

Building, Updating and Verifying Fracture Models in Real Time for Hard Rock
Tunneling

Jeremy Bruyn Decker

Dissertation submitted to the Faculty of the
Virginia Polytechnic Institute and State University
in partial fulfillment of the requirements for the degree of

Doctor of Philosophy
in
Civil Engineering

Mauldon, Matthew, Chair
Gutierrez, Marte S.
Dove, Joseph E.
Westman, Erik C.
Dershowitz, William S.

April 20, 2007
Blacksburg, Virginia

Keywords: trace length, trace density, fractures, stereology, tunnels, Monte Carlo
method, fracture intensity measures, mean fracture size, 3d visualization, database

Building, Updating and Verifying Fracture Models in Real Time for Hard Rock Tunneling

Jeramy Bruyn Decker

Abstract

Fractures and fracture networks govern the mechanical and fluid flow behavior of rock masses. Tunneling and other rock mechanics applications therefore require the characterization of rock fractures based on geological data. Field investigations produce only a limited amount of data from boreholes, outcrops, cut slopes, and geophysical surveys. In tunneling, the process of excavation creates a priceless opportunity to gather more data during construction. Typically, however, these data are not utilized due to the impedance of sampling and analysis on the flow of construction, and safety concerns with sampling within unlined tunnel sections. However, the use of this additional data would increase the overall safety, quality, and cost savings of tunneling.

This study deals with several aspects of the above, with the goal of creating methods and tools to allow engineers and geologists to gather and analysis fracture data in tunnels without interrupting the excavation and without compromising safety. Distribution-independent trace density and mean trace length estimators are developed using principles of stereology. An optimization technique is developed utilizing Differential Evolution to infer fracture size and shape from trace data obtained on two or more nonparallel sampling planes. A method of producing nearly bias free empirical trace length CDF's is also introduced. These new methods and tools were validated using Monte Carlo simulations. A field study was conducted in an existing tunnel allowing the above methods and tools to be further validated and tested. A relational database was developed to aid in storage, retrieval, and analysis of field data. Fracture models were built and updated using fracture data from within the tunnel. Utilization of state of the art imaging techniques allowed for remote sampling and analysis, which were enhanced by the use of 3d visualization techniques.

Acknowledgments

I have so many people to thank for helping this dissertation come to pass. It is the people I have had the chance to work with here at Virginia Tech that I will always remember with fondness. I am grateful to the members of my committee (Dr. Matthew Mauldon, Dr. Marte Gutierrez, Dr. Joe Dove, Dr. Erik Westman, and Dr. William Dershowitz) for all the support, friendship, encouragement, and insight they have provided for me. I would also like to thank Dr. Dershowitz for the use of FracMan. I would especially like to thank my advisor Dr. Mauldon. His insight and support were priceless and I appreciate his genuine concern for my family and me. I am grateful to the Via family and the Via Fellowship for the generous support that made all this possible.

I would like to thank and recognize all my fellow students that I had the opportunity to work with as part of the AMADEUS project and my work here. Sotirios Vardakos for all his insight, friendship, and Greek food. Andrew Ray for his “virtual” support and friendship. Brian Badillo for his part in the development of important software for the field study. Alfred Anthony for his friendship, interesting conversation and support when things were tough. Justin Sommerville for putting up with me in the tunnel and being willing to haul the LiDAR and generator back and forth to the tunnel. Imsoo Lee for putting up with having a desk next to mine and for a good time in Golden. Jon Harris for being a great friend and fishing buddy. There are so many more fellow students that are dear to me that are not named here that I will always remember

I would like to also thank the good people of the Christiansburg Ward of The Church of Jesus Christ of Latter-day Saints for making our family feel right at home.

I would also like to remember all the victims of the tragic events that occurred on Monday April 16, 2007. I know they have all been taken home. I would especially like to remember my good friend Partahi Mamora Halomoan Lumbantoruan (Mora), who I will always remember as a kind selfless person. I look forward to meeting him again beyond this life.

I would like to thank my beautiful wonderful family. My children Bruyn, Hannah, Samuel, and now Elsie have been my inspiration and my greatest fans. My parents, in-laws, and grandmas have given great support and love, despite me moving

their grandkids far away. I would like to remember my Grandpa Nikolaus who passed away during my time here at Virginia Tech. I will always remember those precious days I spent with him driving cattle on the range in Arizona. I look forward to the day I will embrace my Grandfather once more. My lovely wife and best friend Rosanne loved me and believed in me the whole time. She is wonderful beyond belief and I truly love her with all my heart. Lastly, I thank my Heavenly Father, for He is the one true source of knowledge.

Contents

1	Introduction.....	1
2	Generalized Stereological Estimator for Mean Trace Length and Density	3
2.1	Introduction.....	3
2.2	Background.....	5
2.2.1	Density/Intensity Measurements.....	5
2.2.2	Mean Trace Length Estimates	6
2.3	Derivation of Stereological Estimators.....	7
2.3.1	Density Estimator.....	10
2.3.2	Derivation of Mean Trace Length Estimator	15
2.3.3	Relationship among density, mean trace length, and trace intensity (P_{21})	15
2.4	Use of the Stereological Estimators.....	17
2.4.1	Rectangular Windows.....	17
2.4.2	Circular Windows	18
2.4.3	Arbitrary Windows	20
2.5	Field Example	21
2.6	Monte Carlo Simulations and Comparison with Endpoint Estimator	24
2.6.1	Discussion of results	26
	Density Estimators.....	26
	Mean trace length estimators	27
	Further Discussion of Estimators.....	28
2.7	Conclusions.....	28
2.8	Symbols Used	29
2.9	Acknowledgements.....	30
	Appendix 2.A Plots of Monte Carlo Simulations	31
	References.....	41
3	Determining Size and Shape of Fractures from Trace Data using a Differential Evolution Algorithm.....	45
3.1	Introduction.....	45
3.2	Fitness Test	47

3.2.1	Mean Trace Length	47
3.2.2	Trace Length Distribution (K-M-trace)	49
3.2.3	Cost Function	56
3.3	Differential Evolution Algorithm	56
3.3.1	DE Algorithm.....	57
3.3.2	DEfrac	59
3.4	Examples.....	60
3.4.1	Examples 1-3	62
	Example 1	62
	Example 2	64
	Example 3	66
3.4.2	Example 4	68
3.5	Field Example	70
	Discussion on calculating initial slope of empirical CDF from field data.....	73
	Results of DEfrac Analyses Utilizing Field Data	74
3.6	Conclusions.....	75
3.7	Recommended Further Work.....	76
3.8	Symbols Used	80
3.9	Acknowledgements.....	81
	Appendix 3.A: DEfrac User Documentation	82
	Appendix 3.B: K-M-trace User Documentation	87
	References.....	90
4	Rock Fracture Modeling, Imaging and Visualization for a Tunnel in Virginia.....	95
4.1	Introduction.....	95
	Observational Method.....	96
	Fracture Models	96
	Forward Modeling	97
	3d Visualization	98
4.2	Field Site	98
4.2.1	Site Geology and Physiography.....	99
4.3	Tools and Approach.....	101

4.3.1	Database.....	102
4.3.2	Imaging.....	103
4.3.3	Remote Creation of Trace Maps and Data Collection.....	105
4.3.4	Analysis of Data.....	107
4.3.5	Fracture Model and Forward Modeling.....	108
4.4	Field Study Results.....	109
4.4.1	Preliminary Fracture Model.....	109
4.4.2	Forward Modeling – Updating Fracture Model.....	114
	Interval 1, Test Section: Station 1+11 to 1+14.....	114
	Final Model: Station 1+11 to 1+20.....	122
4.5	Conclusions.....	127
4.6	Acknowledgements.....	128
	References.....	128
5	Conclusions and Recommendations.....	135
	Chapter 2.....	135
	Chapter 3.....	136
	Chapter 4.....	137
6	Recommended Further Research.....	141
	Vitae.....	143

List of Figures

- Figure 2.1: Irregular sampling window showing traces oriented at angle θ and with constant length t . The window $a-b-c-d$ itself (vertical light gray stripes on white background with heavy outline) is in the central part of the figure and is surrounded by the *border* (the area with vertical stripes on gray background). The union of the window and its border is referred to as the *window region* ($e-f-g-h-i-j$). A trace intersects the window if and only if its midpoint is inside the window region. The centers of the 16 traces that intersect the window are shown with solid dark circles. The two external rectangles (diagonal gray stripes) and the window $a-b-c-d$ each have the same area, A . The lower rectangle has length l and height μ_h ; the upper rectangle has length l'_{\max} and height μ'_h . These two rectangles are used in subsequent analysis. 8
- Figure 2.2: Plot of expected number, $E(N)$, of fracture traces encountered in a sampling window of area, $A = \mu l$. The traces are of variable length t . The slope of the line is the density ρ and the horizontal axis intercept is defined by the negative of the product of mean trace length μ_t and maximum window length l'_{\max} perpendicular to the traces. (adapted from Mauldon (1998)) 10
- Figure 2.3: Sampling window with four visible traces ($n = 4$), and visible lengths equal to 2, 4, 6, & 8. The apparent mean trace length μ'_t , is $\mu'_t = \frac{L'}{\tilde{N}} = \frac{2+4+6+8}{4} = \frac{20}{4} = 5$.
The scanline shown intersects three traces. 11
- Figure 2.4: Line sampling of fracture traces within a rectangular window of area A . The rectangular area of size $\mu'_h \times l'_{\max}$ corresponds to the upper rectangle in Figure 2.1, which is characterized by light gray diagonal stripes and oriented perpendicular to the traces (Figure 2.1). The horizontal scanline above is shown with exaggerated width dy' and is perpendicular to the traces. 12
- Figure 2.5: The area shown, which represents the integral in Eq. 2.7, consists of infinitesimal trace segments dy' . The mean number of traces intersected \tilde{N}_0 is computed by dividing the area, $(\int_0^{\mu'_h} \tilde{N}_0(y') dy')$ by the width μ'_h 13
- Figure 2.6: Rectangular sampling window with traces oriented at angle θ . Cf. Figure 2.1. 17
- Figure 2.7: Circular sampling window showing traces with a distributed orientation. 19
- Figure 2.8: a) Example of a non-convex sampling window. b) Sampling window with 10 trace segments, showing l'_{\max} in the direction x' . Measured trace lengths l_i (portions inside the window, in m), in order from 1 to 10, are 0.23, 1.31, 0.85, 1.07, 1.91, 0.36, 0.57, 1.21, 0.96, & 0.58. The sum of these lengths is 9.05 m. Even though the window is in this case non-convex, the estimators are applicable because the orientation of traces is such that they cannot intersect the window more than once. Analysis of this case is given in Table 2.1. 20

Figure 2.9: Digital image of rock exposure near the portal of Riverbend Tunnel. A circular sampling area is also shown on the image with a trace map of visible traces with set 3/bedding subhorizontal (blue) and set 1 subvertical (red).....	22
Figure 2.A1a: Performance of Density Estimator. Plot of percent error of density estimate for scenarios 1-5 showing the comparison between the stereological estimator (represented by X's) and the endpoint estimator (represented by O's) for 50 simulations.....	31
Figure 2.A1b: Performance of Density Estimator, continued. Plot of percent error of density estimate for scenarios 4-6 showing the comparison between the stereological estimator (represented by X's) and the endpoint estimator (represented by O's) for 50 simulations.....	32
Figure 2.A1c: Performance of Density Estimator, continued. Plot of percent error of density estimate for scenarios 7-9 showing the comparison between the stereological estimator (represented by X's) and the endpoint estimator (represented by O's) for 50 simulations.....	33
Figure 2.A1d: Performance of Density Estimator, continued. Plot of percent error of density estimate for scenarios 10-12 showing the comparison between the stereological estimator (represented by X's) and the endpoint estimator (represented by O's) for 50 simulations.....	34
Figure 2.A1e: Performance of Density Estimator, continued. Plot of percent error of density estimate for scenarios 13-15 showing the comparison between the stereological estimator (represented by X's) and the endpoint estimator (represented by O's) for 50 simulations.....	35
Figure 2.A2a: Performance of Mean Trace Length Estimator. Plot of percent error of mean trace length estimate for scenarios 1-3 showing the comparison between the stereological estimator (represented by X's) and the endpoint estimator (represented by O's) for 50 simulations.....	36
Figure 2.A2b: Performance of Mean Trace Length Estimator, continued. Plot of percent error of mean trace length estimate for scenarios 4-6 showing the comparison between the stereological estimator (represented by X's) and the endpoint estimator (represented by O's) for 50 simulations.....	37
Figure 2.A2c: Performance of Mean Trace Length Estimator, continued. Plot of percent error of mean trace length estimate for scenarios 7-9 showing the comparison between the stereological estimator (represented by X's) and the endpoint estimator (represented by O's) for 50 simulations.....	38
Figure 2.A2d: Performance of Mean Trace Length Estimator, continued. Plot of percent error of mean trace length estimate for scenarios 10-12 showing the comparison between the stereological estimator (represented by X's) and the endpoint estimator (represented by O's) for 50 simulations.....	39
Figure 2.A2e: Performance of Mean Trace Length Estimator, continued. Plot of percent error of mean trace length estimate for scenarios 13-15 showing the comparison	

between the stereological estimator (represented by X's) and the endpoint estimator (represented by O's) for 50 simulations.....	40
Figure 3.1: Rectangular fracture intersecting a sampling window and creating an intersection vector (trace). a) Shows the intersection vector or fracture trace as seen in the field with portion of fracture shown in rock mass. b) Entire fracture shown, long side a and short side b , and the angle between the intersection vector and side b is denoted β	48
Figure 3.2: Rectangular fracture with side lengths a & b , with $a \geq b$, angle β between intersection vector and side b	49
Figure 3.3: Sampling window with 4 visible traces (2 uncensored – solid lines, 2 censored – dotted lines). Lengths of traces given in Figure 3.4.....	51
Figure 3.4: Example of application of product limit method to trace length data (partial data set).	51
Figure 3.5: Empirical partial CDF for example given in Figure 3.3 and Table 3.1. The linear plot is consistent with constant size rectangular fractures.....	52
Figure 3.6: PDF of intersection lengths for rectangular fractures intersecting a tunnel face as shown in Figure 3.2.	53
Figure 3.7: CDF of intersection lengths for rectangular fractures intersecting a tunnel face as shown in Figure 3.2. The CDF is linearized in straight line segments from p_0 to p_1 , etc. Section p_0 - p_1 defines the initial slope (ψ).....	53
Figure 3.8: Examples of empirical CDF's (uncensored and using K - M -trace) shown with the complete theoretical CDF. The section from p_0 – p'_1 is the initial straight-line portion of the empirical CDF that will be used to measure, $\tilde{\psi}$. The empirical CDF's were created from simulated data in FracWorks. Example a) ($a = 20$, $b = 10$, & $\beta = 45^\circ$) was sampled on a 20 X 20 m sampling window with 58 total traces visible (21—uncensored, 37—censored). Example b) ($a = 20$, $b = 10$, & $\beta = 45^\circ$) was sampled on a 10 X 10 m sampling window with 48 total traces visible (7—uncensored, 41—censored).....	55
Figure 3.9: Schematic of one generation within a Differential Evolution algorithm for individual X_1	59
Figure 3.10: User interface for $DEfrac$ in Excel.....	60
Figure 3.11: a) Population of fractures for example 1 generated within FracWorks. Fractures generated inside and cut by a $100 \times 100 \times 100 \text{m}^3$ generation region. b) Location and orientation of rectangular sampling windows used to sample fracture population in FracWorks. Traces are shown on sampling windows.	61
Figure 3.12: Evolving estimate of fracture size and shape for Example 1. Darker square represents the actual fracture and lighter evolving rectangle represents estimates based on $DEfrac$. Stages are as follows: a) 1 generation, b) 10 generations, c) 20 generations, and d) 60 generations.....	64

Figure 3.13: Evolving estimate of fracture size and shape for Example 2. Darker rectangle represents the actual fracture and lighter evolving rectangle represents estimates based on <i>DEfrac</i> . Stages are as follows: a) 1 generation, b) 10 generations, c) 20 generations, and d) 60 generations.	66
Figure 3.14: Evolving estimate of fracture size and shape for Example 3. Darker rectangle represents the actual fracture and lighter evolving rectangle represents estimates based on <i>DEfrac</i> . Stages are as follows: a) 1 generation, b) 10 generations, c) 20 generations, and d) 60 generations.	68
Figure 3.15: Estimate of fracture size and shape for Example 4. Darker rectangle represents the actual mean fracture and lighter rectangle represents estimates based on <i>DEfrac</i>	70
Figure 3.16: Photograph within Riverbend Tunnel.	71
Figure 3.17: Trace maps of (a) right (west) wall in tunnel with set 1 (red) sub-vertical and set 3/bedding (blue) sub-horizontal, (b) roof in tunnel with only set 1 (red) and (c) rock face near north portal of tunnel with set 1 (red) sub-vertical and set 3/bedding (blue) sub-horizontal. Note termination of set 1 fractures on bedding planes.	72
Figure 3.18: Equal area lower hemisphere projection of poles for set 1.	72
Figure 3.19: Empirical trace length CDF's for (a) right (west) wall, (b) roof, and (c) portal calculated using K-M-trace. A lower bound and upper bound $p'1$ are estimated given a range of initial slopes.	73
Figure 3.20: Estimates of fracture size and shape for Example 5, 6, & 7. Darker rectangle or ellipse represents the actual mean fracture and lighter rectangle represents estimates based on <i>DEfrac</i> , a) Example 5, b) Example 6, and c) Example 7.	79
Figure 3.A1: Assumed fracture geometry for <i>DEfrac</i> analysis.	85
Figure 3.B1: Partial empirical trace length CDF.	89
Figure 4.1: North portal of Riverbend Tunnel. Note bedding dipping to the left (southeast) and sub-vertical fractures. There is a major solutionally enlarged fracture just inside this portal, as can be seen from the soil infilling that has spilled onto the tunnel floor.	98
Figure 4.2: (a) Topographic map of site showing tunnel, sink holes and river; (b) view of tunnel showing solutionally enlarged fractures (numbered 1-25) and test section.	99
Figure 4.3: (a) Small sinkhole located at point A on Fig. 4.2, 80m west of the tunnel test section; (b) Near-vertical joints forming columnar structures along New River east of the tunnel, at point B on Fig. 4.2.	100
Figure 4.4: Solutionally enlarged fracture No. 10, at Station 1+34.5 on right (west) wall of tunnel. Note vertical meter stick bottom center. Bedding dips to the left. Several fractures dip steeply to left-front on left side of picture. Solutionally	

enlarged fracture is earth filled with boulders or pinnacles. View is horizontal towards the southwest.....	101
Figure 4.5: Schematic of AMADEUS database showing 5 raw data databases feeding processed data into the centralized project database which is being used for design, reporting and model building processes.	102
Figure 4.6: Nikon 100D digital cameras mounted for stereo imaging.	103
Figure 4.7: Stereo pair of right (west) wall at station 1+12.5.....	104
Figure 4.8: ILRIS-3D LiDAR scanner by Optech mounted on custom cart for transportation of scanner along tunnel. Tilt table allows scanning at various angles.	104
Figure 4.9: LiDAR scan along tunnel alignment with scanner at station 1+05.5. View is towards the south; the image shows intensity values only. The scan was taken without any artificial (visible) light.	105
Figure 4.10: Two projectors for AMADEUS GeoWall shown with polarizing lenses. .	106
Figure 4.11: Fully immersive viewing of LIDAR 3d data within CAVE at Virginia Tech. The researcher is wearing polarized glasses and is holding a wand that controls navigation within the VE.	107
Figure 4.12: Excavated 3d fracture model with circular sampling area on right wall (dark circle).	109
Figure 4.13: Lower hemisphere equal area stereonet plot of poles of orientation measurements taken near north portal. The stereonet was made using XStereo, a spreadsheet program developed primarily for teaching at Virginia Tech.....	111
Figure 4.14: Trace map created from digital image of rock wall near north portal with traces from Set 1 (red, sub-vertical) and Set 3/bedding (blue, sub-horizontal). .	111
Figure 4.15: Preliminary fracture model with virtual excavation from station 1+11 to 1+21.	114
Figure 4.16: Lower hemisphere equal area stereonet plot of poles with added measurements from LiDAR images (LiDAR measurements circled).....	115
Figure 4.17: Trace maps created from digital images of right (west) wall ((a) digital image with trace fractures, (b) equivalent straight lines for measurement, set 1 (red) sub-vertical and set 3/bedding (blue) sub-horizontal) and roof ((c) digital image with trace fractures, (d) equivalent straight lines for measurement, set 1 (red) sub-vertical and set 2 (green) sub-horizontal) in tunnel.....	116
Figure 4.18: Digital image of the roof showing abrupt steps to bedding planes.	117
Figure 4.19: Updated fracture model after the analysis of interval 1 with a virtual excavation from station 1+11 to 1+21.	120
Figure 4.20: Lower hemisphere equal area stereonet plot of poles with added measurements from additional manual measurements in tunnel (enclosed by red squares) and LiDAR images (enclosed by blue circles).	122

- Figure 4.21: Final fracture model: a) not excavated, b) excavated with the location of the existing solutionally enlarged fracture No. 8..... 125
- Figure 4.22: Comparison between actual trace maps and simulated trace maps. Trace maps from between station 1+17 and 1+20 on the right (west) wall (a) and the roof (c). Simulated trace maps created on planes parallel to the right (west) wall (b) and the roof (d)..... 126

List of Tables

Table 2.1: Application of stereological estimators to the example shown in figure 2.8...	21
Table 2.2: Parameters obtained from trace map for set 1 & 3 for use with the stereological estimator and the endpoint estimator. The results of the applied estimators are also shown.....	23
Table 2.3: Details of Monte Carlo simulation scenarios.....	25
Table 2.4: Summary of performance of stereological and endpoint trace density estimators based on the magnitude of intensity (a), mean trace length (b), and trace length variance (c).	26
Table 2.5: Summary of performance of stereological and endpoint mean trace length estimators based on the magnitude of intensity (a), mean trace length (b), and trace length variance (c).....	27
Table 3.1: Calculated values for example shown in Figure 3.3.....	52
Table 3.2: Varied fracture set parameters for Examples 1-4.	61
Table 3.3: Data obtained from sampling windows used as input into the <i>DEfrac</i> software for Example 1.....	63
Table 3.4: Results of Example 1 (6 tests).	63
Table 3.5: Data obtained from sampling windows used as input into the <i>DEfrac</i> software for Example 2.....	65
Table 3.6: Results of Example 2 (6 tests).	65
Table 3.7: Data obtained from sampling windows used as input into the <i>DEfrac</i> software for Example 3.....	67
Table 3.8: Results of Example 3 (6 tests).	67
Table 3.9: Data obtained from sampling windows used as input into the <i>DEfrac</i> software for Example 4.....	69
Table 3.10: Results of Example 4.....	69
Table 3.11: Trace data obtained from analyses of trace maps created from digital images in Riverbend Tunnel and mean orientation used as input into the <i>DEfrac</i> software for the field example.	74
Table 3.12: Results of field example in tunnel within Riverbend Tunnel.	75
Table 3.13: Varied fracture set parameters for Examples 5, 6, & 7.	77
Table 3.14: Data obtained from sampling windows used as input into the <i>DEfrac</i> software for Example 5.....	78
Table 3.15: Data obtained from sampling windows used as input into the <i>DEfrac</i> software for Example 6.....	78

Table 3.16: Data obtained from sampling windows used as input into the <i>DEfrac</i> software for Example 7.....	78
Table 3.17: Results of Examples 5, 6, & 7.	79
Table 4.1: Trace data obtained from circular sampling window for set 1.	112
Table 4.2: Fracture parameters for preliminary fracture model.....	113
Table 4.3: Trace data obtained from circular sampling windows on right (west) wall and roof of interval 1 for set 1 and set 2.....	117
Table 4.4: Fracture parameters obtained for Set 1 from <i>DEfrac</i> analysis after interval 1.	118
Table 4.5: Fracture parameters input into FracWorks after considering <i>DEfrac</i> analysis and forward modeling analysis for Interval 1.	119
Table 4.6: Results of virtual sampling of updated model and preliminary model after analysis of interval 1. Comparison also shown with measured field data.	121
Table 4.7: Final fracture parameters input into FracWorkXP for station 1+11 to 1+21	124

This page intentionally left blank.

1 Introduction

Fracture networks govern the mechanical and fluid flow behavior of rock masses. Obtaining fracture data is essential, therefore, in the design and excavation of hard rock tunnels. The best source of data is often the tunnel surfaces, which are continually being exposed during the excavation process. The difficulty with utilizing this data is being able to gather data in the tunnel, analysis the data, and possibly implement the findings without slowing construction or endangering personnel at the open face of the tunnel. The AMADEUS research project at Virginia Tech, which began at Virginia Tech in 2003 with funding from the National Science Foundation, is developing and testing new tools and techniques to allow rock fracture data to be quickly obtained and analyzed during tunnel construction. This dissertation focuses on several of these tools and techniques that are related to updating, building, and verifying rock fracture models. Three of the chapters in the dissertation will be submitted to journals for publication.

The dissertation is organized as follows. Chapter 1 gives an introduction. Chapter 2 introduces a generalized distribution-independent stereological estimator for trace density and mean trace length. The stereological estimators is tested and compared with previously published endpoint estimators. Chapter 3 presents an optimization method using Differential Evolution for inferring fracture size and shape from trace data on two or more nonparallel planar surfaces, and also describes a methodology for obtaining a nearly unbiased empirical trace length CDF using the principles of the Kaplan-Meier procedure for life tests. Chapter 4 presents the results of a field study that was conducted in an existing tunnel. Tools and techniques introduced in earlier chapters are utilized in the field study along with a relational database, state of the art imaging tools, and 3d visualization techniques. Data obtained from the tunnel are utilized to build a fracture model, and then to update and verify the model using principles of forward modeling. General conclusions are given in Chapter 5; refer to the Conclusions sections contained in the individual chapters for more specific and detailed conclusions. A few suggestions on further research needs concerning the research topics in this dissertation are given in Chapter 6.

This page intentionally left blank.

2 Generalized Stereological Estimator for Mean Trace Length and Density

Abstract: Rock engineering projects generally require quantification of rock fracture parameters. In this paper, the focus is on fracture traces exposed at a planar rock face and examined within a sampling window. Estimators for fracture trace density and mean fracture trace length are derived based on stereological principles and are generalized for any arbitrary convex sampling window shape. The estimators are shown to form a unified set and to be consistent with the rock fracture abundance measure P_{21} , defined by the total length of trace segments in a sampling window divided by the area of the window. The new estimators are demonstrated for special cases such as rectangular and circular windows. The estimators are also shown to be applicable, under certain conditions, to non-convex windows. Use of the estimators is demonstrated by applying them to field data from a tunnel. Monte Carlo simulations are carried out to check the performance and accuracy of the new estimators, and to compare them with previously published endpoint estimators. Generally speaking, we find that the stereological estimators perform better than the endpoint estimators for relatively short traces, especially for mean trace length, while the endpoint estimators perform better for long traces.

2.1 Introduction

The characterization of fracture networks in rock masses is an essential step in the analysis of stability and deformation, fluid storage, and fluid flow. Nature rarely presents engineers and geologists with the chance to view and measure entire fractures. The data utilized to characterize fracture networks are typically obtained from small areas of partially exposed fractures and from traces created by fractures that intersect outcrops, boreholes, tunnel walls, and other surfaces. Exposed portions of fractures are used to measure fracture orientation, while exposed traces are used to estimate trace parameters such as trace intensity, density, and length. These parameters are then used to infer 3d fracture network characteristics. Obtaining accurate fracture parameters for the 3d rock mass depends on obtaining accurate trace parameters. Trace length measurements taken

from rock exposures, however, are inherently flawed due to censoring and length biases (Mauldon, 2000; Priest, 1993), as well as other sampling difficulties (Einstein and Baecher, 1983). This paper presents a method of obtaining distribution free estimates of areal density (trace density) and mean trace length from window sampling, utilizing principles of stereology.

Window sampling refers to the measurement of those portions of fracture traces that are visible within a defined area, known as a window. The window may be of any shape or size, but is assumed to be planar. Typically many traces are censored in window sampling. The term censored indicates that only a portion of the trace occurs within the window; some portion of the trace is hidden, i.e., outside the window. Also, due to a length bias, larger traces are more likely to be sampled in a given window than smaller traces. These two sampling biases, censoring and length bias, affect the outcome of trace density and mean trace length measurements. A natural way to measure trace density would be to divide the number of trace centers in the window by the area of the window. When analyzing censored traces, however, it is impossible to determine if the trace midpoint is contained in the window or not. If censored trace midpoints are assumed inside the sampling window, then the density will likely be overestimated. On the other hand, if they are assumed to be outside the sampling window the density will be underestimated. Both censoring and length bias create problems in estimating mean trace length since they skew the measured population. Field measurements of trace density and mean trace length are typically overestimated and underestimated, respectively, due to these sampling biases (Baecher and Lanney, 1978; Baecher et al., 1977; Mauldon, 2000).

Stereological principles can be used to estimate trace length parameters that are free of sampling biases and that do not require the assumption of an underlying distribution (Mauldon, 1998). In this paper, the stereological mean trace length estimator for vertical traces in a rectangular window (Mauldon, 1998) is generalized for any convex sampling window with any orientation, or orientation distribution, of traces. The method is also expanded to include a trace density estimator based on stereological principles. The mean trace length estimator and density estimator, together with the

stereological areal or trace intensity P_{21} (Dershowitz et al., 2000; Underwood, 1970), are shown to form a mutually consistent set of estimators.

A brief background on the analysis of trace intensity (trace length per unit area), density (trace centers per unit area), and mean length will be given. Then the derivation of the stereological estimator for trace density and mean length will be presented, along with the relationship between the estimators and trace intensity. The performance of the estimated parameters will then be demonstrated by sampling simulated data along with actual field data from an inactive train tunnel in Southwest, Virginia. The stereological estimators will also be compared with the endpoint estimator for trace density and mean trace length (Kulatilake and Wu, 1984b; Mauldon, 1998; Mauldon et al., 2001; Mauldon et al., 1999a; Mauldon et al., 1999b; Pahl, 1981; Rohrbaugh Jr. et al., 2002; Zhang and Einstein, 1998).

2.2 Background

A brief background of density/intensity measurements and mean trace length estimates will be given in this section.

2.2.1 Density/Intensity Measurements

Fracture systems in rock masses can be described quantitatively by means of fracture abundance measures (Dershowitz et al., 2000; Dershowitz, 1985; Dershowitz and Herda, 1992; Mauldon and Dershowitz, 2000). Examples of fracture abundance measures are linear intensity P_{10} — number of fractures per linear unit along a direction, areal/trace density P_{20} — number of fracture traces per unit area, areal/trace intensity P_{21} — summed fracture length per unit area, 3d density P_{30} — number of fractures per unit volume, and 3d intensity P_{32} — summed fracture area per unit volume (Dershowitz and Herda, 1992; Mauldon, 1994; Mauldon and Dershowitz, 2000). Trace intensity can be shown to be equivalent to the product of trace density and mean trace length (Mauldon et al., 2001). The most useful is usually P_{32} , which is also the most difficult to obtain.

Areal intensity P_{21} can be estimated by dividing the total length of fracture traces in the window by the window area (Underwood, 1970). An estimator for trace intensity P_{21} has also been developed based on intersections with a sampling circle (Mauldon et

al., 2001; Mauldon et al., 1999a). Areal density P_{20} cannot be measured directly if traces are censored. This difficulty can be circumvented, however, by means of a distribution-independent trace endpoint method (Mauldon, 1998; Mauldon et al., 2001; Mauldon et al., 1999a; Rohrbaugh Jr. et al., 2002). Distribution dependent methods for estimating density have been published by several researchers (Kulatilake and Wu, 1984a; Warburton, 1980a; Warburton, 1980b).

2.2.2 Mean Trace Length Estimates

There are three types of sampling biases that are encountered when measuring trace lengths: first, truncation bias — small fractures are not measured; second, length bias — longer trace lengths are more likely to be sampled; and third, censoring bias — some portion of the trace is not seen (e.g., Baecher, 1980; Baecher and Lanney, 1978; Call et al., 1976; Cruden, 1977; Einstein and Baecher, 1983; Kulatilake and Wu, 1984b; Laslett, 1982a; Pahl, 1981; Priest, 1993; Warburton, 1980a). The first bias can typically be ignored if the truncation limit is set small enough in sampling procedures (e.g., Einstein and Baecher, 1983). Length bias and censoring bias can have a large affect on results and, therefore, need to be addressed. Several distribution-dependent approaches to dealing with these two biases have been proposed (e.g., Baecher, 1980; Baecher and Lanney, 1978; Baecher et al., 1977; Cruden, 1977; Grossmann, 1995; Priest and Hudson, 1981; Song and Lee, 2001; Warburton, 1980a; Warburton, 1980b). Some researchers have approached censored traces as analogous to truncated life tests (e.g., Epstein, 1954) and applied the methodology developed by Kaplan and Meier (1958) for medical statistics (e.g., Decker and Mauldon, 2006; Decker and Mauldon, 2007a; Laslett, 1982a; Laslett, 1982b). An innovative distribution-independent mean trace length estimator based on trace endpoints was introduced by Pahl (1981), extended (Kulatilake and Wu, 1984b), and generalized to convex windows of arbitrary shape, with variable fracture trace orientation (Mauldon, 1998; Mauldon et al., 2001; Mauldon et al., 1999b; Rohrbaugh Jr. et al., 2002; Zhang and Einstein, 1998).

2.3 *Derivation of Stereological Estimators*

The irregular sampling window in Figure 2.1 shows parallel traces of length t . The area defined by the union of the window and its *border* (Fig. 2.1) is termed the *window region*. The midpoints of traces must be within the window region in order for the traces to intersect the window. Traces with midpoints in the border, as well as those with midpoints in the window, have non-empty intersections with the window itself. The border is dependent on the orientation of the traces relative to the sampling window, and also on the half-length of the traces.

We make use of the window region in the derivation of the stereological estimators for trace density and mean trace length. These estimators will apply to convex sampling windows, as well as to non-convex windows as long as traces are oriented such that no trace can intersect the window more than once.

We make the following assumptions:

- Stationarity – statistics are not affected by the location of the sampling window.
- Planar fractures and sampling windows – fractures are flat surfaces and thus create straight line traces on planar sampling windows.
- Sampling window and fractures are independent of each other.

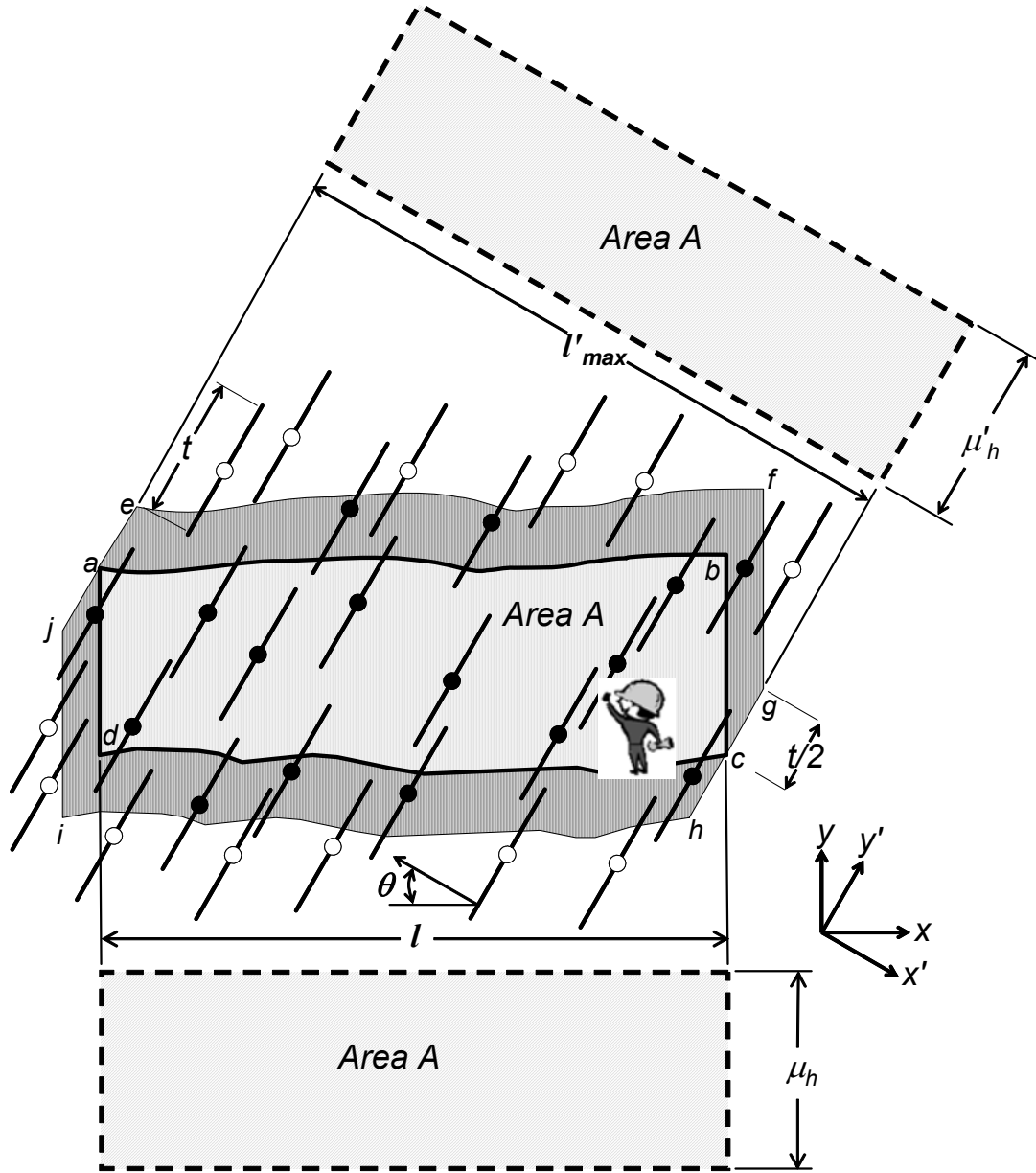


Figure 2.1: Irregular sampling window showing traces oriented at angle θ and with constant length t . The window $a-b-c-d$ itself (vertical light gray stripes on white background with heavy outline) is in the central part of the figure and is surrounded by the *border* (the area with vertical stripes on gray background). The union of the window and its border is referred to as the *window region* ($e-f-g-h-i-j$). A trace intersects the window if and only if its midpoint is inside the window region. The centers of the 16 traces that intersect the window are shown with solid dark circles. The two external rectangles (diagonal gray stripes) and the window $a-b-c-d$ each have the same area, A . The lower rectangle has length l and height μ_h ; the upper rectangle has length l'_{max} and height μ'_h . These two rectangles are used in subsequent analysis.

For constant length traces, as seen in Figure 2.1, the expected number $E(N)$ of traces intersecting the window is given as

$$E(N) = \rho(A + tl'_{\max}) = \rho(\mu_h l + tl'_{\max}) = \rho\mu_h l + \rho tl'_{\max}, \quad (2.1)$$

where:

t is the length of the fracture traces, (for now assumed constant),

ρ is the density (number per unit area), and

A is the area of the sampling window,

l is the length of the window in direction x (e.g., along the tunnel),

μ_h is the mean height of the window measured in direction y (Figure 2.1), such

that , $\mu_h l = A$

l'_{\max} is the maximum length of the sampling window in direction x' (perpendicular to the traces),

μ'_h is the mean height of the window in direction y' (parallel to traces) such that

$\mu'_h l'_{\max} = A$

For traces of variable length t the expected number $E(N)$ of traces that intersect a window of mean height μ_h is

$$E(N) = \rho\mu_h l + \rho l'_{\max} \int_{t=0}^{t=\infty} t dF(t) = \rho\mu_h l + \rho l'_{\max} \int_0^1 t dF = \rho\mu_h l + \rho\mu_t l'_{\max}. \quad (2.2)$$

where:

$F(t)$ is the cumulative distribution of the trace lengths, and

μ_t is the mean trace length.

Riemann-Stieltjes integration is used in Eq. 2.2 to cover both continuous and discrete distributions, or a combination thereof (Mauldon, 1998).

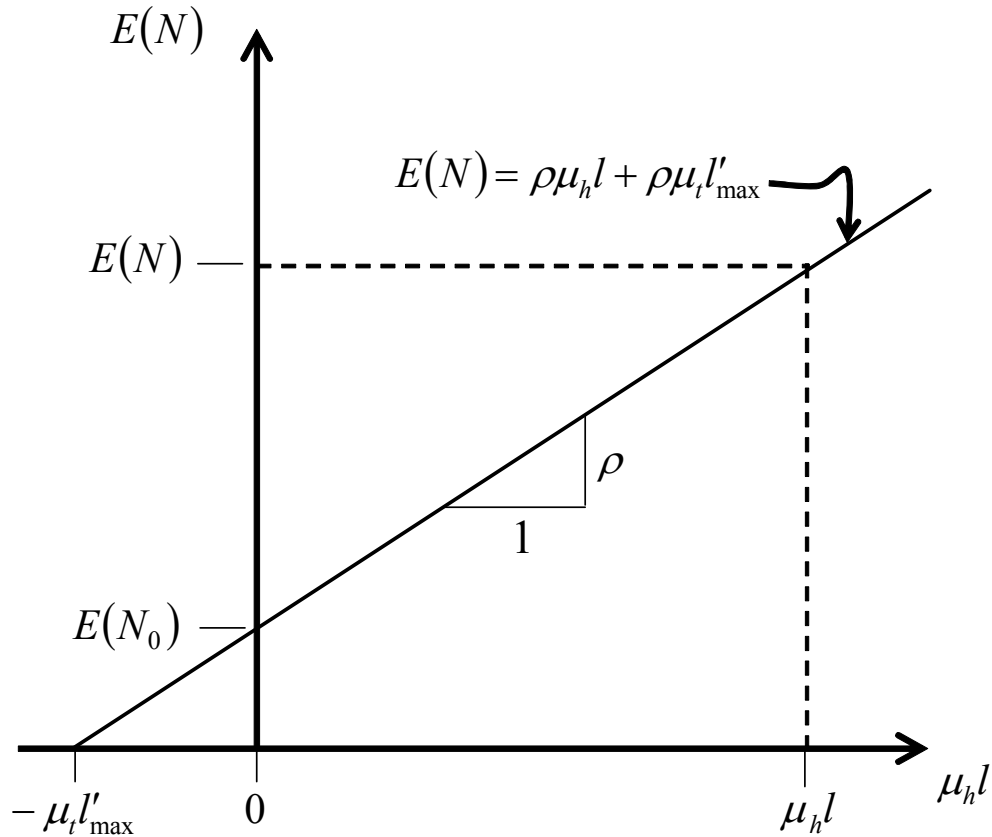


Figure 2.2: Plot of expected number, $E(N)$, of fracture traces encountered in a sampling window of area, $A = \mu_t l$. The traces are of variable length t . The slope of the line is the density ρ and the horizontal axis intercept is defined by the negative of the product of mean trace length μ_t and maximum window length l'_{\max} perpendicular to the traces. (adapted from Mauldon (1998))

2.3.1 Density Estimator

We let $E(N_0)$ denote the expected number of traces encountered within a window with length l'_{\max} and height zero perpendicular to the traces; i.e., a scanline (See Figure 2.2).

From similar triangles (Figure 2.2), the following expression can be given for density, ρ :

$$\rho = \frac{E(N) - E(N_0)}{\mu_h l}. \tag{2.3}$$

Using the field-obtained counts \tilde{N} and \tilde{N}_0 in place of the expectations $E(N)$ and $E(N_0)$ in Eq. 2.3 gives an estimate $\tilde{\rho}$ of trace density

$$\tilde{\rho} = \frac{\tilde{N} - \tilde{N}_0}{\mu_h l}. \tag{2.4}$$

Let L' denote the combined lengths of those portions of traces that occur inside the window (i.e. the summed lengths of solid line trace segments in Figure 2.3); let \tilde{N} denote the number of traces intersecting the window; let μ'_t denote the apparent average trace length in the original window. Then L' , can be expressed as

$$L' = \mu'_t \tilde{N}. \tag{2.5}$$

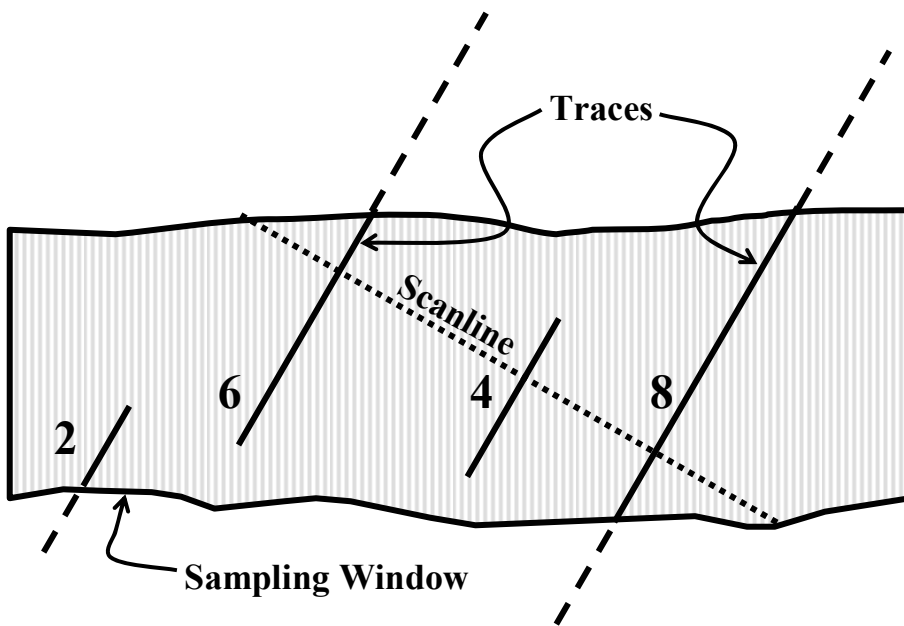


Figure 2.3: Sampling window with four visible traces ($n = 4$), and visible lengths equal to 2, 4, 6, & 8. The apparent mean trace length μ'_t , is $\mu'_t = \frac{L'}{\tilde{N}} = \frac{2+4+6+8}{4} = \frac{20}{4} = 5$. The scanline shown intersects three traces.

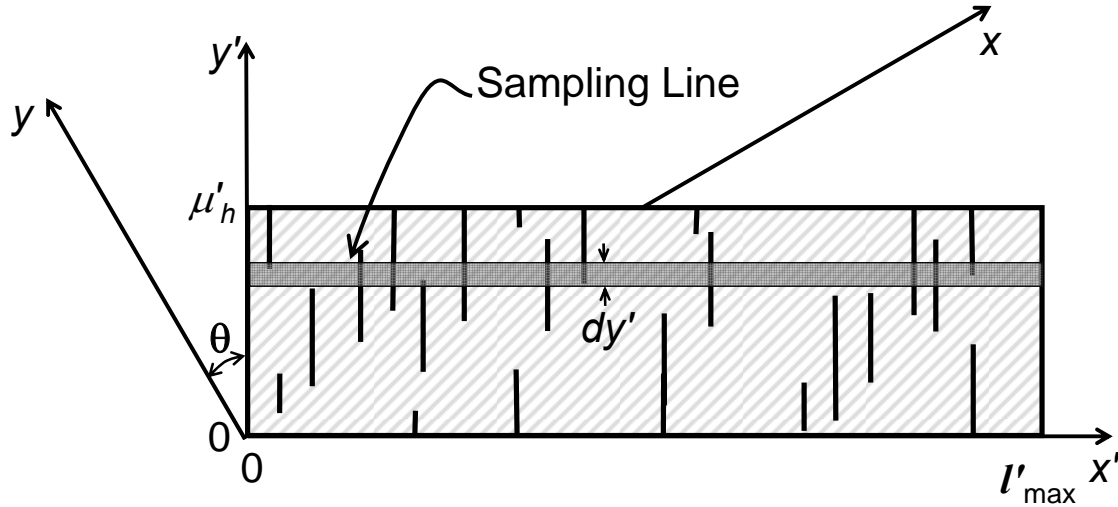


Figure 2.4: Line sampling of fracture traces within a rectangular window of area A . The rectangular area of size $\mu'_h \times l'_{\max}$ corresponds to the upper rectangle in Figure 2.1, which is characterized by light gray diagonal stripes and oriented perpendicular to the traces (Figure 2.1). The horizontal scanline above is shown with exaggerated width dy' and is perpendicular to the traces.

Let $\tilde{N}_0(y')$ be the number of traces intersected by a line sample at position y' . For simplicity, and without loss of generality, we assume $0 \leq \theta < 90$. The differential length of traces from sampling line y' to $y' + dy'$ is given by

$$dL = \tilde{N}_0(y') dy' . \tag{2.6}$$

Therefore, the total length, L' , of traces in the window can be found as

$$L' = \int dL = \int_0^{\mu'_h} \tilde{N}_0(y') dy' , \tag{2.7}$$

Since all three regions in Figure 2.1 have identical area A , the total length L' of traces in the window is the same, on average, for all three regions. Therefore, Eq. 2.7 represents the total length L' of traces in the window in Figure 2.1. The integral on the right hand side of Eq. 2.7 can be represented as the area shown in Figure 2.5. The vertical

column at position y' in Figure 2.5 has length corresponding to the number $\tilde{N}_0(y')$ of traces intersected at $y = y'$ and width dy' . Total trace length at y' is represented on Figure 2.5 as length dy' multiplied by $\tilde{N}_0(y')$. The summed area of differential columns is then total trace length L' . Therefore, the mean number of traces \tilde{N}_0 intersected by a sampling window of height zero perpendicular to the traces, is the integral in Eq. 2.7 divided by expected height μ'_h in the direction of the traces (Mauldon, 1998; Underwood, 1970).

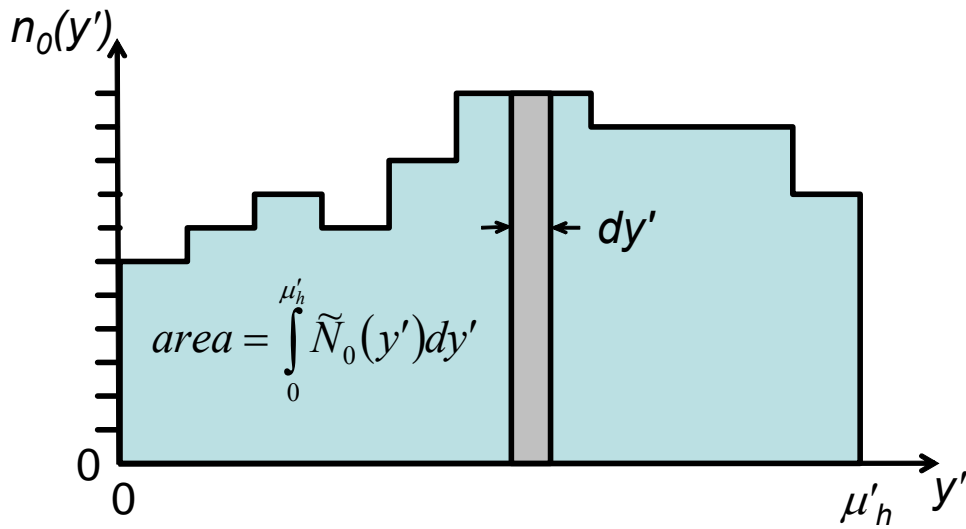


Figure 2.5: The area shown, which represents the integral in Eq. 2.7, consists of infinitesimal trace segments dy' . The mean number of traces intersected \tilde{N}_0 is computed by dividing the area,

$(\int_0^{\mu'_h} \tilde{N}_0(y') dy')$ by the width μ'_h .

$$\tilde{N}_0 = \frac{1}{\mu'_h} \int_0^{\mu'_h} \tilde{N}_0(y') dy' . \tag{2.8}$$

Substituting the results of Eq. 2.7 into the above yields,

$$\tilde{N}_0 = \frac{L'}{\mu'_h} . \tag{2.9}$$

Now substituting Eq 2.5 into Eq. 2.9, results in

$$\tilde{N}_0 = \frac{\mu'_t \tilde{N}}{\mu'_h}. \quad (2.10)$$

The area of any convex window can be expressed as the maximum length of the window in direction x' multiplied by the mean height in direction y' (Figure 2.1). Therefore,

$$l'_{\max} \mu'_h = \mu_h l = A \quad (2.11)$$

and

$$\frac{\mu_h l}{l'_{\max}} = \frac{A}{l'_{\max}} = \mu'_h. \quad (2.12)$$

Now substitute Eq. 2.10 and Eq. 2.11 into Eq. 2.4 and simplify to obtain the estimate of trace density,

$$\tilde{\rho} = \frac{1}{A} \left(\tilde{N} - \frac{\mu'_t \tilde{N}}{\mu'_h} \right) = \frac{\tilde{N}}{A} \left(1 - \frac{\mu'_t}{\mu'_h} \right), \quad (2.13)$$

where μ'_t and μ'_h , defined earlier, are the apparent mean length of the visible traces (Figure 2.3), and the mean height of the window in direction y' (Figure 2.1), respectively.

Defining an apparent density, $\rho' = \tilde{N}/A$ allows the density estimator (Eq. 2.13) to be expressed as

$$\tilde{\rho} = \mu'_t \rho' \left(\frac{1}{\mu'_t} - \frac{1}{\mu'_h} \right). \quad (2.14)$$

2.3.2 Derivation of Mean Trace Length Estimator

Using similar triangles (Figure 2.2), the following relationship can be defined:

$$E(N_0)/\mu_t l'_{\max} = E(N)/(\mu_t l'_{\max} + \mu_h l). \quad (2.15)$$

Then, solving for the reciprocal of the mean trace length μ_t ,

$$\frac{1}{\mu_t} = \frac{l'_{\max}}{\mu_h l} \frac{E(N) - E(N_0)}{E(N_0)}. \quad (2.16)$$

Using the field-obtained counts \tilde{N} and \tilde{N}_0 in place of the expectations $E(N_0)$ and $E(N)$ in Eq. 2.16, and substituting Eq. 2.10 into Eq. 2.16, gives

$$\frac{1}{\tilde{\mu}_t} = \frac{l'_{\max}}{\mu_h l} \frac{\tilde{N} - \mu'_t \tilde{N} / \mu'_h}{\mu'_t \tilde{N} / \mu'_h} = \frac{l'_{\max} \mu'_h}{\mu_h l} \left(\frac{1}{\mu'_t} \right) - \frac{l'_{\max}}{\mu_h l}. \quad (2.17)$$

Substitute Eqs. 2.11 & 2.12 into Eq. 2.17 and simplify to obtain the mean trace length estimator,

$$\tilde{\mu}_t = \left(\frac{1}{\mu'_t} - \frac{1}{\mu'_h} \right)^{-1} \quad (2.18)$$

2.3.3 Relationship among density, mean trace length, and trace intensity (P_{21})

The areal intensity P_{21} is a basic parameter of stereology (Underwood, 1972), where it is usually denoted L_A . The notation P_{21} (Dershowitz et al., 2000) is intended to serve as a reminder of the dimension of the sampling domain (in this case, 2) and the dimension of the feature being measured (in this case, 1). P_{21} can be expressed as

$$P_{21} = \frac{L'}{A}. \quad (2.19)$$

Now plug in the results of Eq. 2.5 to obtain

$$P_{21} = \frac{\mu'_t \tilde{N}}{A} = \left(\frac{\tilde{N}}{A} \right) \mu'_t = \rho' \mu'_t. \quad (2.20)$$

We now show the relationship between P_{21} and the derived density and mean trace length estimator by writing

$$P_{21} = \rho' \mu'_t \left(\frac{\frac{1}{\mu'_t} - \frac{1}{\mu'_h}}{\frac{1}{\mu'_t} - \frac{1}{\mu'_h}} \right) = \left[\rho' \mu'_t \left(\frac{1}{\mu'_t} - \frac{1}{\mu'_h} \right) \right] \left[\left(\frac{1}{\mu'_t} - \frac{1}{\mu'_h} \right)^{-1} \right]. \quad (2.21)$$

Replacing the expressions in square brackets on the right hand side with the estimators for density $\tilde{\rho}$ and mean trace length $\tilde{\mu}_t$ respectively (Eqs. 2.14 & 2.18) gives

$$\tilde{P}_{21} = \tilde{\rho} \times \tilde{\mu}_t. \quad (2.22)$$

The above expression Eq. 2.22 confirms that trace intensity is equal, on average, to the product of the trace density and mean trace length and shows that the derived stereological estimators for trace density $\tilde{\rho}$ mean trace length $\tilde{\mu}_t$ and trace intensity P_{21} are a mutually consistent, unified set of estimators. Eq. 2.22 also results in the following relationship (see Eq. 2.20 & 2.22),

$$\frac{\tilde{\rho}}{\rho'} = \frac{\mu'_t}{\tilde{\mu}_t} \quad (2.23)$$

2.4 Use of the Stereological Estimators

A few examples of the application of the stereological estimators will now be given to demonstrate their use in field geological studies.

2.4.1 Rectangular Windows

The mean trace length estimator for rectangular windows with vertical (or horizontal traces), using stereological principles, has been discussed previously (Mauldon, 1998). This section will look at both the trace density and mean length estimators when the traces are oriented at some angle θ , as shown in Figure 2.6. The mean trace length estimator for this case was introduced by Decker and Mauldon (2006); however, no derivation was given and the trace density estimator was not discussed.

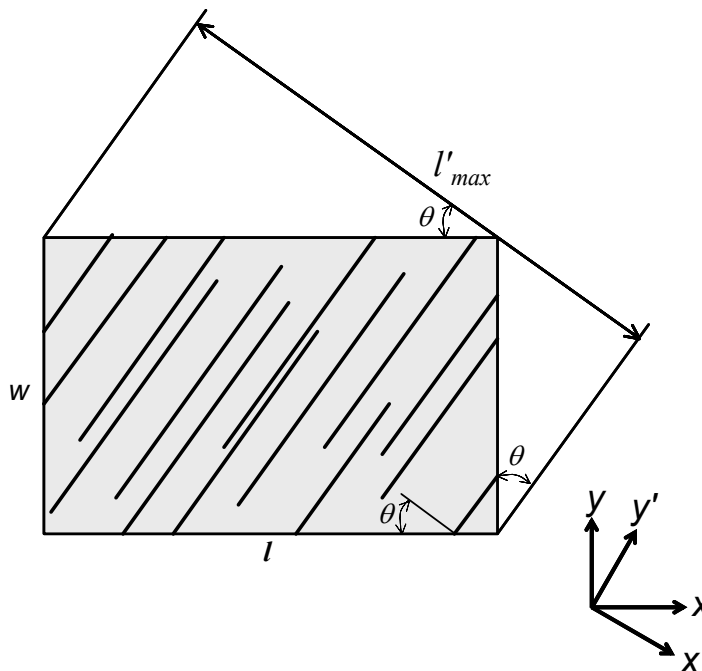


Figure 2.6: Rectangular sampling window with traces oriented at angle θ . Cf. Figure 2.1.

The expected window height μ'_h in the direction y' of the traces, can be computed by dividing the area A by the maximum window length perpendicular to the traces l'_{\max} (Figure 2.7), which yields,

$$\mu'_h = \frac{A}{l'_{\max}} = \frac{lw}{l \cos \theta + w \sin \theta}. \quad (2.24)$$

Substituting the results of Eq. 2.24 into Eqs. 2.14 & 2.18 yields

$$\tilde{\rho} = \mu'_i \rho' \left(\frac{1}{\mu'_i} - \frac{l \cos \theta + w \sin \theta}{lw} \right) \text{ and} \quad (2.25)$$

$$\tilde{\mu}_i = \left(\frac{1}{\mu'_i} - \frac{l \cos \theta + w \sin \theta}{lw} \right)^{-1}. \quad (2.26)$$

Eqs. (2.25) & (2.26) give unique trace density and mean trace length estimators for a rectangular window with traces oriented at an angle θ . If the trace orientation is variable, θ becomes the expected value $E(\theta)$ of θ (Mauldon, 1998), and the estimators are written in the form,

$$\tilde{\rho} = \mu'_i \rho' \left(\frac{1}{\mu'_i} - \frac{l \cos E(\theta) + w \sin E(\theta)}{lw} \right) \text{ and} \quad (2.27)$$

$$\tilde{\mu}_i = \left(\frac{1}{\mu'_i} - \frac{l \cos E(\theta) + w \sin E(\theta)}{lw} \right)^{-1}. \quad (2.28)$$

2.4.2 Circular Windows

The circular sampling window is an important case because it is independent of trace orientation. The expected height of a circle (Figure 2.7) is the same in all directions;

therefore, the trace orientation will not affect the stereological estimators for trace density and mean trace length. The use of circular sampling windows has been suggested to eliminate the affect of orientation distributions on determining density and trace length parameters (e.g., Mauldon et al., 2001; Mauldon et al., 1999b; Rohrbaugh Jr. et al., 2002; Zhang and Einstein, 2000; Zhang et al., 2002).

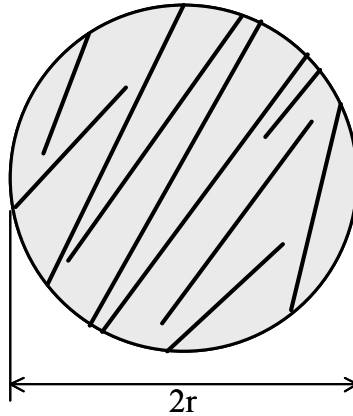


Figure 2.7: Circular sampling window showing traces with a distributed orientation.

The following relationship can be obtained for mean window height of a circular window,

$$\mu'_h = \frac{A}{l'_{\max}} = \frac{\pi r^2}{2r} = \frac{\pi r}{2}. \quad (2.29)$$

Now substituting the results of Eq. 2.31 into Eqs. 2.14 & 2.18

$$\tilde{\rho} = \mu'_i \rho' \left(\frac{1}{\mu'_i} - \frac{2}{\pi r} \right) \text{ and} \quad (2.30)$$

$$\tilde{\mu}_i = \left(\frac{1}{\mu'_i} - \frac{2}{\pi r} \right)^{-1}. \quad (2.31)$$

Eqs. (2.30) & (2.31) give unique trace density and mean trace length estimators for a circular window with traces oriented at any angle and any distribution.

2.4.3 Arbitrary Windows

The cases of rectangular and circular windows, discussed above, are particular cases of the more generic forms of the estimators given in Eqs. 2.14 & 2.18. Examination of these two equations shows that both depend on the mean window height μ'_h in the direction parallel to the traces (direction y' in Figure 2.1). This observation can be employed to derive estimators for convex windows of arbitrary shape, and for non-convex windows where traces will not intersect the window more than once. For windows in these two categories, it is necessary merely to determine mean window height in the y' direction (Figure 2.1), where the mean is taken with respect to the window geometry, weighted by the probability density of direction y' . As an example, Eqs. 2.14 & 2.18 will be applied to the window shown in Figure 2.8, in order to arrive at estimates of trace density and mean population trace length (see Table 2.1).

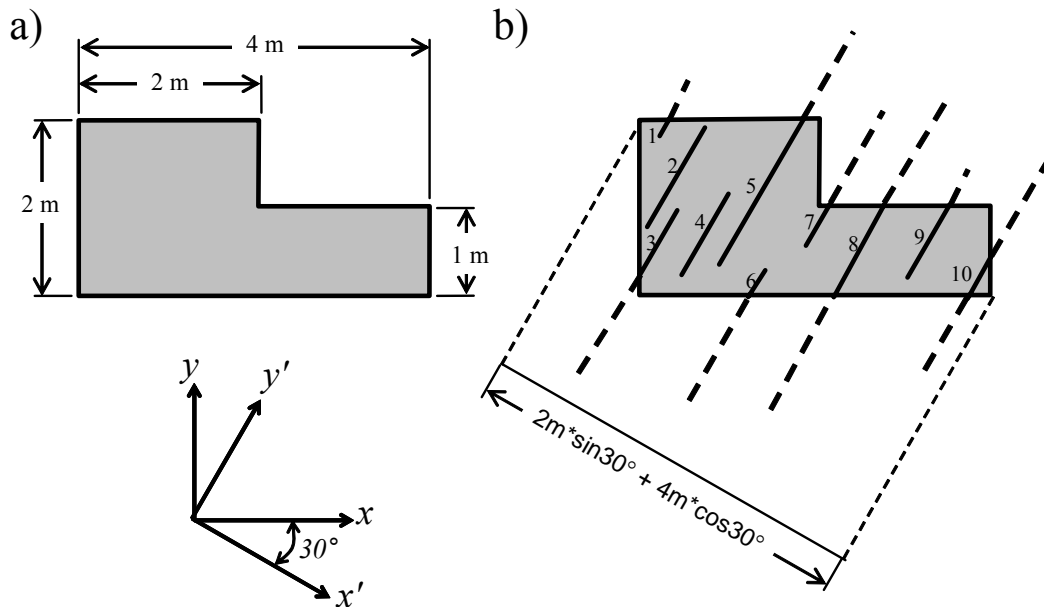


Figure 2.8: a) Example of a non-convex sampling window. b) Sampling window with 10 trace segments, showing l'_{\max} in the direction x' . Measured trace lengths l_i (portions inside the window, in m), in order from 1 to 10, are 0.23, 1.31, 0.85, 1.07, 1.91, 0.36, 0.57, 1.21, 0.96, & 0.58. The sum of these lengths is 9.05 m. Even though the window is in this case non-convex, the estimators are applicable because the orientation of traces is such that they cannot intersect the window more than once. Analysis of this case is given in Table 2.1.

Table 2.1: Application of stereological estimators to the example shown in figure 2.8

Parameter	Figure	Equation	Eq.	Value	Units
L'	2.8b	$\sum l_i = 0.23 + 1.31 + 0.85 + 1.07 + 1.91 + 0.36 + 0.57 + 1.21 + 0.96 + 0.58$	-	9.05	m
A	2.8a	$2m \times 2m + 2m \times 1m$	-	6.00	m ²
l'_{\max}	2.8b	$2m \sin 30 + 4m \cos 30$	-	4.46	m
ρ'	2.8a,b	$\frac{\#traces}{A} = \frac{10}{6m^2}$	See 2.13	1.67	m ⁻²
μ'_t	2.8b	$\frac{L'}{\#traces} = \frac{9.05m}{10}$	-	0.91	m
μ'_h	2.8a	$\frac{A}{l'_{\max}} = \frac{6m^2}{4.46m}$	-	1.34	m
P_{21}	2.8a	$\frac{L'}{A} = \frac{9.05m}{6m^2}$	-		m ⁻¹
$\tilde{\rho}$	na	$\mu'_t \rho' \left(\frac{1}{\mu'_t} - \frac{1}{\mu'_h} \right) = (0.905m)(1.67m^{-2}) \left(\frac{1}{0.905m} - \frac{1}{1.34m} \right)$	2.14	0.54	m ⁻²
$\tilde{\mu}_t$	na	$\left(\frac{1}{\mu'_t} - \frac{1}{\mu'_h} \right)^{-1} = \left(\frac{1}{0.905m} - \frac{1}{1.34m} \right)^{-1}$	2.18	2.79	m

2.5 Field Example

Figure 2.9 is a digital image of a rock exposure near the portal of an abandoned railroad tunnel, referred to herein as Riverbend Tunnel, in Giles County, Virginia. Superposed on the rock face is a circular sampling window with a trace map of visible traces in the window. The trace map was drawn by digitally tracing the fracture traces using the digital image of the rock exposure. The rock outcrop shown is a Cambrian-age dolomite (Bartholomew et al., 2000; Schultz et al., 1986). The rock outcrop displays three discontinuity sets, two near vertical cross-joints (sets 1 & 2) and bedding (set 3) and. The trace map consists of sets 1 & 3. Set 2 is nearly parallel to the window and was not represented. A circular sampling area was used to eliminate orientation bias in the plane.

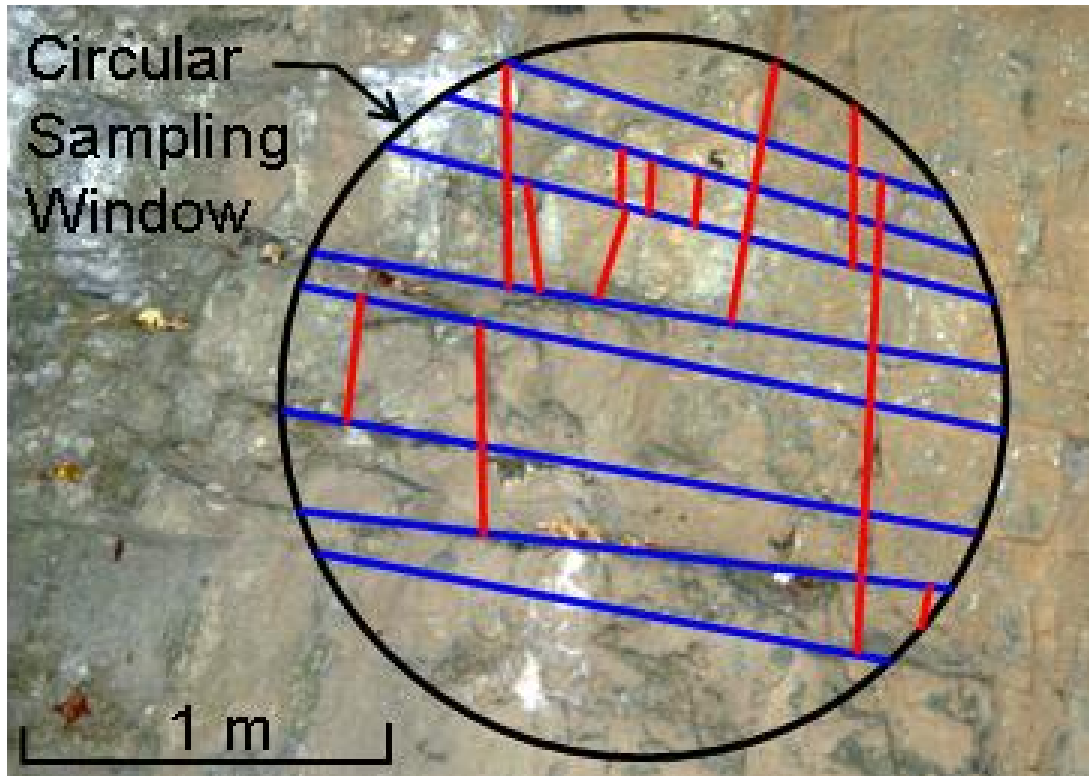


Figure 2.9: Digital image of rock exposure near the portal of Riverbend Tunnel. A circular sampling area is also shown on the image with a trace map of visible traces with set 3/bedding subhorizontal (blue) and set 1 subvertical (red).

The trace density and mean trace length were estimated using both the stereological estimator and the previously published endpoint estimator. Endpoint estimators have been used for both density, intensity, and mean trace length estimates. The endpoint density estimator for a circular sampling window was described by Mauldon et al. (2001) and Rohrbaugh et al. (2002). The endpoint estimator for mean tracelength, using circular windows was described by Mauldon (1998), Mauldon et al. (2001), Rohrbaugh et al. (2002), and Zhang and Einstein (1998). These estimators are given in 2.32 and 2.33 respectively.

$$\tilde{\rho} = \frac{m}{2\pi r^2} \quad \text{and} \quad (2.32)$$

$$\tilde{\mu}_i = \frac{\pi r}{2} \left(\frac{n}{m} \right), \quad (2.33)$$

where:

$\tilde{\rho}$ is the estimated density,

$\tilde{\mu}_t$ is the estimated mean trace length,

r is the radius of the circular sampling window,

n is the total number of intersection between the traces and the circular scanline (Figure 2.10), and

m is the total number of trace endpoints within the sampling window (see Figure 2.10).

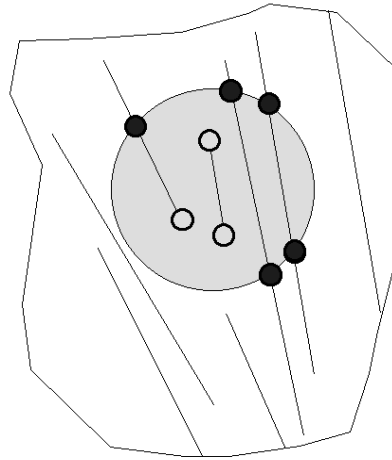


Figure 2.10: Circular sampling window (shaded) with four fracture traces intersecting the window. The closed markers represent the intersections of the traces with the circle ($n = 5$), and the open markers represent the trace endpoints contained in the circle ($m = 3$).

Table 2.2 contains the parameters acquired to evaluate the trace maps using both the stereological and endpoint estimators and the results of applying the estimators. The apparent mean trace length μ'_t was obtained by measuring straight line approximations of the fracture traces. The apparent density ρ' was calculated by counting the total number of traces seen in the window and then dividing by the area of the circular sampling window. The total number of intersections between the traces and the sampling window n and the total number of trace endpoints within the sampling window m were determined by visually counting the endpoints and intersections.

Table 2.2: Parameters obtained from trace map for set 1 & 3 for use with the stereological estimator and the endpoint estimator. The results of the applied estimators are also shown.

Parameter	Symbol	Eq.	Units	Set 1	Set 3 (Bedding)
Radius of Sampling Area	r	-	m	1.0	1.0
Apparent mean trace length	μ'_h	-	m	0.438	1.73
Apparent density	ρ'	-	m ⁻²	3.820	2.55
No. of intersections with circle	n	-	-	4	16
No. of endpoints contained in circle	m	-	-	20	0
Stereological Density Estimator	$\tilde{\rho}$	2.30	m ⁻²	2.75	-0.25
Endpoint Density Estimator	$\tilde{\rho}$	2.32	m ⁻²	3.18	0
Stereological Mean Trace Length Estimator	$\tilde{\mu}_t$	2.31	m	0.61	-17.07
Endpoint Mean Trace Length Estimator	$\tilde{\mu}_t$	2.33	m	0.31	Inf.

The estimates of density for set 1 from the stereological estimator and the endpoint estimator are similar. The mean trace length estimate from the stereological estimator is nearly twice as long as that from the endpoint estimator. It should be noted that the mean trace length estimate given by the endpoint estimator is less than the censored mean (the apparent mean trace length). The censored mean is typically smaller than the actual.

Set 3 is bedding and can be assumed to be very large fractures. The traces, therefore, were continuous in the sampling window and gave no reliable results. In the case of the stereological estimator, the apparent mean trace length of bedding was larger than the mean height of the window and thus negative results were obtained. For the endpoint estimator, there were no endpoints contained in the circle, $m = 0$. Therefore, the estimated density was zero and the estimated mean trace length tended towards infinity. For all field applications, it should be noted that these estimators are not to be used blindly, but should be used with geological judgment.

2.6 Monte Carlo Simulations and Comparison with Endpoint Estimator

Monte Carlo simulations were conducted using an Excel spreadsheet created by the authors. Simulated traces were sampled on a circular sampling window. Fifteen

different scenarios were created with each scenario being simulated 50 times. The scenarios were varied by systematically adjusting the mean trace length μ_t relative to the mean window height μ'_t , the areal intensity P_{21} and the distribution of trace lengths.

Table 2.3 gives the details of each scenario tested. Plots showing the performance of the density estimator and the mean trace length estimator for the scenarios defined in Table 2.3 are given in Appendix 2.A as Figures 2.A1 and 2.A2, respectively.

Table 2.3: Details of Monte Carlo simulation scenarios.

Scenario	Diameter	μ'_t	μ_t	μ_t / μ'_t	P_{21}	Distribution	Standard Deviation
-	m	m	m	-	m^{-1}	-	m
1	10	7.85	1.96	0.25	0.5	Constant	0
2	10	7.85	1.96	0.25	2	Constant	0
3	10	7.85	1.96	0.25	5	Constant	0
4	10	7.85	3.93	0.5	0.5	Constant	0
5	10	7.85	3.93	0.5	2	Constant	0
6	10	7.85	3.93	0.5	5	Constant	0
7	10	7.85	7.85	1	0.5	Constant	0
8	10	7.85	7.85	1	2	Constant	0
9	10	7.85	7.85	1	5	Constant	0
10	10	7.85	39.27	5	0.5	Constant	0
11	10	7.85	39.27	5	2	Constant	0
12	10	7.85	39.27	5	5	Constant	0
13	10	7.85	7.85	1	2	Neg. Exp.	μ_t
14	10	7.85	7.85	1	2	Lognormal	$\mu_t/2$
15	10	7.85	7.85	1	2	Uniform	$\mu_t(\sqrt{3}/2)$

Notes: μ'_t is the mean window height, μ_t is the actual mean trace length of the population, and P_{21} is trace intensity.

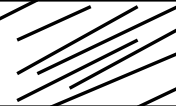
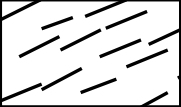
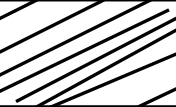
2.6.1 Discussion of results

The main conclusions to be drawn from the Monte Carlo simulations are presented in Tables 2.4 and 2.5.

Density Estimators

Table 2.4 shows a summary of the performance of the stereological and the endpoint estimator for density as a function of trace intensity, mean trace length, and trace length variability. Performance is best with high values of intensity, relatively low values of mean trace length and relatively low trace length variability. For low values of intensity, the endpoint estimator for density slightly outperforms the stereological estimator for density. A similar result is observed for high values of mean trace length, for which the endpoint estimator slightly outperforms the stereological estimator for density. For other conditions, there is no appreciable difference in performance between the two density estimators.

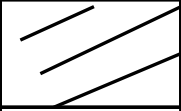
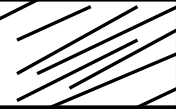
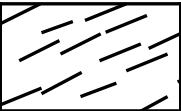
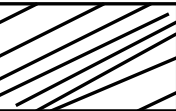
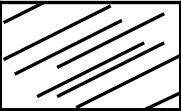
Table 2.4: Summary of performance of stereological and endpoint trace density estimators based on the magnitude of intensity (a), mean trace length (b), and trace length variance (c).

a)	Parameter: Intensity		
	Magnitude	Low	High
	Overall performance	Good	Very Good
	Estimator with best performance	Endpoint	No difference
b)	Parameter: Mean Trace length		
	Magnitude	Low	High
	Overall performance	Very Good	Good
	Estimator with best performance	No difference	Endpoint
c)	Parameter: Trace length Variability		
	Magnitude	Low	High
	Overall performance of estimators	Very Good	Good
	Estimator with best performance	No difference	No difference

Mean trace length estimators

Table 2.5 shows a summary of the performance of the stereological and the endpoint estimator for mean trace length as a function of trace intensity, mean trace length, and trace length variability. Performance is best with high values of intensity, relatively low values of mean trace length and relatively low trace length variability. For low values of mean trace length, the stereological estimator for mean trace length outperforms the endpoint estimator for mean trace length. For high values of mean trace length the endpoint estimator outperforms the stereological estimator for mean trace length. For other conditions, there is no appreciable difference in performance between the two mean trace length estimators.

Table 2.5: Summary of performance of stereological and endpoint mean trace length estimators based on the magnitude of intensity (a), mean trace length (b), and trace length variance (c).

a)	Parameter: Intensity		
	Magnitude	Low	High
	Overall performance	Good	Very Good
	Estimator with best performance	No difference	No difference
b)	Parameter: Mean Trace length		
	Magnitude	Low	High
	Overall performance	Very Good	Good
	Estimator with best performance	Stereological	Endpoint
c)	Parameter: Trace length Variability		
	Magnitude	Low	High
	Overall performance of estimators	Very Good	Good
	Estimator with best performance	No difference	No difference

Further Discussion of Estimators

The stereological estimator for mean trace length (see Eq. 2.18) becomes unstable when the apparent mean trace length μ'_t approaches the mean window height in the direction of the traces μ'_h . This instability can occur for long trace lengths and low values of P_{21} . In some cases the apparent mean trace length μ'_t can actually be greater than the mean window height in the direction of the traces μ'_h . When the above occurs, the estimators return negative values and must be ignored. Several simulations of Scenario 10 failed to produce a stereological estimate for density or mean trace length due to the apparent mean trace length μ'_t being greater than the mean window height μ'_h in the direction of the traces.

The endpoint estimator becomes less accurate when the total number of intersections between the traces and the sampling window n is low, like in the case of short trace lengths and low values of P_{21} . Low numbers of trace endpoints within the sampling window m like in the case of long trace lengths and low values of P_{21} also affect the accuracy of the endpoint estimator, especially for the case when no endpoints are visible within the sampling window ($m = 0$). The endpoint estimator is undefined in this case. For these cases, the stereological estimator will still be able to produce an estimate as long as the apparent mean trace length μ'_t is not greater than or equal to the mean window height in the direction of the traces μ'_h . The above case ($m = 0$) occurred during Scenario 10 four times (Simulations 1, 18, 19, & 20). The stereological estimator produced an estimate three out of the four times with errors of 129, 31 & 59%.

2.7 Conclusions

- Estimators based on stereological principles have been derived for both trace density and mean trace length.
- The estimators are applicable to convex sampling windows of any shape and size, and for non-convex windows as long as traces cannot intersect the window boundary twice
- The stereological estimators for trace density and mean trace length are a unified set of estimators with P_{21} as defined by $P_{21} = L/A$.

- The use of a circular sampling area eliminates any effects that the fracture orientation distribution may have on the stereological estimators for trace density and mean trace length.
- The stereological estimator can be utilized to obtain estimates from field data.
- Performance of the stereological and endpoint estimators for both density and mean trace length is best with high values of P_{21} , low ratios of mean trace length to mean window height and low variance in the distribution of trace length.
- The stereological estimator for mean trace length is typically more accurate than the endpoint estimator for relatively low values of mean trace length, whereas the converse is true for higher values mean trace length.
- The use of the stereological and endpoint estimators together will give engineers and geologists a better estimate of intensity, density, and mean trace length.

2.8 Symbols Used

Symbol	Meaning	Dimension
P_{10}	1d fracture intensity	$[L^{-1}]$
P_{20}	2d (trace) fracture density	$[L^{-2}]$
P_{21}	2d (trace) fracture intensity	$[L^{-1}]$
\tilde{P}_{21}	Estimated 2d (trace) fracture intensity	$[L^{-1}]$
P_{30}	3d fracture density	$[L^{-3}]$
P_{32}	3d fracture intensity	$[L^{-1}]$
x	the horizontal direction	$[-]$
y	the vertical direction	$[-]$
x'	direction perpendicular to traces	$[-]$
y'	direction parallel to traces	$[-]$
t	trace length	$[L]$
μ_t	theoretical mean trace length	$[L]$
μ'_t	apparent mean trace length	$[L]$
$\tilde{\mu}_t$	estimated mean trace length	$[L]$
l	length of sampling window	$[L]$

Symbol	Meaning	Dimension
l'_{\max}	maximum length of sampling window in the direction y'	[L]
μ_h	mean sampling window height in the direction y	[L]
μ'_h	mean sampling window height in the direction y'	[L]
A	area of sampling window	[L ²]
θ	angle from trace normal to horizontal	[deg]
ρ	areal (trace) density	[L ⁻²]
ρ'	apparent density	[L ⁻²]
$\tilde{\rho}$	estimated areal (trace) density	[L ⁻²]
$E(N)$	expected # of traces intersecting a window	[-]
$E(N_0)$	expected # of traces intersecting a window of height zero	[-]
\tilde{N}	# of traces intersecting a window (field count)	[-]
$\tilde{N}_0(y')$	# of traces intersected by a line at position y'	[-]
\tilde{N}_0	mean # of traces intersection a sampling window of height zero (field count)	[-]
$F(t)$	cumulative distribution of trace length	[-]
L'	combined length of visible portions of traces in sampling window	[L]
w	width (height) of rectangular sampling window	[L]
r	Radius of circular sampling window	[L]
n	total # of intersections between the traces and the sampling window border	[L ⁰]
m	total # of trace endpoints within the sampling window	[L ⁰]

2.9 Acknowledgements

The study presented in this paper is based upon work that is supported by the National Science Foundation under grant number CMS 0324889. Any opinions, findings and conclusions or recommendations expressed in this paper are those of the authors and do not necessarily reflect the views of the National Science Foundation.

Appendix 2.A Plots of Monte Carlo Simulations

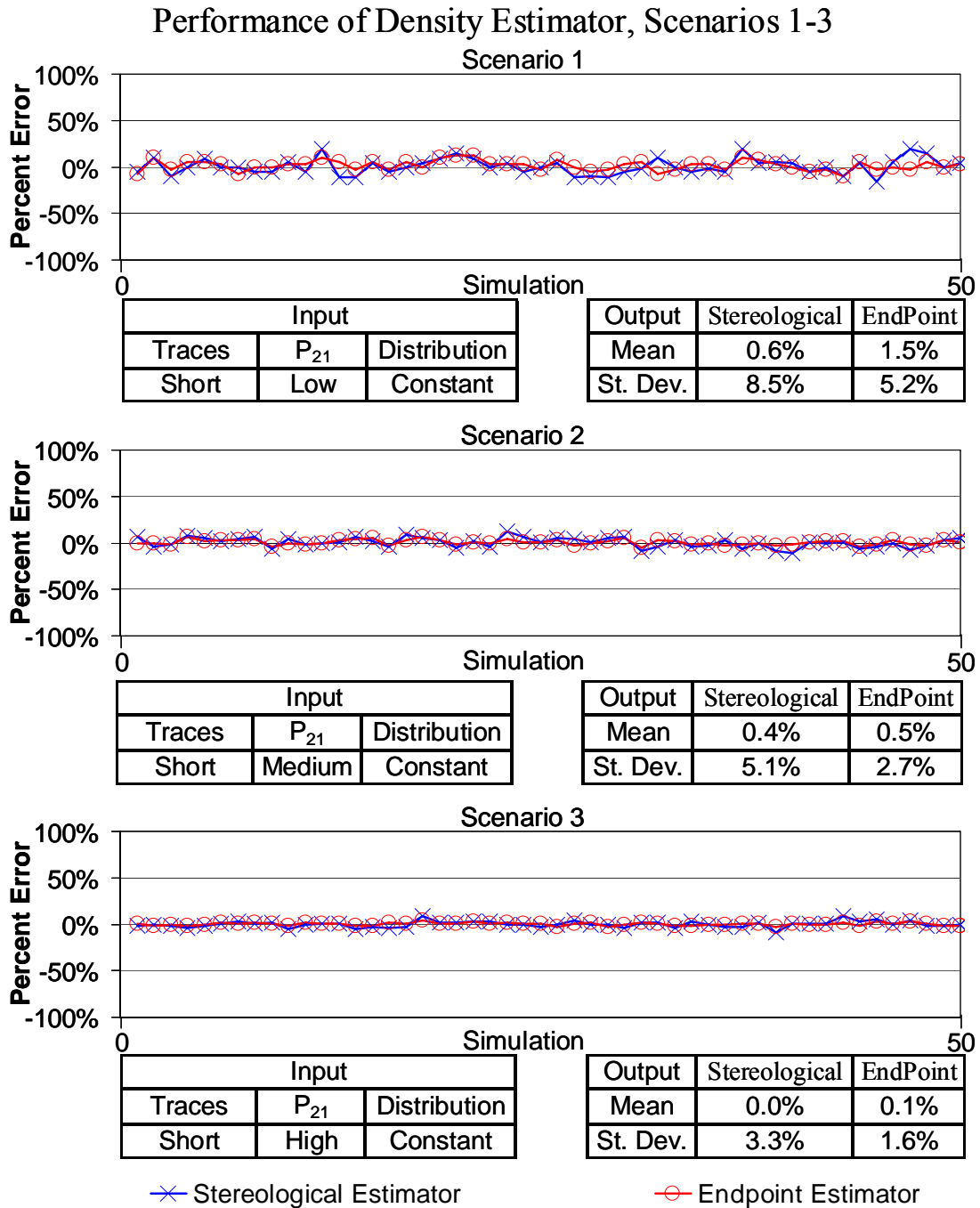


Figure 2.A1a: Performance of Density Estimator. Plot of percent error of density estimate for scenarios 1-5 showing the comparison between the stereological estimator (represented by X's) and the endpoint estimator (represented by O's) for 50 simulations.

Performance of Density Estimator, continued, Scenarios 4-6

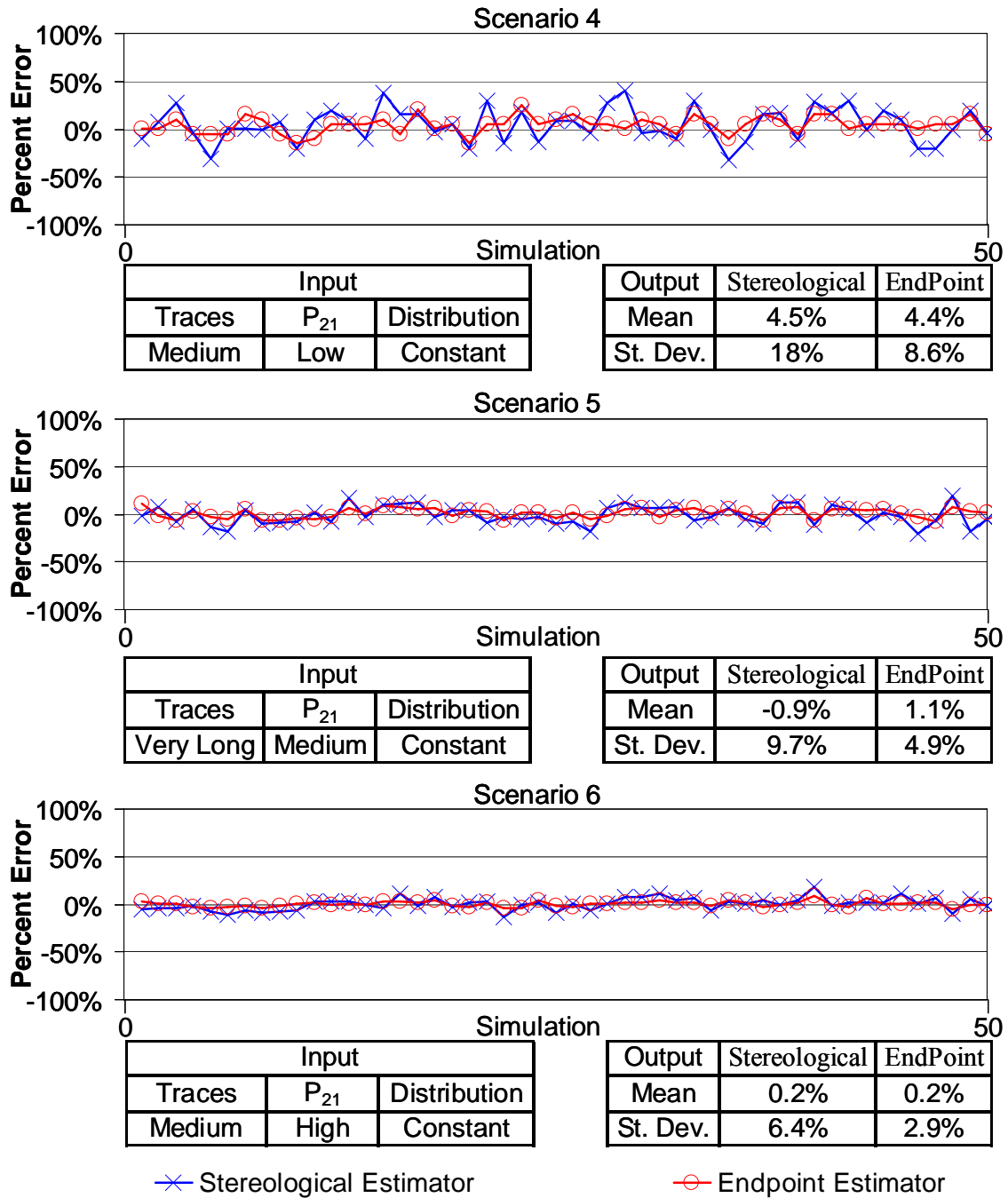


Figure 2.A1b: Performance of Density Estimator, continued. Plot of percent error of density estimate for scenarios 4-6 showing the comparison between the stereological estimator (represented by X's) and the endpoint estimator (represented by O's) for 50 simulations.

Performance of Density Estimator, continued, Scenarios 7-9

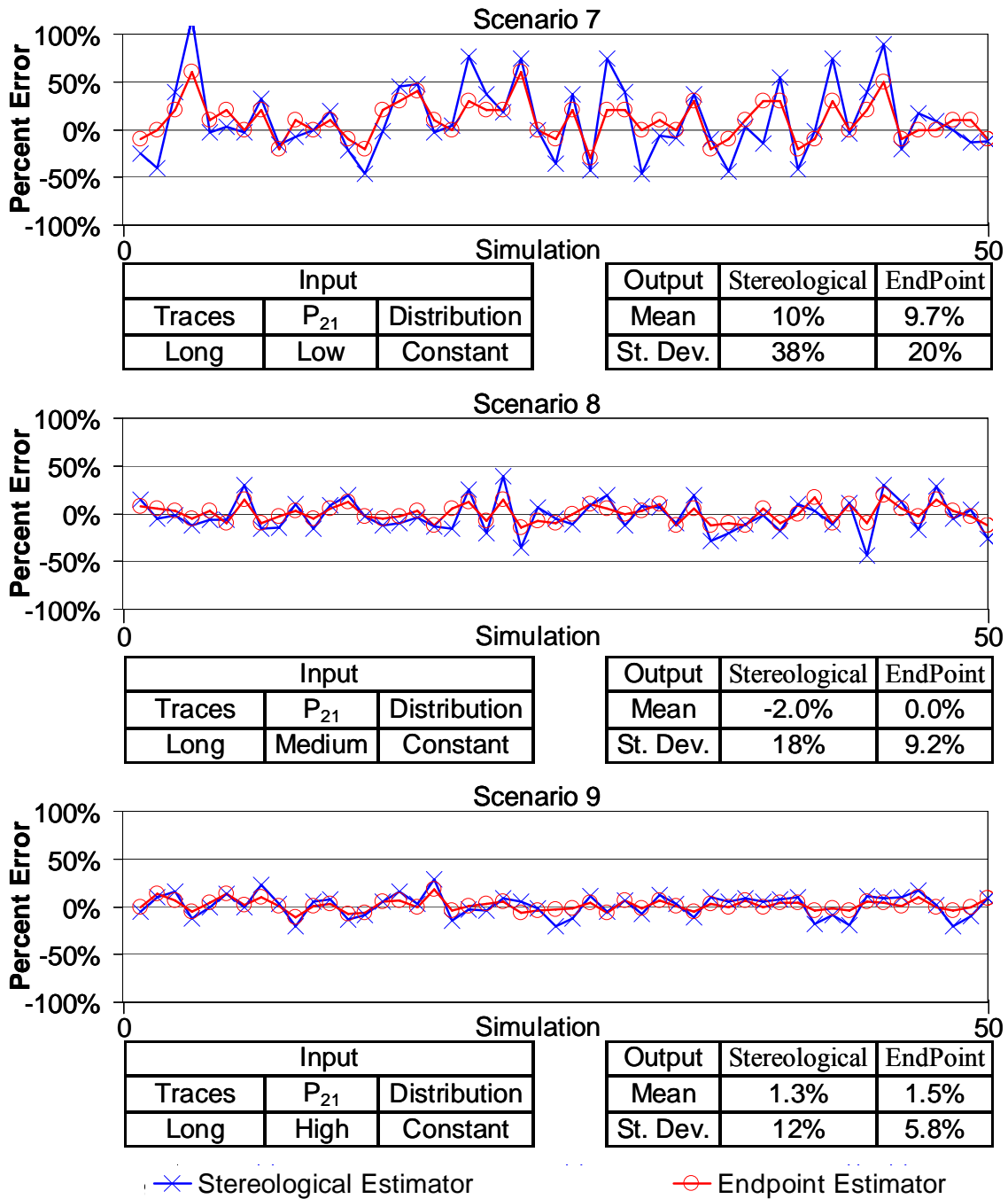


Figure 2.A1c: Performance of Density Estimator, continued. Plot of percent error of density estimate for scenarios 7-9 showing the comparison between the stereological estimator (represented by X's) and the endpoint estimator (represented by O's) for 50 simulations.

Performance of Density Estimator, continued, Scenarios 10-12

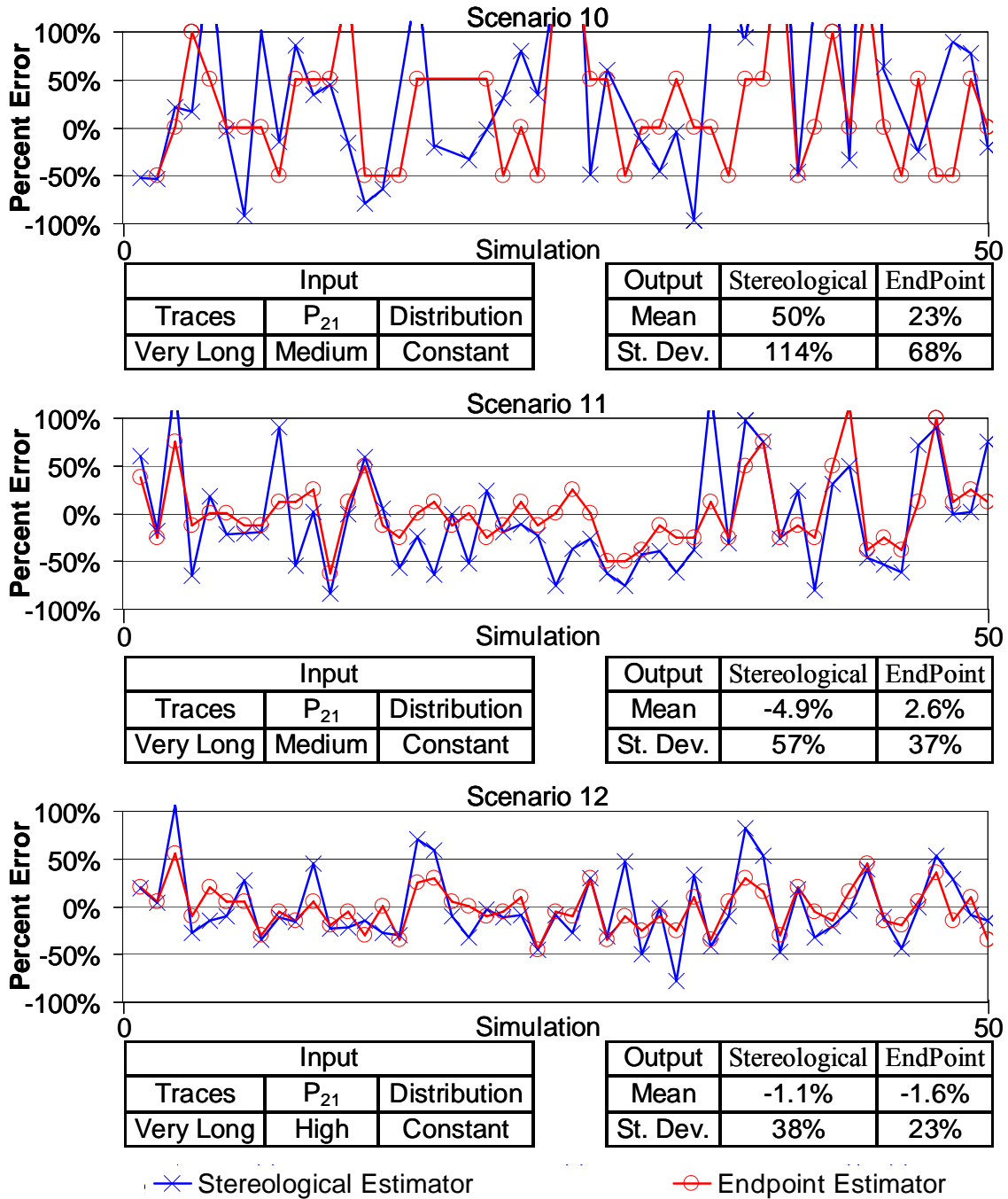


Figure 2.A1d: Performance of Density Estimator, continued. Plot of percent error of density estimate for scenarios 10-12 showing the comparison between the stereological estimator (represented by X's) and the endpoint estimator (represented by O's) for 50 simulations.

Performance of Density Estimator, continued, Scenarios 13-15

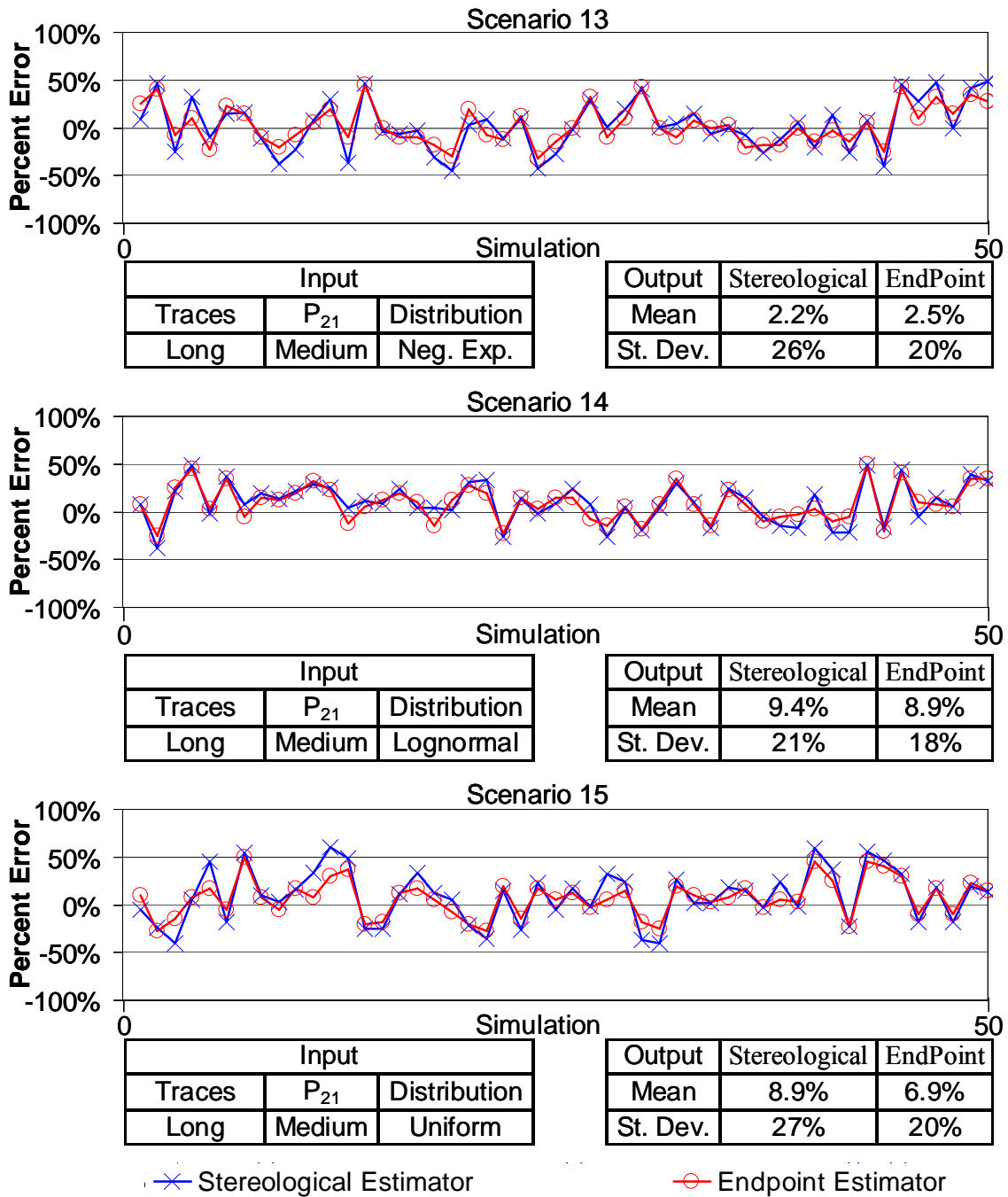


Figure 2.A1e: Performance of Density Estimator, continued. Plot of percent error of density estimate for scenarios 13-15 showing the comparison between the stereological estimator (represented by X's) and the endpoint estimator (represented by O's) for 50 simulations.

Performance of Mean Trace Length Estimator, Scenarios 1-3

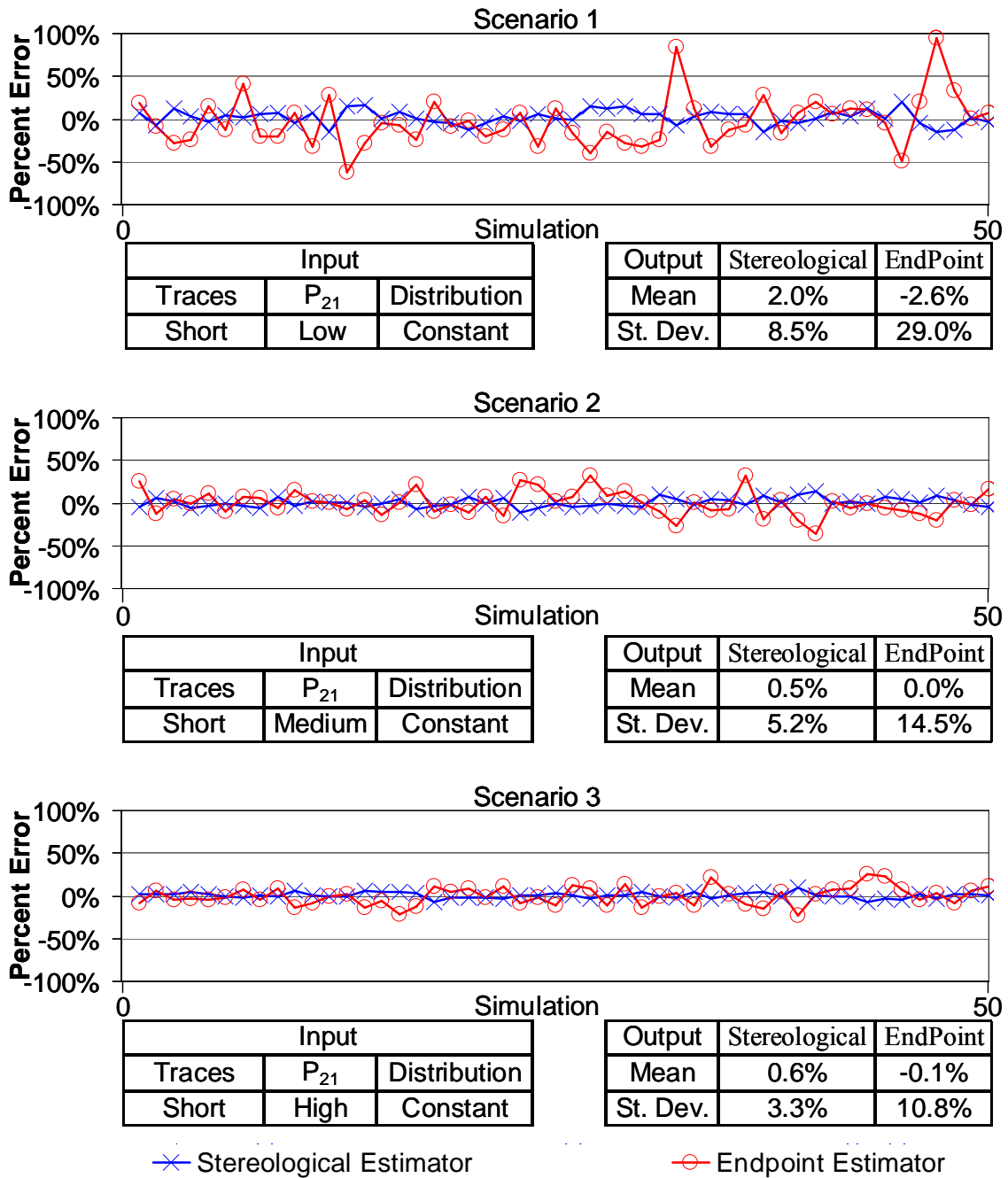


Figure 2.A2a: Performance of Mean Trace Length Estimator. Plot of percent error of mean trace length estimate for scenarios 1-3 showing the comparison between the stereological estimator (represented by X's) and the endpoint estimator (represented by O's) for 50 simulations.

Performance of Mean Trace Length Estimator, continued, Scenarios 4-6

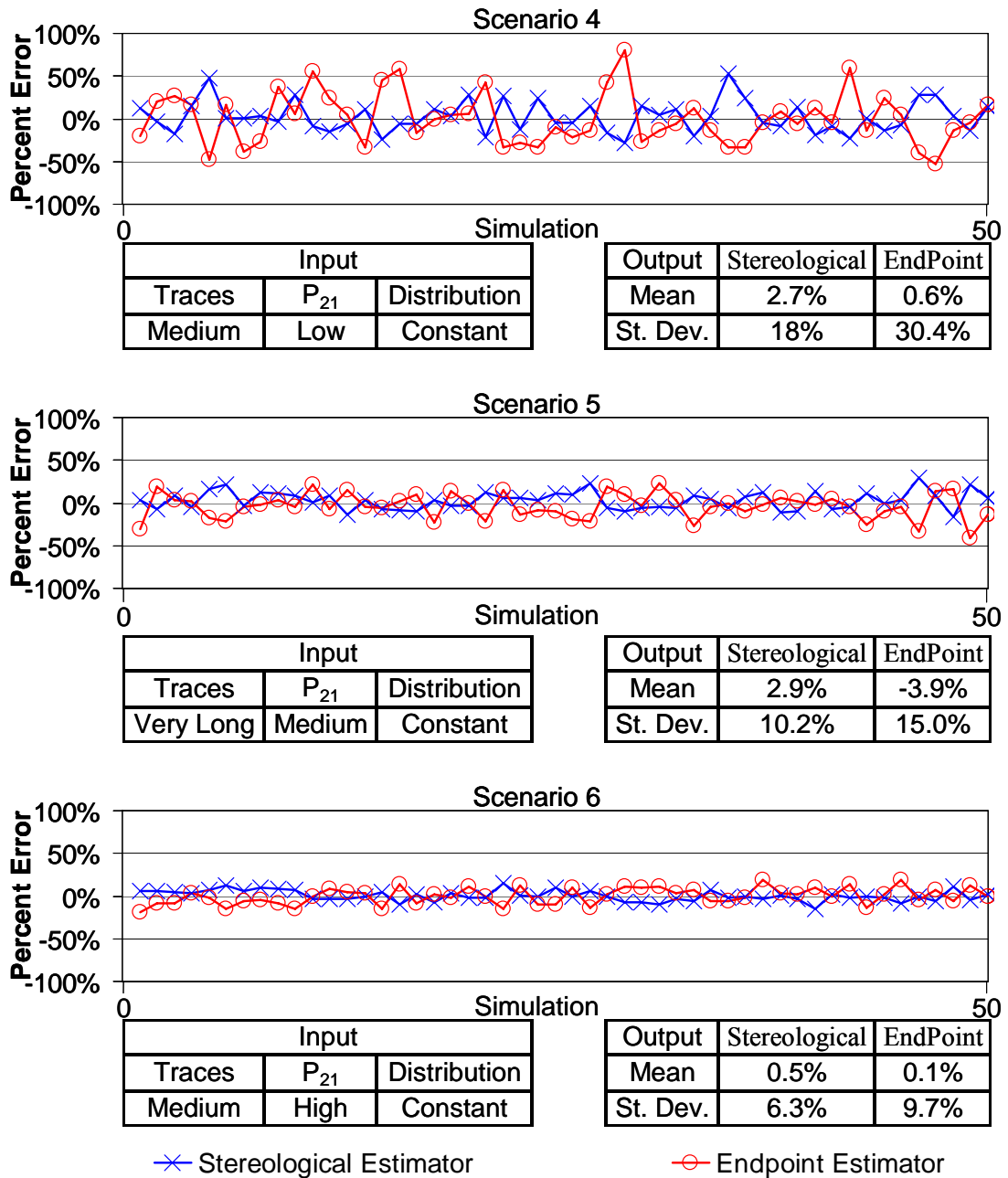


Figure 2.A2b: Performance of Mean Trace Length Estimator, continued. Plot of percent error of mean trace length estimate for scenarios 4-6 showing the comparison between the stereological estimator (represented by X's) and the endpoint estimator (represented by O's) for 50 simulations.

Performance of Mean Trace Length Estimator, continued, Scenarios 7-9

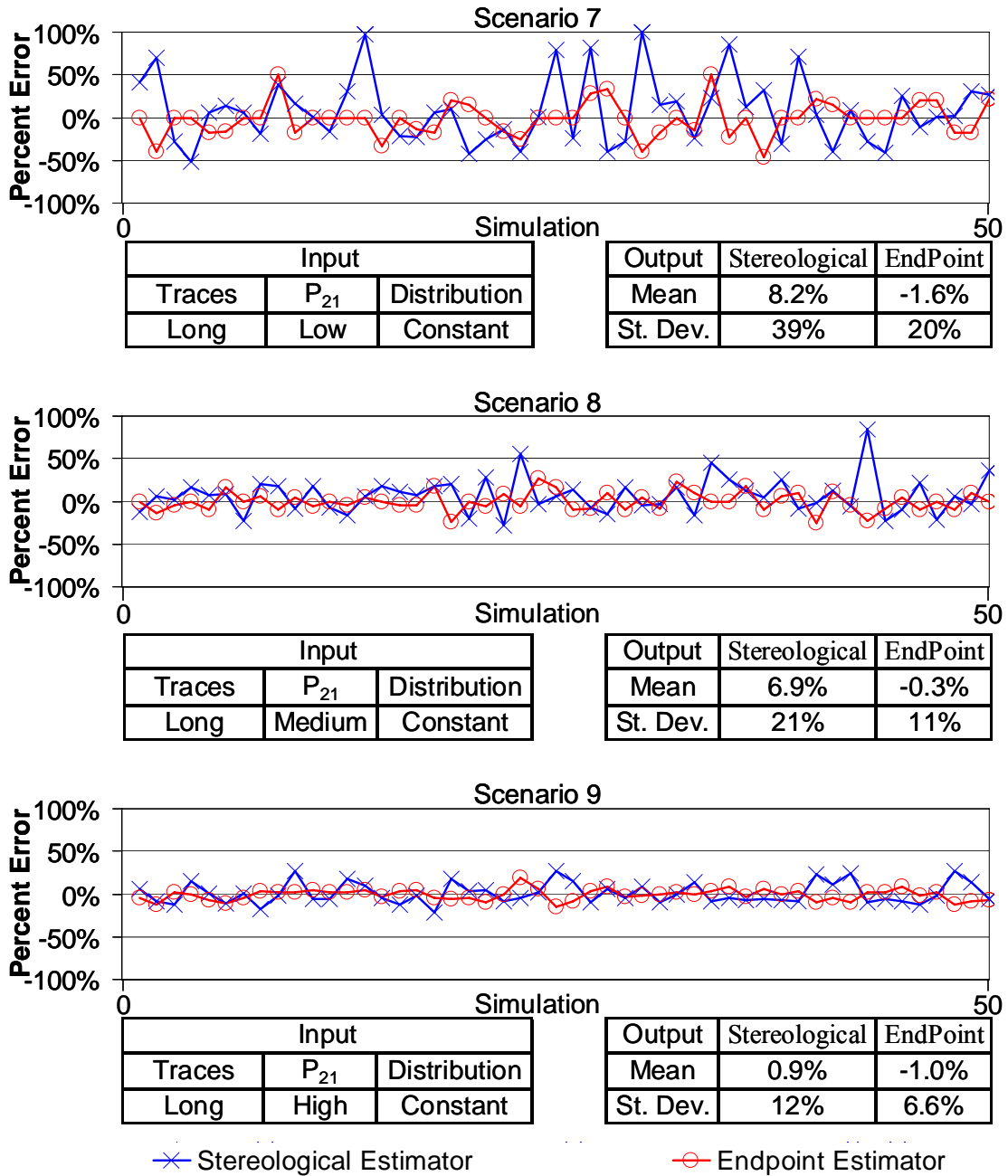


Figure 2.A2c: Performance of Mean Trace Length Estimator, continued. Plot of percent error of mean trace length estimate for scenarios 7-9 showing the comparison between the stereological estimator (represented by X's) and the endpoint estimator (represented by O's) for 50 simulations.

Performance of Mean Trace Length Estimator, continued, Scenarios 10-12

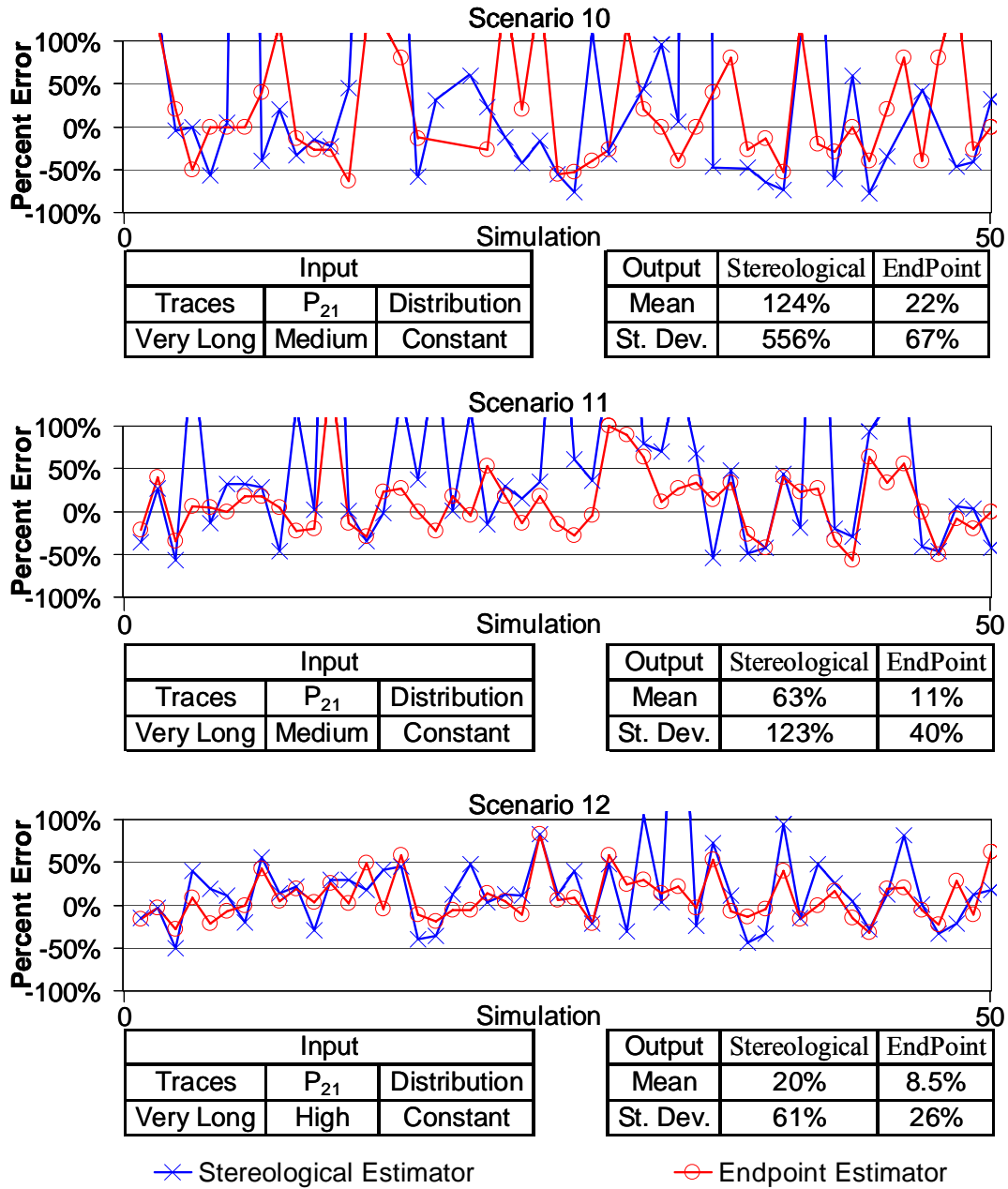


Figure 2.A2d: Performance of Mean Trace Length Estimator, continued. Plot of percent error of mean trace length estimate for scenarios 10-12 showing the comparison between the stereological estimator (represented by X's) and the endpoint estimator (represented by O's) for 50 simulations.

Performance of Mean Trace Length Estimator, continued, Scenarios 13-15

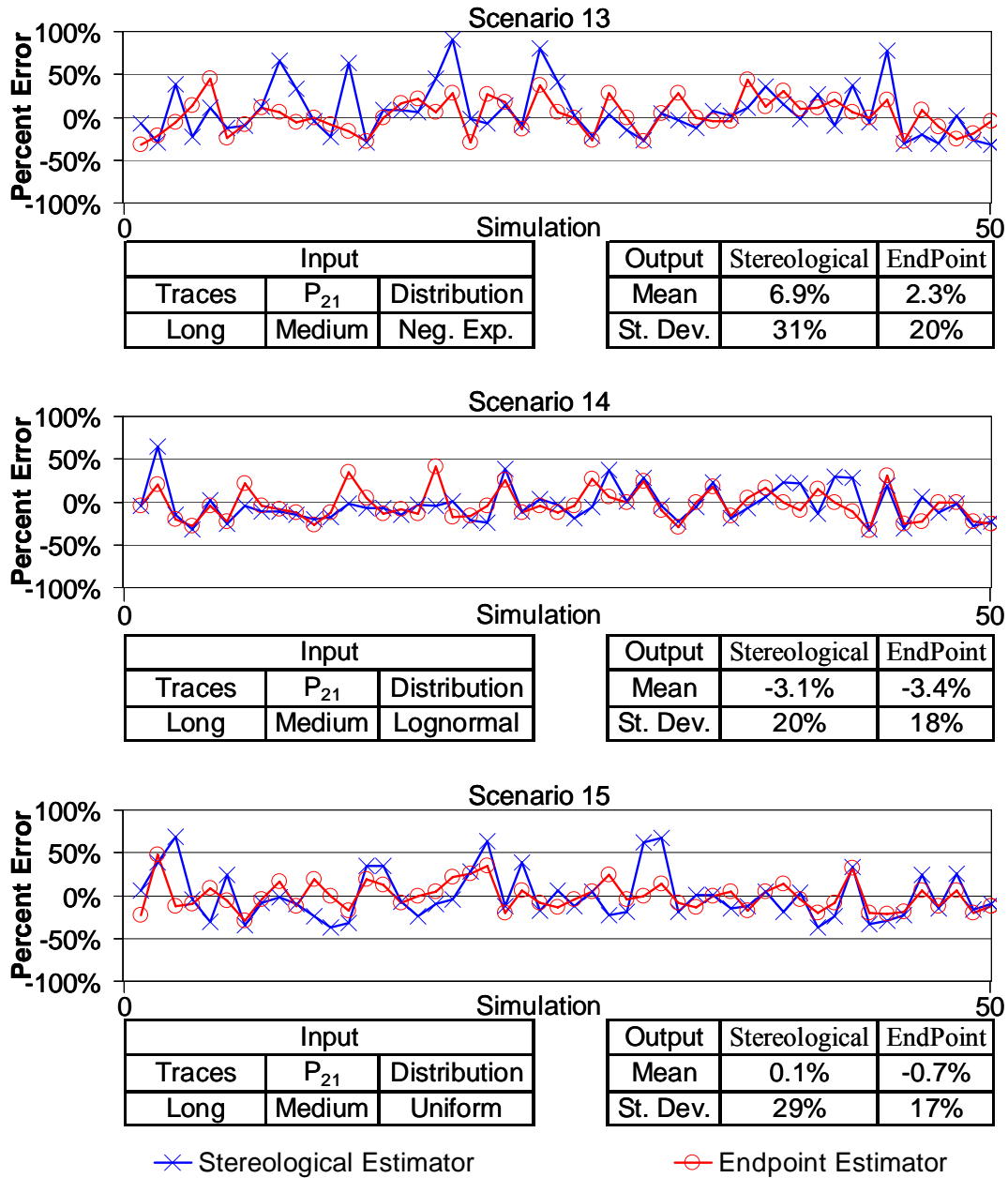


Figure 2.A2e: Performance of Mean Trace Length Estimator, continued. Plot of percent error of mean trace length estimate for scenarios 13-15 showing the comparison between the stereological estimator (represented by X's) and the endpoint estimator (represented by O's) for 50 simulations.

References

- Baecher, G.B., 1980. Progressively Censored Sampling of Rock Joint Traces. *Mathematical Geology*, 12(1): 33-40.
- Baecher, G.B. and Lanney, N.A., 1978. Trace length biases in joint surveys. In: Y.S. Kim (Editor), *Proceedings for the 19th U.S. Symposium on Rock Mechanics*. University of Nevada-Reno, Stateline, Nevada, pp. 56-65.
- Baecher, G.B., Lanney, N.A. and Einstein, H.H., 1977. Statistical description of rock properties and sampling. In: F.D. Wang and G.B. Clark (Editors), *Proceedings of the 18th U.S. Symposium on Rock Mechanics*. Colorado School of Mines, Sante Fe, New Mexico, pp. 5C1.1-5C1.8.
- Bartholomew, M.J., Schultz, A.P., Lewis, S.E., McDowell, R.C. and Henika, W.S., 2000. Digital Geological Map of the Radford 30 by 60 Minute quadrangle, Virginia and West Virginia, Virginia Department of Mines Minerals and Energy, Division of Mineral Resources Preliminary Draft.
- Call, R.D., Savelly, J.P. and Nicholas, D.E., 1976. Estimation of joint set characteristics from surface mapping data. In: W.S. Brown, S.J. Green and W.A. Hustrulid (Editors), *Preprint-Proceedings of the 17th U.S. Symposium on Rock Mechanics*. University of Utah, Snowbird, Utah, pp. 2 B2.1-2 B2.9.
- Cruden, D.M., 1977. Describing the size of discontinuities. *International Journal of Rock Mechanics & Mining Sciences & Geomechanics Abstracts*, 14: 133-137.
- Decker, J.B. and Mauldon, M., 2006. Determining Size and Shape of Fractures from Trace Data using a Differential Evolution Algorithm. In: D.P. Yale, S.C. Holtz, C. Breeds and U. Ozbay (Editors), *Proceedings of the 41st U.S. Symposium on Rock Mechanics*, Golden, Colorado, pp. Paper No. 969.
- Decker, J.B. and Mauldon, M., 2007. Determining Size and Shape of Fractures from Trace Data using a Differential Evolution Algorithm. Not Yet Published.
- Dershowitz, W., Hermanson, J., Follin, S. and Mauldon, M., 2000. Fracture intensity measures in 1-D, 2-D, and 3-D at Aspö, Sweden. In: Girard, Liebman, Breeds and Doe (Editors), *Proceedings of the 4th North American Rock Mechanics Symposium*. Balkema, Rotterdam, Seattle, Washington, pp. 849-853.
- Dershowitz, W.S., 1985. *Rock joint system*, MIT, Cambridge, Mass.
- Dershowitz, W.S. and Herda, H.H., 1992. Interpretation of fracture spacing and intensity. In: J.R. Tillerson and W.R. Wawersik (Editors), *Proceedings of the 33rd U.S. Symposium on Rock Mechanics*. Balkema, Rotterdam, Sante Fe, New Mexico, pp. 757-766.
- Einstein, H.H. and Baecher, G.B., 1983. Probabilistic and statistical methods in engineering geology, specific methods and examples, part 1: exploration. *Rock Mechanics & Rock Engineering*, 16: 39-72.
- Epstein, B., 1954. Truncated Life Tests in the Exponential Case. *Analytical Mathematical Statistics*, 25: 555-564.

- Grossmann, N.F., 1995. About the distribution of the trace lengths of a joint set. In: C. Myer, Goodman, & Tsang (Editor), Proceedings of the Conference of Fractured and Jointed Rock Masses. Balkema, Rotterdam, Lake Tahoe, California, USA, pp. 161-169.
- Kulatilake, P.H.S.W. and Wu, T.H., 1984a. The density of discontinuity traces in sampling windows (Technical Note). International Journal of Rock Mechanics & Mining Sciences & Geomechanics Abstracts, 21(6): 345-347.
- Kulatilake, P.H.S.W. and Wu, T.H., 1984b. Estimation of Mean Trace Length of Discontinuities. Rock Mechanics & Rock Engineering, 17: 215-232.
- Laslett, G.M., 1982a. Censoring and Edge Effects in Areal and Line Transect Sampling of Rock Joint Traces. Mathematical Geology, 14(2): 125-140.
- Laslett, G.M., 1982b. The survival curve under monotone density constraints with application to two dimensional line segment processes. Biometrika, 69(1): 153-160.
- Mauldon, M., 1994. Intersection probabilities of impersistent joints. International Journal of Rock Mechanics & Mining Sciences & Geomechanics Abstracts, 31(2): 108-115.
- Mauldon, M., 1998. Estimating mean fracture trace length and density from observations in convex windows. Rock Mechanics & Rock Engineering, 31(4): 201-216.
- Mauldon, M., 2000. Borehole estimates of fracture size. In: Girard, Liebman, Breeds and Doe (Editors), Proceedings of the 4th North American Rock Mechanics Symposium. Balkema, Rotterdam, Seattle, Washington, pp. 715-721.
- Mauldon, M. and Dershowitz, W.S., 2000. A multi-dimensional system of fracture abundance. Geological Society of America Annual Meeting, Abstracts with Programs, 31: A474.
- Mauldon, M., Dunne, W.M. and Rohrbaugh Jr., M.B., 2001. Circular scanlines and circular windows: new tools for characterizing the geometry of fracture traces. Journal of Structural Geology, 23: 247-258.
- Mauldon, M., Rohrbaugh Jr., M.B., Dunne, W.M. and Lawdermilk, W., 1999a. Fracture intensity estimates using circular scanlines. In: B. Amadei, R.L. Kranz, G.A. Scott and P.H. Smeallie (Editors), Proceedings of the 37th U.S. Symposium on Rock Mechanics. Balkema, Rotterdam, Sante Fe, New Mexico, pp. 777-784.
- Mauldon, M., Rohrbaugh Jr., M.B., Dunne, W.M. and Lawdermilk, W., 1999b. Mean Fracture trace length and density estimators using circular windows. In: B. Amadei, R.L. Kranz, G.A. Scott and P.H. Smeallie (Editors), Proceedings of the 37th U.S. Symposium on Rock Mechanics. Balkema, Rotterdam, Sante Fe, New Mexico, pp. 785-792.
- Pahl, P.J., 1981. Estimating the Mean Length of Discontinuity Traces. International Journal of Rock Mechanics & Mining Sciences & Geomechanics Abstracts, 18(3): 221-228.

- Priest, S.D., 1993. *Discontinuity Analysis for Rock Engineering*. Chapman & Hall, New York, 473 pp.
- Priest, S.D. and Hudson, J.A., 1981. Estimation of Discontinuity Spacing and Trace Length Using Scanline Surveys. *International Journal of Rock Mechanics & Mining Sciences & Geomechanics Abstracts*, 18(3): 183-197.
- Rohrbaugh Jr., M.B., Dunne, W.M. and Mauldon, M., 2002. Estimating fracture trace intensity, density, and mean length using circular scan lines and windows *The American Association of Petroleum Geologists Bulletin*, 86(12): 2087-2102.
- Schultz, A.P., Stanley, C.B., Gathright, I., T.M., Rader, E.K., Bartholomew, M.J., Lewis, S.E. and Evans, N.H., 1986. *Geological Map of Giles County, Virginia*. Publication 69. 1: 50,000-scale colored geologic map., Commonwealth of Virginia Department of Mines, Minerals and Energy-Division of Mineral Resources.
- Song, J.J. and Lee, C.I., 2001. Estimation of joint length distribution using window sampling. *International Journal of Rock Mechanics & Mining Sciences*, 38: 519-528.
- Underwood, E.E., 1970. *Quantitative Stereology*. Addison-Wesley Publishing Company, Reading, MA.
- Warburton, P.M., 1980a. A stereological interpretation of joint trace data. *International Journal of Rock Mechanics & Mining Sciences and Geomechanics Abstracts*, 17: 181-190.
- Warburton, P.M., 1980b. Stereological interpretation of joint trace data: influence of joint shape and implications for geological surveys. *International Journal of Rock Mechanics & Mining Sciences and Geomechanics Abstracts*, 17: 305-316.
- Zhang, L. and Einstein, H.H., 1998. Estimating the mean trace length of rock discontinuities. *Rock Mechanics & Rock Engineering*, 31(4): 217-235.
- Zhang, L. and Einstein, H.H., 2000. Estimating the intensity of rock discontinuities. *International Journal of Rock Mechanics & Mining Sciences & Geomechanics Abstracts*, 37(5): 819-837.
- Zhang, L., Einstein, H.H. and Dershowitz, W.S., 2002. Stereological relationship between trace length and size distribution of elliptical discontinuities. *Geotechnique*, 52(6): 419-433.

This page intentionally left blank.

3 Determining Size and Shape of Fractures from Trace Data using a Differential Evolution Algorithm

Abstract: Fracture length data obtained during geological investigations is typically not a direct measurement of fracture size; instead, it is a measure of the length of the intersection vector between two planes. The statistics of these intersection vectors (traces) are not only affected by the size of the fractures, but also by the shape of the fracture. A new method for obtaining fracture size and shape based on trace data has been developed. The method introduced herein assumes rectangular fractures with constant size and utilizes estimators for mean trace length and an empirical trace length CDF on two or more planes. These two statistical measures are used to define a cost function used with a Differential Evolution algorithm to converge on the best fit mean fracture size and shape. The algorithm has been implemented using an Excel spreadsheet *DEfrac*. The method is demonstrated and tested using simulated fracture sets and field data.

3.1 Introduction

A collaborative research project at Virginia Tech, AMADEUS, deals in part with the semi-automatic collection, interpretation, and visualization of fracture data during tunneling. This paper looks at one component of AMADEUS: the determination of fracture size and shape from trace data.

The size and shape of fractures are important parameters in building fracture models. Data about fractures are commonly obtained by measuring fracture traces visible on rock outcrops and on tunnel walls. There are several limitations to this approach. However, since entire fractures are rarely visible, the use of fracture traces to build fracture models is often the only viable solution. Limitations to the use of fracture trace data include biases during sampling and the fact that the traces do not directly represent the fracture size. Sampling biases have been discussed at length in the literature (Baecher, 1980; Einstein and Baecher, 1983; Kulatilake and Wu, 1984b; Mauldon, 1998; Warburton, 1980a; Warburton, 1980b) and will not be discussed in this paper.

Because traces are random section lines across fractures, mean trace length and trace length distribution do not directly represent the mean fracture length and

distribution (Einstein and Baecher, 1983). Transitioning from trace length estimates to fracture size and shape estimates is a very important step, which can be fairly difficult. Several researchers have developed mathematical models and numerical solutions for this, assuming circular fractures (Grossmann, 1995; Kulatilake and Wu, 1986; Priest, 2004; Song and Lee, 2001; Tonon and Chen, 2005; Villaescusa and Brown, 1992; Warburton, 1980a; Zhang and Einstein, 2000). The assumption of circular fractures has been typically made due to mathematical simplicity (Zhang et al., 2002); however, the assumption of circular shape may be in many cases unrealistic, and the shape of fractures can clearly have an affect on the trace length distribution (Grossmann, 1995). Using the assumption of parallelogram shaped fractures, numerical solutions for fracture size and shape have been described (Grossmann, 1995; Warburton, 1980b). Also an assumption of an elliptical fracture shape has been explored (Zhang et al., 2002), in which fracture size and shape for elliptical fractures are estimated using two or more sampling planes. The complexities of elliptical fractures and the relationship between fracture length and trace length are dealt with by fitting a distribution of hypothetical ellipses to trace length data. All these methods require the assumption of both the trace length distribution and fracture size distribution.

The method presented in this paper assumes rectangular fractures with constant size and orientation. The method requires trace data (estimated mean fracture trace length and an empirical CDF of trace length) on two or more non-parallel planes. Rectangular fractures are commonly encountered in sedimentary rock; for example, bed contained cross joints tend to be rectangular due to termination on primary joints (Baecher et al., 1977; Bai and Pollard, 2000; Cooke and Underwood, 2001; Engelder and Gross, 1993; Gross, 1993; Helgeson and Aydin, 1991; Ruf et al., 1998; Wang et al., 2004; Wang et al., 2005).

The problem of finding the best fit fracture based on trace data from two or more planes is a complex inverse problem. Optimization techniques are used in this research to converge to the best estimate based on the trace data. The optimization technique described here is an Evolution Scheme (a type of Genetic Algorithm) called Differential Evolution (DE) (Price and Storn, 1997; Storn and Price, 1997). An Excel application

DEfrac (Differential Evolution for fractures) that implements the DE algorithm was developed for this research.

This paper will give the derivation of the cost function used for optimization. Then the implementation of the DE algorithm will be explained. Examples will then be shown with fracture populations that follow the model assumptions along with fracture populations that do not. Then an example of implementing the method in the field will be given. This paper is based on previous work by Decker and Mauldon (2006).

3.2 *Fitness Test*

A cost function to measure fitness has been defined based on estimated mean trace length and the empirical trace length CDF on each plane where trace data is obtained.

3.2.1 Mean Trace Length

The mean trace length is estimated in this study using window sample data, by using a point estimator (Mauldon, 1998; Pahl, 1981) and a stereological estimator (Mauldon, 1998). The point estimator (Mauldon, 1998) is

$$\tilde{\mu}_t = \frac{wl}{w \sin \theta + l \cos \theta} \left(\frac{n}{m} \right) \quad (3.1)$$

where $\tilde{\mu}_t$ = estimated mean trace length, w = width of sampling window, l = length of sampling window, θ = angle between side parallel with width and traces (assuming that the orientation is constant), n is the total number of intersections between the traces and the sampling window border, m is the total number of trace endpoints within the sampling window (Mauldon, 1998; Mauldon et al., 2001).

The stereological estimator (Mauldon, 1998), modified for traces at arbitrary orientation relative to the observation window (Decker and Mauldon, 2007b), is given by

$$\tilde{\mu}_t = \left(\frac{1}{\mu'_t} - \frac{w \sin \theta + l \cos \theta}{wl} \right)^{-1}, \tag{3.2}$$

where: $\tilde{\mu}_t$ = estimated mean trace length, μ'_t = apparent mean trace length, w = width of sampling window, l = length of sampling window, and θ = angle between side parallel with width and traces (assuming that the orientation is constant).

The quality of the estimates defined by Eq. 3.1 & 3.2 can be assessed by comparing the estimated mean trace lengths, with the theoretical mean trace lengths produced by assuming the size and shape of rectangular fractures. This comparison yields a measure of how well the assumed size and shape fits the measured data. The derivation of theoretical mean trace lengths as a function of the size and shape of rectangular fractures will be given below

Assume the rock mass around a tunnel contains a set of constant-size rectangular fractures. Then the expected value of the trace on a sampling window is the average length of the vector representing the intersection of the fractures and the planar surface of the window (Figure 3.1).

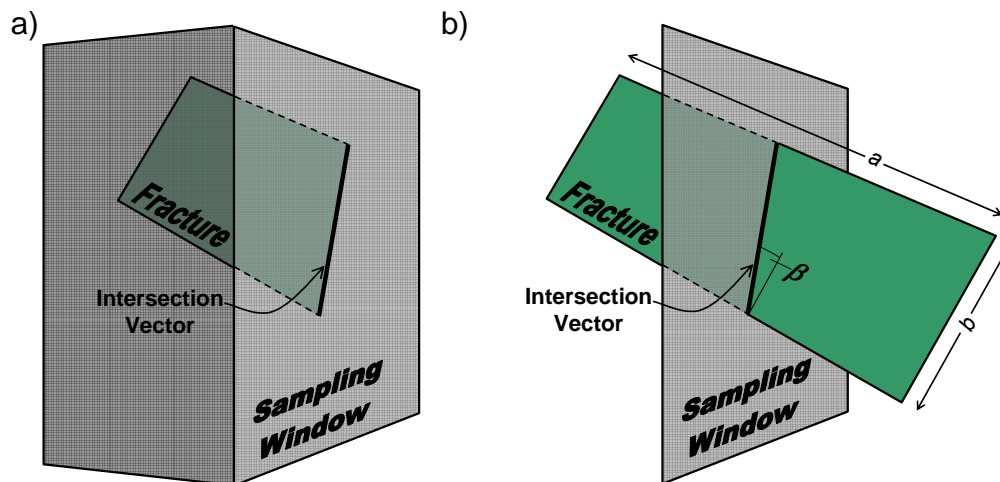


Figure 3.1: Rectangular fracture intersecting a sampling window and creating an intersection vector (trace). a) Shows the intersection vector or fracture trace as seen in the field with portion of fracture shown in rock mass. b) Entire fracture shown, long side a and short side b , and the angle between the intersection vector and side b is denoted β

To determine the average length of this intersection vector, the angle, β , measured in the fracture plane between the intersection vector and the short side b of the fracture, must be obtained (Fig. 3.1). The angle β is a function of the orientation of the sampling plane, the orientation of the fracture, and the orientation of the elongation axis of the fracture (parallel to side a), within its plane. It is assumed that the orientation of the plane and fracture have already been determined. Then the only unknown, is the orientation of the long axis of the rectangular fracture. Once β is obtained, the theoretical mean intersection vector length or mean fracture trace length μ_t is computed as the area of the fracture, divided by the length of the fracture perpendicular to the intersection vector as given by Eq. 3.3 (see Figure 3.2).

$$\mu_t = \frac{ab}{a \sin \beta + b \cos \beta} \tag{3.3}$$

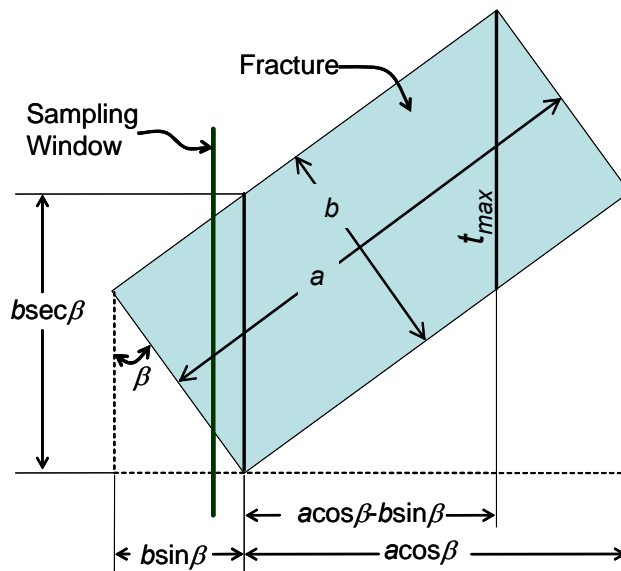


Figure 3.2: Rectangular fracture with side lengths a & b , with $a \geq b$, angle β between intersection vector and side b .

3.2.2 Trace Length Distribution (K-M-trace)

The trace length distribution of window samples is estimated in this study by using the Kaplan-Meier (Kaplan and Meier, 1958) procedure modified for trace data, which will be referred to as the *K-M-trace* procedure. The Kaplan-Meier procedure is

used widely in survival analyses in the medical field (Armitage et al., 2002). The Kaplan-Meier procedure has been applied previously to trace length studies (Laslett, 1982a). The method allows for the development of a nearly unbiased empirical CDF for censored data. The *K-M-trace* method describes two different types of data: *terminations* (uncensored data) and *removals* (censored data). For trace data, censored traces are considered removals and uncensored traces as terminations. Length intervals are chosen so that each interval contains exactly one termination - this is the Product-Limit method of Kaplan-Meier (1958). Basically, each termination is chosen as the upper boundary of the interval, except when the longest length is a removal; in which case the upper boundary of the last interval is set as the longest removal. In this case, therefore, the last interval contains no termination. An empirical CDF (see (Kaplan and Meier, 1958) Proc. 1 & Eq. 2c) can be constructed by solving for the cumulative probability, as follows.

We begin by establishing upper boundaries u_i , ($i=0,1,\dots,k$) on length intervals 1 to k , with each u_i corresponding to the lengths of terminated traces (Figure 3.4). We let r_i and d_i denote, respectively, the removals and terminations to be counted at length u_i . Specifically, r_i is the number of removals in the interval u_i to u_{i+1} and d_i is the number of terminations in the interval u_{i-1} to u_i . Because each u_i corresponds to exactly one termination (presumed to occur just before length u_i), $d_i=1$ for every interval except the last one. The upper boundary u_k of the last interval is the longest observed trace length. If this is a termination then $d_k = 1$ and $r_k = 0$; if it is a removal then $d_k = 0$ and $r_k = 1$.

We let n_i denote the total number of traces observed at length u_i , and we let n'_i denote the number of traces that have not terminated at length u_i , or

$$n'_i = n_i - d_i, \quad (3.4)$$

where d_i equals either 1 or 0, as explained in the preceding paragraph.

The values of n_i can be expressed as follows:

$$n_i = n'_{i-1} - r_{i-1} = (n' - r)_{i-1}, \quad (3.5)$$

where n_0 denotes the total number of traces observed.

The survival probability \tilde{P}_i at each u_i is computed by

$$\tilde{P}_i = (n'_i/n_i)\tilde{P}_{i-1} \tag{3.6}$$

where $\tilde{P}_0 = 1.0$.

The termination probability \tilde{P}'_i is then

$$\tilde{P}'_i = 1 - \tilde{P}_i. \tag{3.7}$$

An example of using the *K-M-trace* procedure for fracture traces is shown for the sampling window in Figure 3.3. Figure 3.4 shows the terminations, removals, and the intervals along a lengthline analogous to a timeline. Table 3.1 shows the application of Eqs. 3.4 thru 3.7 for the example.

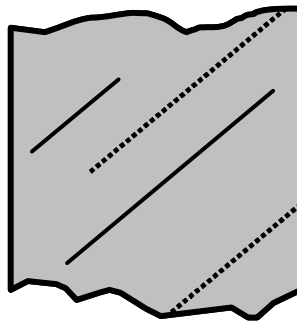


Figure 3.3: Sampling window with 4 visible traces (2 uncensored – solid lines, 2 censored – dotted lines). Lengths of traces given in Figure 3.4.

	d_0	d_1	d_2	
	r_0	r_1	r_2	
	n_0	n_1	n_2	
	n'_0	n'_1	n'_2	...
Removals		1.2	1.8	...
Terminations		0.8	1.9	
Lengths	0.0	1.0	2.0	
	u_0			

Figure 3.4: Example of application of product limit method to trace length data (partial data set).

Table 3.1: Calculated values for example shown in Figure 3.3.

	u_i	d_i	r_i	n_i	n_i'	\tilde{P}	\tilde{P}'_i
0	0	0	0	8	8	1.00	0.00
1	0.8	1	2	8	7	0.88	0.13
2	1.9	1	0	5	4	0.70	0.30

The columns u_i and \tilde{P}'_i constitute the empirically determined CDF up to the longest uncensored trace (Figure 3.5). The method yields a nearly unbiased empirical CDF, but not necessarily in its entirety.

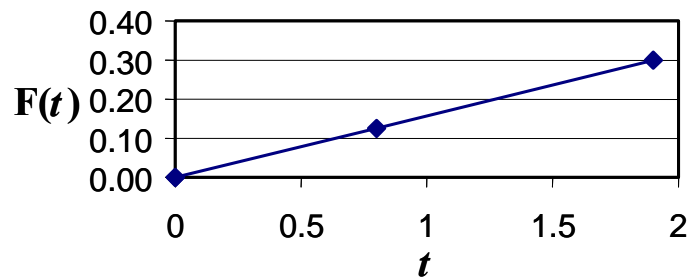


Figure 3.5: Empirical partial CDF for example given in Figure 3.3 and Table 3.1. The linear plot is consistent with constant size rectangular fractures.

The fracture model is now optimized by comparing the empirical CDF with the theoretical CDF's for various assumed sizes and shapes of fractures. The theoretical PDF of intersection (trace) length for rectangular fractures with constant size is derived using Figure 3.2 and is plotted in Figure 3.6. The PDF is constant in the half-closed interval $[0, t_{\max})$, where $t_{\max} = b \sec \beta$ (Figure 3.2).

At $t = t_{\max}$, the PDF is represented by a probability mass. The PDF and probability mass are defined as follows:

$$f(t) = \begin{cases} \psi & \text{for } 0 \leq t < t_{\max} \\ \infty & \text{for } t = t_{\max} \text{ and} \\ 0 & \text{for elsewhere} \end{cases} \quad (3.8)$$

$$P(t = t_{\max}) = \frac{a \cos \beta - b \sin \beta}{a \cos \beta + b \sin \beta}; \quad (3.9)$$

where:

$$t_{\max} = b \sec \beta \text{ and} \tag{3.10}$$

$$\psi = \frac{\sin 2\beta}{a \cos \beta + b \sin \beta} . \tag{3.11}$$

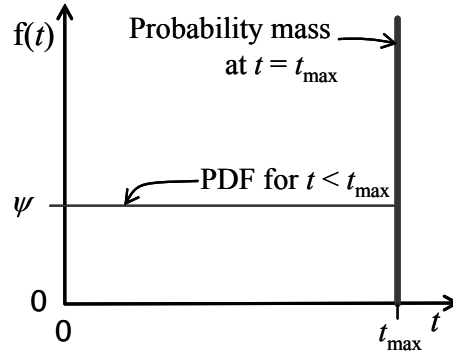


Figure 3.6: PDF of intersection lengths for rectangular fractures intersecting a tunnel face as shown in Figure 3.2.

The theoretical CDF of trace length is given by

$$F(t) = \begin{cases} \psi t & \text{for } 0 \leq t < t_{\max} \\ 1 & \text{for } t \geq t_{\max} \end{cases} \tag{3.12}$$

and is graphed in Figure 3.7.

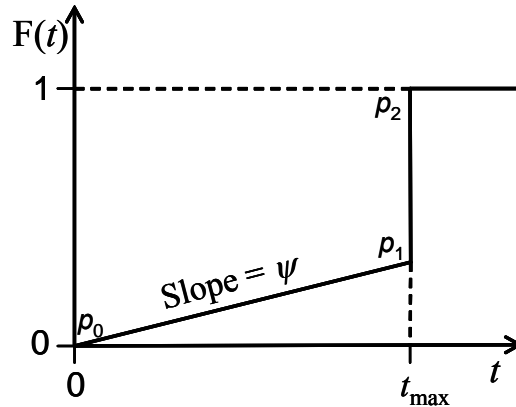


Figure 3.7: CDF of intersection lengths for rectangular fractures intersecting a tunnel face as shown in Figure 3.2. The CDF is linearized in straight line segments from p_0 to p_1 , etc. Section p_0 - p_1 defines the initial slope (ψ)

It should be noted that the slope of the CDF in the interval $[0, t_{\max})$ (Figure 3.6) is equal to the probability ψ , as defined in Eq. 3.11. The fracture model optimization now

proceeds by comparing the theoretical CDF slope ψ , to the empirical CDF slope $\tilde{\psi}$ obtained from the fracture trace data.

Figure 3.8 gives two examples of empirical CDF's constructed using trace data generated with FracWorks (Golder and Associates, 2004). These examples represent two different cases that are related to the size of the sampling window in relation to the traces. For each example the censored empirical CDF, the *K-M-trace* empirical CDF, and the theoretical CDF are shown. The Comparison between the different CDF's demonstrates how effectively the *K-M-trace* method corrects for bias in the data. The first example (a) represents the case when the sampling window is large enough that the entire theoretical CDF can be estimated. In this case, the point p_1 can be estimated (estimated point is labeled p'_1) by fitting the straight-line portion of the CDF. The second example (b) represents the case when a portion of the theoretical CDF is being censored by the sampling window (relatively small window). Note that the initial portion of the empirical data estimates the initial slope of the theoretical CDF well. The *K-M-trace* procedure, for this case, typically gives better results near the beginning (shorter trace lengths) of the CDF where there is more data and then becomes less accurate at longer trace lengths (Figure 3.8). At longer trace lengths the CDF typically drops below the theoretical CDF because the probability is low of having uncensored traces as we approach the maximum trace length that can be seen in the window. The initial portion of the empirical CDF (Figure 3.8) can be computed by identifying the first point (estimated point is labeled p'_1) on the empirical CDF where the slope has a significant change; if there is not a definite change in slope then a best fit line should be used. This point is labeled p'_1 . The initial slope is measured along the straight line segment from the origin (point p_0) to p'_1 . There is some judgment involved in determination of point p'_1 for both cases, but the model is relatively insensitive to its precise location.

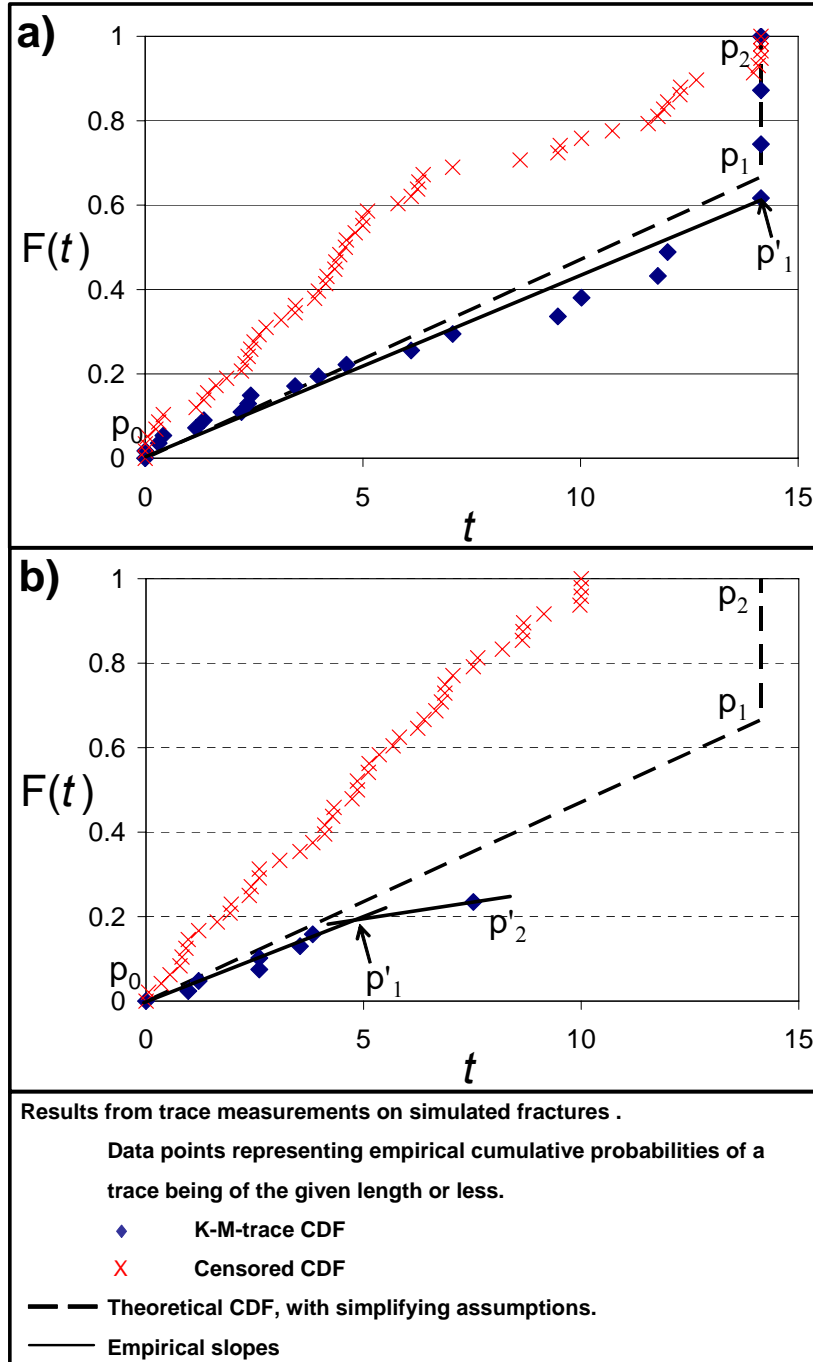


Figure 3.8: Examples of empirical CDF's (uncensored and using *K-M-trace*) shown with the complete theoretical CDF. The section from $p_0 - p'_1$ is the initial straight-line portion of the empirical CDF that will be used to measure, $\tilde{\psi}$. The empirical CDF's were created from simulated data in FracWorks. Example a) ($a = 20, b = 10, \& \beta = 45^\circ$) was sampled on a 20 X 20 m sampling window with 58 total traces visible (21—uncensored, 37—censored). Example b) ($a = 20, b = 10, \& \beta = 45^\circ$) was sampled on a 10 X 10 m sampling window with 48 total traces visible (7—uncensored, 41—censored).

3.2.3 Cost Function

For this study we used two fitness measures: (1) estimated mean trace length (Eqs. 3.1 & 3.2) and (2) estimated slope of the CDF (Figures 3.7 & 3.8). The cost function, (Ravindran et al., 2006; Russell and Norvig, 2003) that was used for optimization, combines the two fitness measures as follows:

$$C(Frac) = \sum_{i=1}^k w_i \left[A \frac{|\mu_{ii} - \tilde{\mu}_{ii}|}{\tilde{\mu}_{ii}} + B \frac{|\psi_i - \tilde{\psi}_i|}{\tilde{\psi}_i} \right] \quad (3.13)$$

where the rectangular fracture $Frac$ is specified in terms of a , b and β (Figure 3.2).

In Eq. (3.13) above, k = number of sampling windows; A & B are weighting factors for the mean trace length and slope of the CDF, respectively ($A + B = 1.0$); and w_i is a weighting factor for different sampling windows ($\sum w_i = 1.0$).

The cost C is a function of a , b , and β of the fracture being tested against the trace data. The cost function uses the weighting factors (A , B , and w_i) to allow the user to account for different levels of confidence in the fitness measures and of data obtained from specific sampling windows.

3.3 Differential Evolution Algorithm

Genetic Algorithms (Holland, 1975; Michalewicz, 1996; Reeves and Rowe, 2003; Russell and Norvig, 2003) are an important type of optimization technique that uses the terminology and processes of biology (selection, crossover, and mutation) to develop search algorithms that produce populations of best fit individuals. Typically, Genetic Algorithms use binary codes to represent integers analogous to a series of genes representing a genome or chromosome.

Evolution Schemes (Michalewicz, 1996; Schwefel, 1995) are a form of Genetic Algorithm that do not use binary codes, but instead use floating point numbers. Differential Evolution (DE) is an extremely simple yet powerful Evolution Scheme (Price and Storn, 1997; Price et al., 2005; Storn and Price, 1997). DE has found many uses in

optimization in engineering such as digital filter design (Price et al., 2005), optimization of water pumping systems (Babu and Angira, 2003), neural network learning (Ilonen et al., 2003), location of earthquake epicenters (Ruzek and Kvasnicka, 2001), and many others (Storn, 2007). DE has also been applied in fracture characterization including determination of fracture orientation (Kemeny and Post, 2003) and fracture size and shape (Decker and Mauldon, 2006).

3.3.1 DE Algorithm

The DE algorithm within *DEfrac* (Figure 3.9), uses evolutionary processes of mutation and crossover to search for best fit individuals. The algorithm is initiated by randomly generating a number (NP) of individuals. In *DEfrac*, NP is set at 30, which is 10 times the number of variables. The initial variables are chosen randomly; the initial range for a (length) is 0 to 5 times the largest estimated mean trace length, for b (width) is 0 to value of a , and elongation trend is 0 to 180° . These randomly generated individuals make up what is called the *Target Vector* (Figure 3.9). During each generation within *DEfrac*, all individuals in the *Target Vector* generate offspring through a process of mutation and crossover. The mutated individual involved in crossover with the *Target Vector* individual is created by randomly choosing three other individuals in the *Target Vector* and then utilizing the mutation scheme:

$$X_i^m = X_A + F(X_B - X_C). \quad (3.14)$$

The above expression refers to mutation of a single “gene” that controls a single parameter. The mutated individual X_i^m is a composite of a randomly selected individual X_A and the difference between two other randomly selected individuals (X_B and X_C) multiplied by a scaling factor F . The resulting mutated gene is then involved in crossover with the original gene. The term Differential Evolution refers to the quantity $X_B - X_C$ involved in mutation. The resulting mutated individuals have non-integer representation of parameters, in contrast to the classic genetic algorithms described by Holland (1975)

Crossover of parameters is controlled by a user defined constant CR (crossover rate), which ranges from 0 to 1; a random number $randnum$ generated for each parameter, which ranges from 0 to 1; and a random integer $randint$ generated only once for each individual, which ranges 1 to the number of parameters. The crossover is defined as follows

$$x'_{ij} = \begin{cases} x_{ij}^m & \text{if } randnum \leq CR \text{ or if } randint = j \\ x_{ij} & \text{if } randnum > CR \text{ or if } randint \neq j \end{cases} \quad (3.15)$$

The CR is compared with $randnum$. If CR is greater than or equal to $randnum$ then the parameter is taken from the mutated individual. If CR is less than $randnum$ it is taken from the *Target Vector* individual. The random integer $randint$ forces at least one parameter to be from the mutated individual, to ensure diversity in the population.

Once mutation and crossover have occurred, a *Trial Vector* is defined with all the new individuals. The cost of these individuals in the *Trial Vector* is computed and compared with the cost of the individuals from the *Target Vector*. The lowest cost individual is carried over to a new *Target Vector*. This new *Target Vector* is then ready to run through another generation.

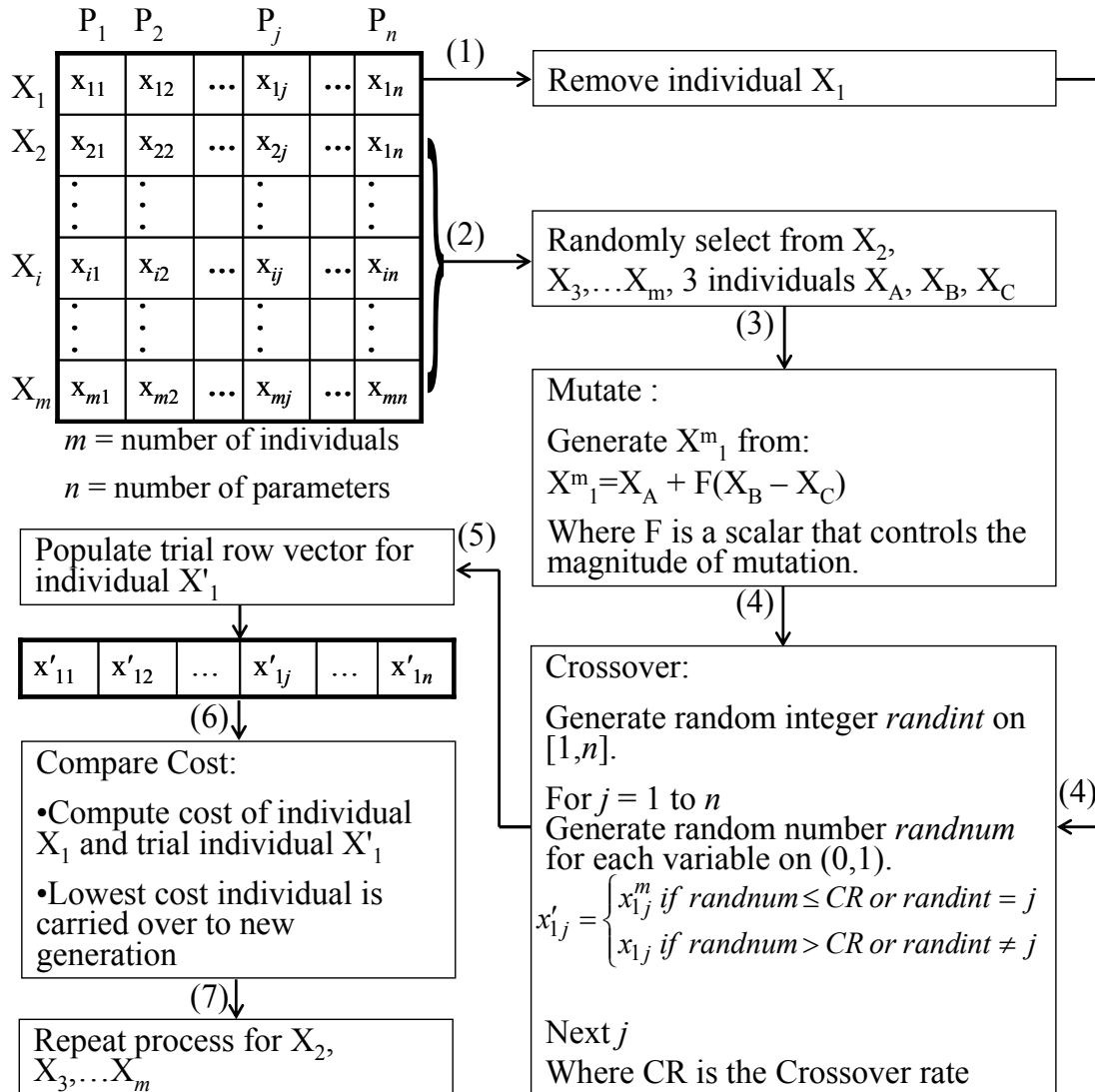


Figure 3.9: Schematic of one generation within a Differential Evolution algorithm for individual X_1 .

3.3.2 DEfrac

The user interface sheet for *DEfrac* consists of two input tables, one output table, and three macro buttons (see Figure 3.10). The first input table is for the variables that control the behavior of the DE algorithm (F , CR , number of generations, and number of runs). The second input table is for all the trace data input (dip and dip direction of sampling window planes, mean trace length estimators, and the slope of the CDF), mean set orientation, and weighting factors to be used in the cost function. The output table gives the average cost of the present *Target Vector*, the coefficient of variation of the

costs of the *Target Vector*, mean a (length), mean b (width), mean equivalent radius, mean aspect ratio, mean elongation trend and plunge, and a generation number. The macro button *First Generation* initializes the population and runs the first generation. The macro button *Single Run* loops through generations until the specified number of generations is met. The macro button *Multiple Runs* allows a *DEfrac* analysis to be run multiple times while recording, on a separate spreadsheet, the output for each run for statistical analysis. The processing time is extremely efficient, running 100 generations in less than 20 seconds on a typical desktop computer.

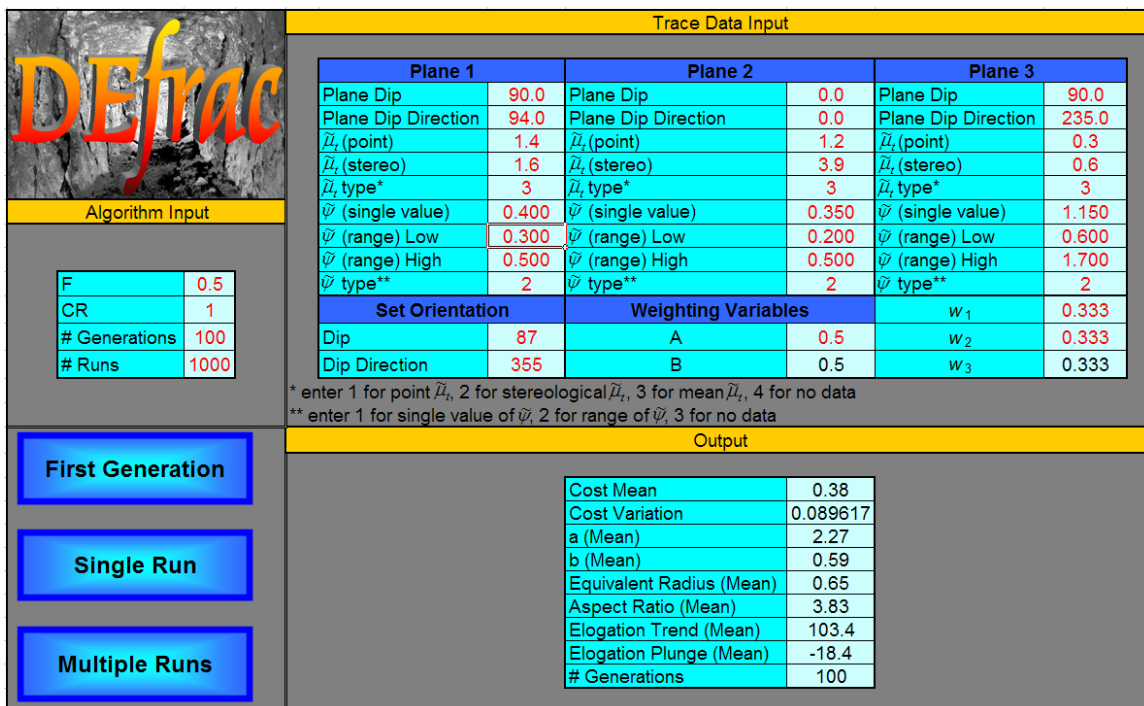


Figure 3.10: User interface for *DEfrac* in Excel.

3.4 Examples

In this section, 4 examples will be given to demonstrate the effectiveness of the method. The examples use fracture populations generated within FracWorks (Golder and Associates, 2004) (Figure 3.11). All of the fracture populations had a dip of 30°, a dip direction of 30°, a width (b) of 10m, a 3d intensity (P_{32}) of 1, an elongation trend of 60°, and an elongation plunge of 26°. The first three examples use populations of fractures that are rectangular, constant size, and constant orientation. These conditions match the

assumptions made to derive the *DEfrac* method. The only parameter varied between these three examples was the fracture aspect ratio. The other example (4) had a fracture population that did not follow the simplifying assumptions of constant orientation. Table 3.2 gives the fracture set parameters that are varied for each example.

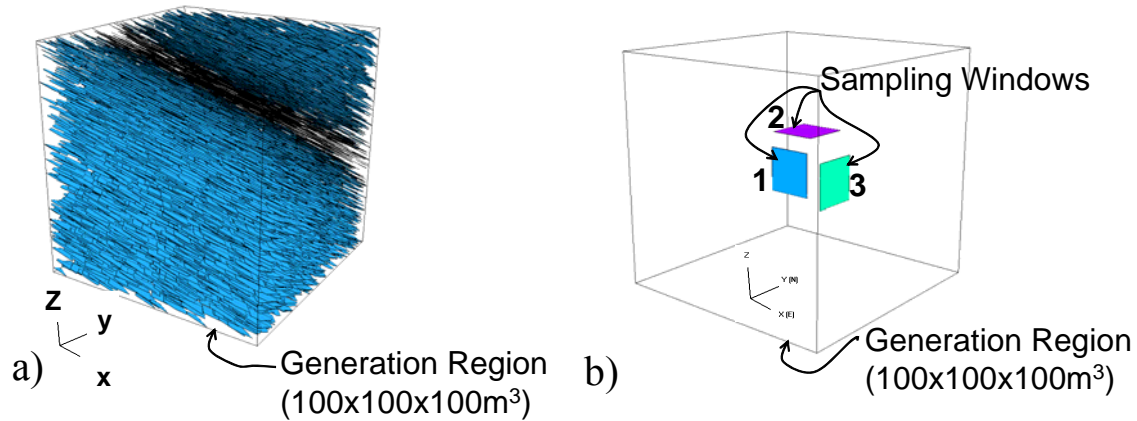


Figure 3.11: a) Population of fractures for example 1 generated within FracWorks. Fractures generated inside and cut by a 100x100x100m³ generation region. b) Location and orientation of rectangular sampling windows used to sample fracture population in FracWorks. Traces are shown on sampling windows.

Table 3.2: Varied fracture set parameters for Examples 1-4.

Example Number	Length, <i>a</i> (m)	Aspect Ratio	Shape	Size Distribution	Orientation Distribution
1	10	1	Rectangular	Constant	Constant
2	20	2	Rectangular	Constant	Constant
3	50	5	Rectangular	Constant	Constant
4	20	2	Rectangular	Constant	Fisher ($\kappa = 30$)

Each fracture population was generated using a 100x100x100m³ generation region (see Figure 3.11). The fractures were then sampled on three orthogonal rectangular sampling windows 20m high and 20m long (see Figure 3.11). Using the data obtained on these planes, mean trace lengths $\tilde{\mu}_i$ were estimated and empirical trace length CDF's were constructed and used to obtain estimates for $\tilde{\psi}$. These estimates were then used

within *DEfrac* to obtain best fit estimates of the fracture size and shape. Examples 1-3 were tested using the average $\tilde{\mu}_i$ for three different values of the weighting factors A & B with the weighting factor w_i set equally for all sampling windows (Tables 3.4, 3.6, & 3.8). The values were as follows: $A = 0.5$ & $B = 0.5$, $A = 0.9$ & $B = 0.1$, and $A = 0.1$ & $B = 0.9$. It was found that $A = 0.5$ & $B = 0.5$ typically gave better results than the other combinations. Using $A = 0.5$ & $B = 0.5$, other tests were run using the point mean trace estimator, the stereological mean trace estimator, and the average of the two estimators with the weighting factors, w_i , based on the ratio of traces on a window to total traces on all three windows. Example 4 was tested with the weighting factors A & B equal and w_i all equal. Also for Example 4 the average of the two mean trace length estimators was used. For each test the number of generations was 60, CR was 1, and F was 0.5.

3.4.1 Examples 1-3

Examples 1, 2, & 3 are varied only by the Aspect Ratio, which is set at 1, 2, & 5, respectively.

Example 1

Table 3.3 gives the trace data obtained from the sampling window used for input into *DEfrac*. The results from Example 1 are shown in Table 3.4 and Figure 3.12. The results of the tests are similar, with Test 1 having the best estimate for size and Test 3 the best estimate of elongation direction. The tests produced elongation directions that were either near or approximately 90° from the actual elongation direction; because the aspect ratio was 1 (square). Figure 3.12 shows the evolving mean fracture within the *DEfrac* process at different generations, related to the actual fracture size and shape of fractures in the sample population. Figure 3.12 also visually demonstrates the convergence of *DEfrac* after 60 generations; the optimized fracture barely changes from generations 20 to 60.

Table 3.3: Data obtained from sampling windows used as input into the *DEfrac* software for Example 1.

Trace Data	Units	Window 1	Window 2	Window 3
# Traces	-	106	47	92
Plane Dip	°	90	0	90
Plane Dip Direction	°	0	0	90
$\tilde{\mu}_i$ (point)	m	6.68	9.09	8.54
$\tilde{\mu}_i$ (stereo)	m	7.72	7.04	6.73
$\tilde{\psi}$	rise/run	0.0598	0.0585	0.0572

Table 3.4: Results of Example 1 (6 tests).

		Test					
		1	2	3	4	5	6
Input	<i>A</i>	0.5	0.9	0.1	0.5	0.5	0.5
	<i>B</i>	0.5	0.1	0.9	0.5	0.5	0.5
	w_1	0.33	0.33	0.33	0.33	0.33	0.43
	w_2	0.33	0.33	0.33	0.33	0.33	0.19
	w_3	0.33	0.33	0.33	0.33	0.33	0.38
	$\tilde{\mu}_i$	avg.	avg.	avg.	point	stereo	avg.
Output	<i>a, m</i>	12.27	12.69	13.49	13.47	12.91	12.32
	<i>b, m</i>	8.70	8.67	7.59	7.65	8.28	8.70
	Aspect ratio	1.41	1.46	1.78	1.76	1.56	1.42
	Elongation Trend, °	147.7	145.6	149.4	149.4	57.5	147.4
	Elongation Plunge, °	-13.5	-12.5	-14.2	-14.2	26.3	-13.3

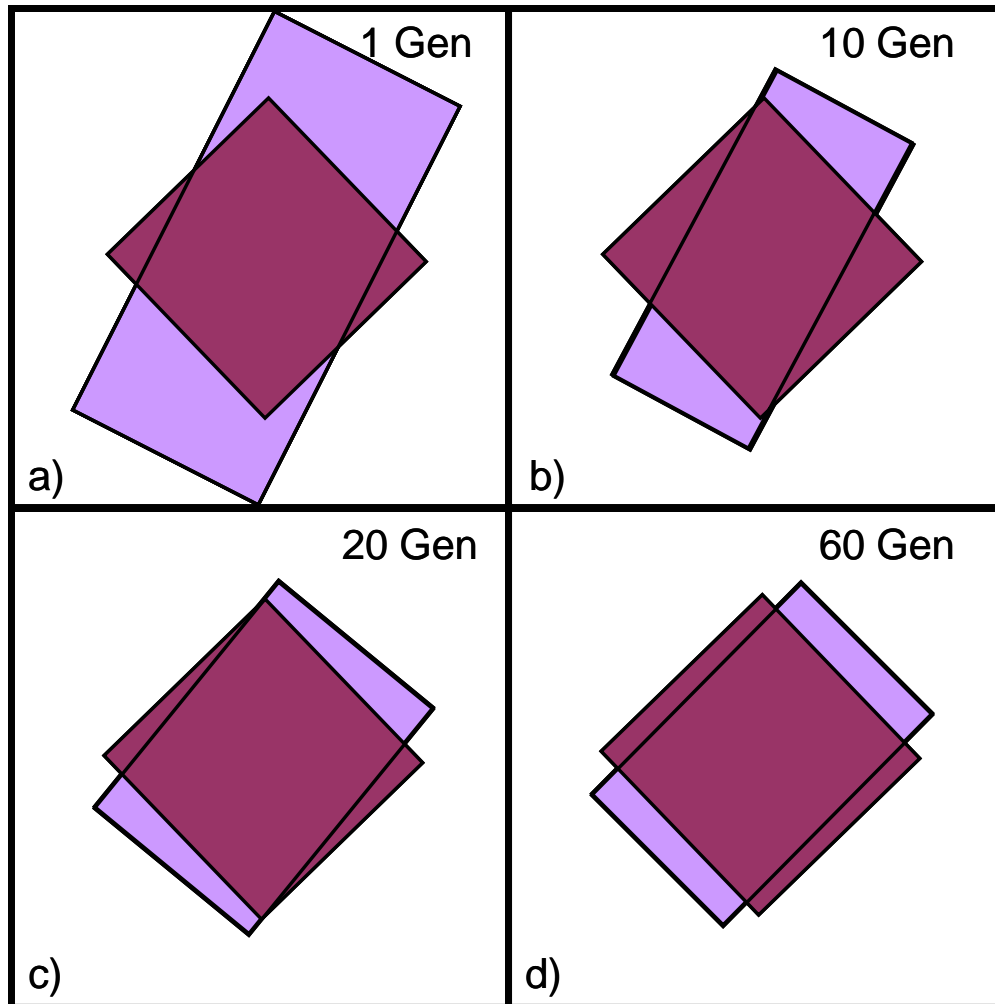


Figure 3.12: Evolving estimate of fracture size and shape for Example 1. Darker square represents the actual fracture and lighter evolving rectangle represents estimates based on *DEfrac*. Stages are as follows: a) 1 generation, b) 10 generations, c) 20 generations, and d) 60 generations.

Example 2

Table 3.5 gives the trace data obtained from the sampling window used for input into *DEfrac*. The results from Example 2 are given in Table 3.6 and Figure 3.13. The results of the tests are similar with a little more variation than Example 1. Test 1 was the best overall estimate. Averaging the two mean trace estimators gave better results for both size and shape. Figure 3.13 shows the evolving mean fracture within the *DEfrac* process related to the actually fracture size of the population at different generations. Figure 3.13 also visually demonstrates how well *DEfrac* has done after 60 generations.

In this case, the fit between the predicted size and shape and the actual size and shape is very good.

Table 3.5: Data obtained from sampling windows used as input into the DEfrac software for Example 2.

Trace Data	Units	Window 1	Window 2	Window 3
# Traces	-	81	36	74
Plane Dip	°	90	0	90
Plane Dip Direction	°	0	0	90
$\tilde{\mu}_i$ (point)	m	13.60	9.32	10.50
$\tilde{\mu}_i$ (stereo)	m	11.20	8.39	8.12
$\tilde{\psi}$	rise/run	0.0362	0.0435	0.0440

Table 3.6: Results of Example 2 (6 tests).

		Test					
		1	2	3	4	5	6
Input	<i>A</i>	0.5	0.9	0.1	0.5	0.5	0.5
	<i>B</i>	0.5	0.1	0.9	0.5	0.5	0.5
	w_1	0.33	0.33	0.33	0.33	0.33	0.42
	w_2	0.33	0.33	0.33	0.33	0.33	0.19
	w_3	0.33	0.33	0.33	0.33	0.33	0.39
	$\tilde{\mu}_i$	avg.	avg.	avg.	point	stereo	avg.
Output	<i>a, m</i>	21.35	24.30	17.17	18.21	22.79	23.38
	<i>b, m</i>	10.09	9.88	13.42	12.77	8.99	9.63
	Aspect ratio	2.12	2.46	1.28	1.43	2.53	2.43
	Elongation Trend, °	60.4	64.3	64.6	64.3	59	57.1
	Elongation Plunge, °	25.6	24.4	24.3	24.4	25.9	26.4

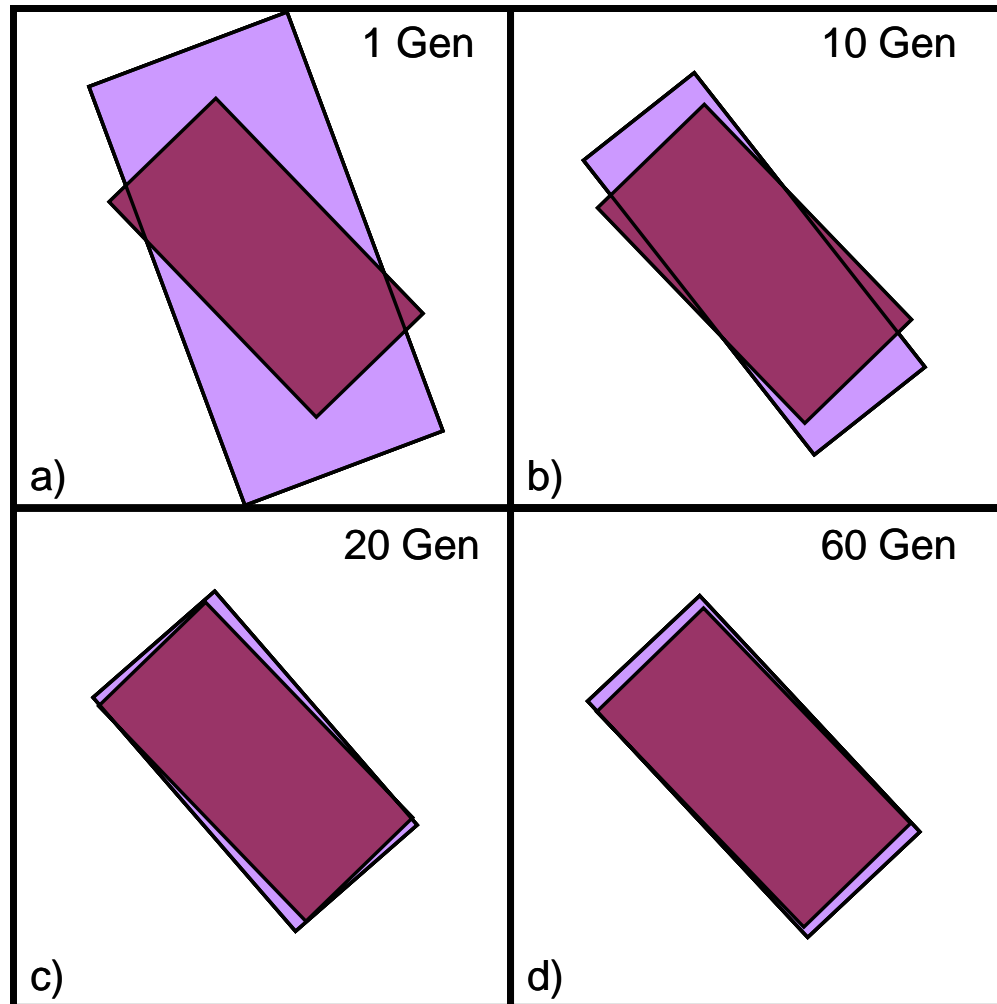


Figure 3.13: Evolving estimate of fracture size and shape for Example 2. Darker rectangle represents the actual fracture and lighter evolving rectangle represents estimates based on *DEfrac*. Stages are as follows: a) 1 generation, b) 10 generations, c) 20 generations, and d) 60 generations.

Example 3

Table 3.7 gives the trace data obtained from the sampling window used for input into *DEfrac*. The results from Example 3 are given in Table 3.8 and Figure 3.14. The results of the tests were more varied than Examples 1 & 2, with respect to the length, a . The variation is likely due to the length of the fractures being longer than the sampling window. Different values of the weighting factors, A & B , affected results more for Example 3 than Example 1 & 2. Tests 1 & 6 yielded the best results. Figure 3.14 shows the evolving mean fracture within the *DEfrac* process related to the actual fracture size of the population at different generations. Figure 3.14 also visually demonstrates how well

DEfrac has done after 60 generations. Again, as with Example 2, the fracture after 60 generations is very close to the original fracture shape and size.

Table 3.7: Data obtained from sampling windows used as input into the *DEfrac* software for Example 3.

Trace Data	Units	Window 1	Window 2	Window 3
# Traces	-	49	41	72
Plane Dip	°	90	0	90
Plane Dip Direction	°	0	0	90
$\tilde{\mu}_i$ (point)	m	19.00	8.90	11.60
$\tilde{\mu}_i$ (stereo)	m	15.09	11.44	9.97
$\tilde{\psi}$	rise/run	0.0163	0.0187	0.0247

Table 3.8: Results of Example 3 (6 tests).

		Test					
		1	2	3	4	5	6
Input	<i>A</i>	0.5	0.9	0.1	0.5	0.5	0.5
	<i>B</i>	0.5	0.1	0.9	0.5	0.5	0.5
	w_1	0.33	0.33	0.33	0.33	0.33	0.30
	w_2	0.33	0.33	0.33	0.33	0.33	0.25
	w_3	0.33	0.33	0.33	0.33	0.33	0.45
	$\tilde{\mu}_i$	avg.	avg.	avg.	point	stereo	avg.
Output	<i>a, m</i>	52.24	73.18	63.93	56.91	52.69	52.33
	<i>b, m</i>	9.86	9.58	12.99	10.44	9.51	9.84
	Aspect ratio	5.30	7.64	4.92	5.45	5.54	5.32
	Elongation Trend, °	61.7	63.2	52.0	58.4	61.5	62
	Elongation Plunge, °	25.2	24.7	27.6	26.1	25.2	25.1

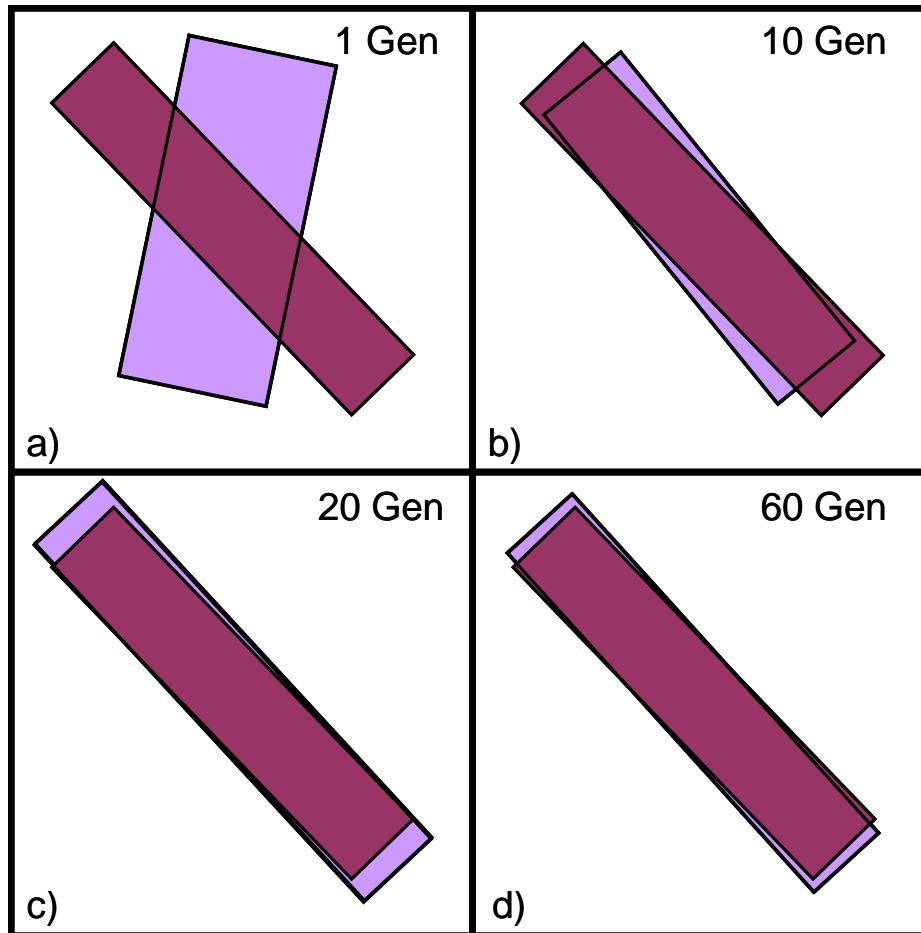


Figure 3.14: Evolving estimate of fracture size and shape for Example 3. Darker rectangle represents the actual fracture and lighter evolving rectangle represents estimates based on *DEfrac*. Stages are as follows: a) 1 generation, b) 10 generations, c) 20 generations, and d) 60 generations.

3.4.2 Example 4

Example 4 had a fracture population that did not follow the basic assumption of constant orientation (See Table 3.2). The input parameters that were obtained from the sampling window for Example 4 are shown in Tables 3.9. Due to more scatter in the empirical CDF, an upper bound point p'_1 and a lower bound point p'_1 were estimated giving a range of initial slopes $\tilde{\psi}$. This range of slopes $\tilde{\psi}$ was used in *DEfrac*. *DEfrac* was run 1,000 times and for each individual run, the slopes $\tilde{\psi}$ for each plane were chosen randomly from the given range. The results of Example 4 are given in Table 3.11.

Table 3.9: Data obtained from sampling windows used as input into the *DEfrac* software for Example 4.

Trace Data	Units	Window 1	Window 2	Window 3
# Traces	-	61	36	67
Plane Dip	°	90	0	90
Plane Dip Direction	°	0	0	90
$\tilde{\mu}_i$ (point)	m	13.00	9.44	7.61
$\tilde{\mu}_i$ (stereo)	m	12.85	12.01	9.99
$\tilde{\psi}$ (range)	rise/run	0.014 to 0.026	0.018 to 0.046	0.035 to 0.060

Table 3.10: Results of Example 4.

Output	Units	Example 4	
		Mean	Standard Deviation
<i>a</i>	m	28.1	10.2
<i>b</i>	m	9.5	0.9
Aspect ratio	-	3.1	1.4
Elongation Trend	°	73.9	19.4
Elongation Plunge	°	20.1	-

Figure 3.15 shows the estimated size and shape of the mean fracture for Example 4. The estimated mean fracture is shown with respect to the actual mean fracture of the fracture population. As seen in Figure 3.15, the estimation of size and shape loses accuracy as compared to Examples 1 thru 3, but is still a fairly reasonable estimate. The variation in the slope values used for each run is reflected by the variation in the results.

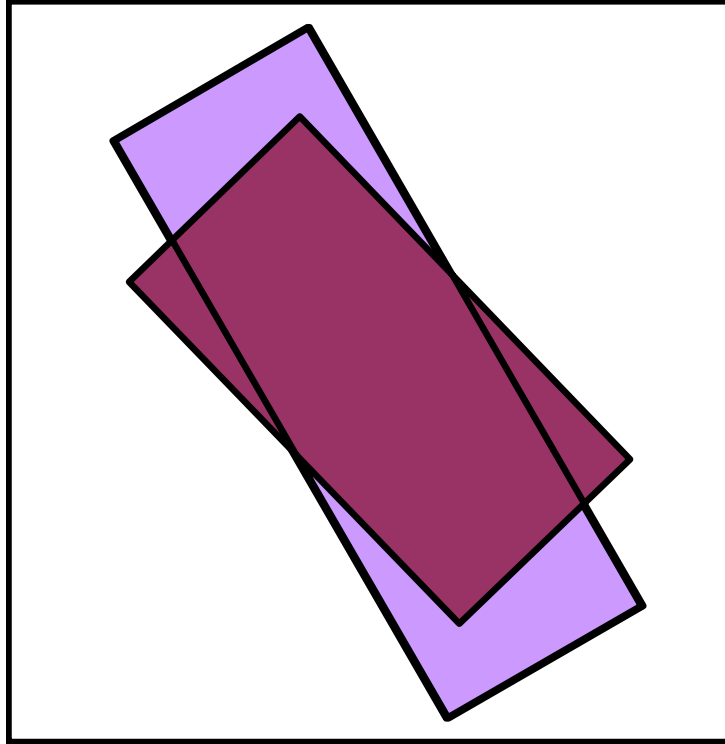


Figure 3.15: Estimate of fracture size and shape for Example 4. Darker rectangle represents the actual mean fracture and lighter rectangle represents estimates based on *DEfrac*.

3.5 *Field Example*

Figure 3.16 is a photograph taken within an abandoned railroad tunnel, which will be referred to as the *Riverbend Tunnel*, in Giles County Virginia. The rock encountered in the tunnel is a Cambrian aged dolomite (Bartholomew et al., 2000; Schultz et al., 1986). The rock structure consists of three fracture sets, comprising two near-vertical cross joints (sets 1 & 2) and bedding planes (set 3). Note that the terms fracture and fracture set are used here to denote planar or sub-planar weaknesses in the rock mass, regardless of their origin.



Figure 3.16: Photograph within Riverbend Tunnel.

Digital images were taken within the rectangular tunnel on the right wall and the roof and on a rock outcrop outside the tunnel near the north portal. Using these images, three circular trace maps (Figure 3.17) were created showing a sub-vertical joint set (fracture set 1) and bedding planes (set 3). Trace data for set 1 were then obtained from these circular trace maps. The mean orientation for set 1 was determined using the measured orientations, shown plotted on an equal area lower hemisphere projection (Lisle and Leyshon, 2004) in Figure 3.18, along with the Terzaghi correction factor (R. Terzaghi, 1965) to account for orientation biases. Figure 3.20 shows the CDF's created using the *K-M-trace* procedure (Decker and Mauldon, 2006) and the determination of the initial slopes for each surface. All the trace data obtained along with the mean orientation for set 1 used in the analysis and other input parameters, are given in Table 3.11. The trace data was entered into *DEfrac* and then *DEfrac* was run 1,000 times. *DEfrac* was run two different times as will be explained below. The results from these runs were analyzed and means for estimated fracture size and shape for set 1 were determined along with standard deviations. Table 3.12 contains the estimates of mean fracture size and shape obtained from *DEfrac*.

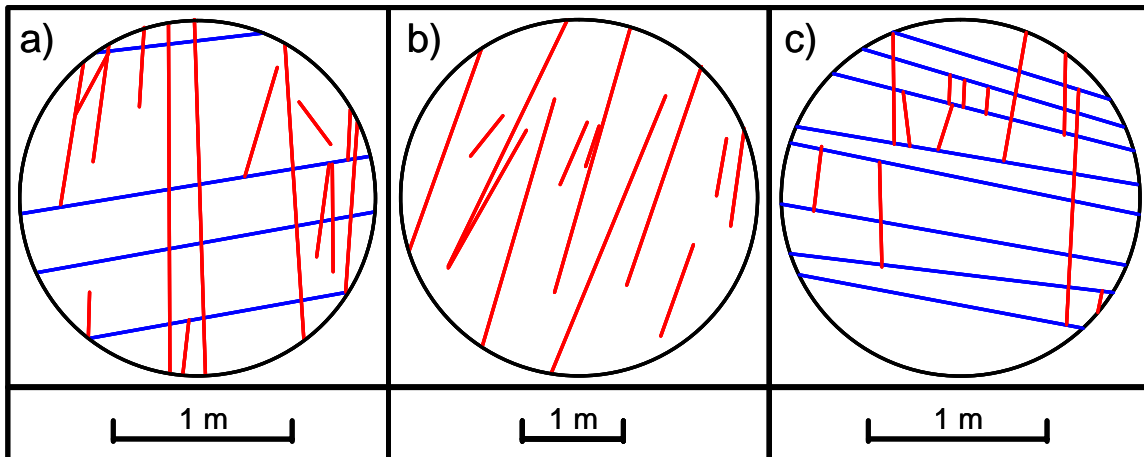


Figure 3.17: Trace maps of (a) right (west) wall in tunnel with set 1 (red) sub-vertical and set 3/bedding (blue) sub-horizontal, (b) roof in tunnel with only set 1 (red) and (c) rock face near north portal of tunnel with set 1 (red) sub-vertical and set 3/bedding (blue) sub-horizontal. Note termination of set 1 fractures on bedding planes.

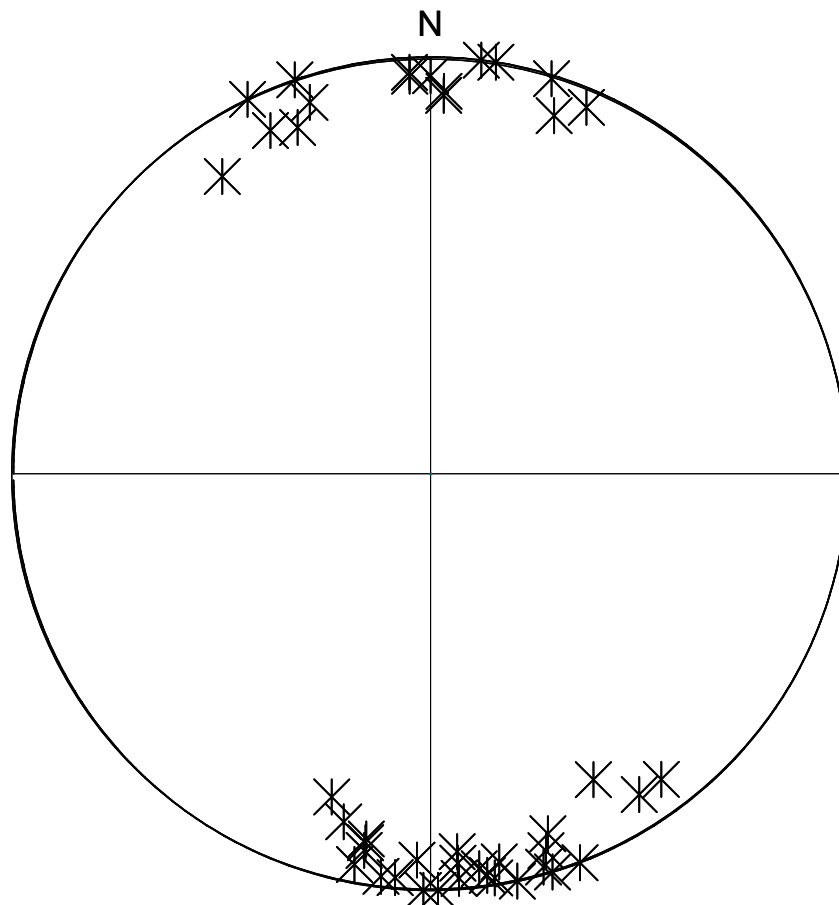


Figure 3.18: Equal area lower hemisphere projection of poles for set 1.

Discussion on calculating initial slope of empirical CDF from field data

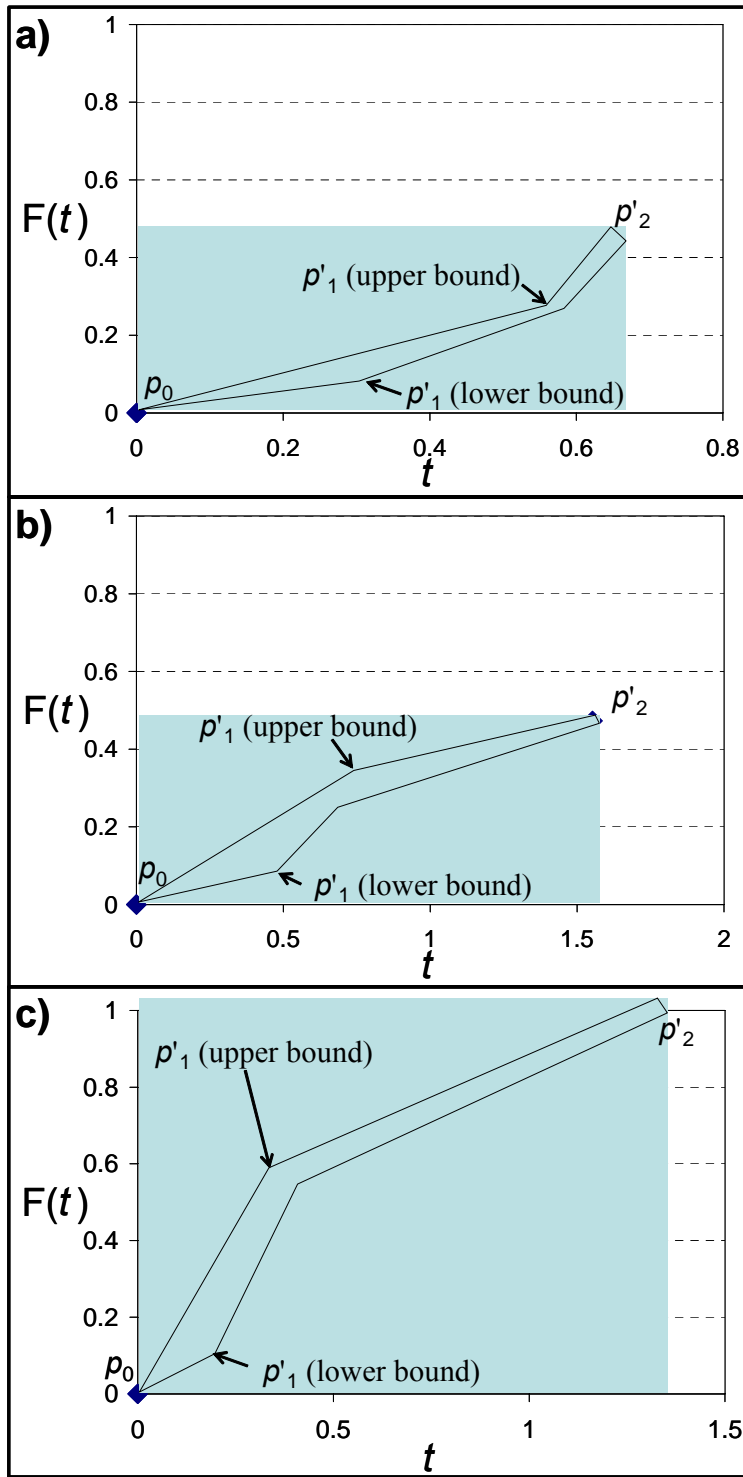


Figure 3.19: Empirical trace length CDF's for (a) right (west) wall, (b) roof, and (c) portal calculated using K-M-trace. A lower bound and upper bound p'_1 are estimated given a range of initial slopes.

There is a considerable amount of scatter in the initial portions of the empirical CDF's constructed from field data. Therefore, a lower and an upper bound point p'_1 were estimated (Figure 3.19). These two points p'_1 define a lower and an upper bound initial slope $\tilde{\psi}$. The lower and upper bound slopes $\tilde{\psi}$ define a range of possible slopes $\tilde{\psi}$. This range of slopes $\tilde{\psi}$ was used in the first *DEfrac* run. For each individual run the slopes $\tilde{\psi}$ for each plane were chosen randomly from the given range. The second *DEfrac* run was conducted using the mean slope $\tilde{\psi}$ in the range of slopes $\tilde{\psi}$.

Results of DEfrac Analyses Utilizing Field Data

Table 3.11: Trace data obtained from analyses of trace maps created from digital images in Riverbend Tunnel and mean orientation used as input into the *DEfrac* software for the field example.

Trace Data	Units	Right Wall	Roof	Portal
# Traces	-	15	13	12
Plane Dip	°	90	0	90
Plane Dip Direction	°	94	0	235
$\tilde{\mu}_i$ (point)	m	1.37	1.22	0.31
$\tilde{\mu}_i$ (stereo)	m	1.59	3.85	0.61
$\tilde{\psi}$ (range)	rise/run	0.3 to 0.5	0.2 to 0.5	0.6 to 1.7
$\tilde{\psi}$ (mean)	rise/run	0.4	0.35	1.15
Dip	°	87°		
Dip Direction	°	355°		
<i>A & B</i>	-	0.5		
w_i	-	0.333		
<i>F</i>	-	0.5		
<i>CR</i>	-	1		
# Generations	-	100		

Table 3.12: Results of field example in tunnel within Riverbend Tunnel.

Output	Units	Analysis 1		Analysis 2	
		Mean	Standard Deviation	Mean	Standard Deviation
<i>a</i>	m	2.67	0.66	2.62	0.42
<i>b</i>	m	0.56	0.07	0.60	0.05
Aspect ratio	-	4.91	1.50	4.38	0.87
Elongation Trend	°	84.4	26.4	92.2	23.0
Elongation Plunge	°	0.6	-	-7.2	-

The *DEfrac* analyses of set 1 indicates (Table 3.12) that the fractures are likely strike elongated with the fractures tending to be long and slender. This assessment is reasonable since fractures in sedimentary rocks tend to be strike elongated (Priest, 1993) and the fractures in set 1 are also mostly contained within bedding. Both analyses gave similar results with Analysis 2 resulting in slightly lower standard deviations. The results of these analyses show that the solution is not overly sensitive to changes in slope $\tilde{\psi}$.

3.6 Conclusions

- A Differential Evolution algorithm for estimating fracture size and shape from trace data has been developed. Fitness is measured via a cost function based on estimated mean trace length, and empirical CDF created using the *K-M-trace* procedure. The trace data must be obtained on two or more non-parallel planes.
- *K-M-trace* procedure has been developed to obtain a partial nearly unbiased empirical trace length CDF utilizing the Kaplan-Meier procedure developed for censored data.
- The Differential Evolution algorithm is a simple and effective optimization tool that can be used affectively with the cost function to find best fit individuals.
- The implementation of the Differential Evolution algorithm into an Excel spreadsheet, *DEfrac*, creates an efficient tool for engineers and geologist to use for inferring fracture size and shape from trace data. The Excel spreadsheet,

DEfrac, can cycle through 100 generations in less than 20 seconds on a typical desktop computer.

- The estimation of the fracture size and shape is only as good as the original estimates of $\tilde{\mu}_i$ and $\tilde{\psi}$.
- Two mean trace length estimators were utilized. Averaging the two mean trace length estimator typically improves the overall estimate of fracture size and shape.
- The overall method can give reasonable results for fracture populations that violate the assumption of constant orientation.
- The method can be easily applied in the field and gave reasonable results in this study.
- Although the initial slope $\tilde{\psi}$ is subject to judgment when using an empirical CDF derived from field data, the *DEfrac* solution is not overly sensitive to slope $\tilde{\psi}$ changes and a range of slopes $\tilde{\psi}$ covering all possibilities should be chosen.

3.7 Recommended Further Work

The procedure developed in this paper has been shown to be effective at estimating fracture size and shape when the population of fractures are rectangular and had a constant fracture size distribution. However, when fracture populations no longer have a constant fracture size or are no longer rectangular the method does not work as well, especially for mean fracture size estimation. Three examples (Example 5, 6, & 7) are given below to show how the current *DEfrac* method works for negative exponential distribution and elliptical fractures and to demonstrate the need for further research in this area. Table 3.13 gives the parameters used to create the simulated fractures. Examples 5 & 7 had a greater probability of large fractures and were generated using a $300 \times 300 \times 300 \text{m}^3$ generation region to minimize the probability of end affects. Tables 3.14, 3.15, and 3.16 give the input data that was used in *DEfrac* for Example 5, 6, & 7, respectively. This data was obtained in the same manner as Examples 1-4. A range of estimate initial slopes was obtained for Example 5 and used with multiple *DEfrac* run (1000 runs). Table 3.17 gives the results of the *DEfrac* analyses. It can be seen that the analyses overestimated the fracture size; however, the elongation direction was predicted

fairly accurate in all cases (Figure 3.20). Example 5 and 6 were better than Example 7, which violated the most assumptions.

It should be noted that Example 5 & 7 had a negative exponential distribution for fracture size. The trace data for these examples was likely affected by a sampling bias that is introduced when the fracture size is distributed shown by the higher estimated mean trace length for these examples (Tables 3.14 & 3.15). This sampling bias occurs because the larger a fracture is the greater the probability that the maximum trace length will be sampled (see Eq. 3.11). This bias tends to create higher estimates of mean trace length $\tilde{\mu}_t$ than the theoretical mean trace length μ_t of a fracture population.

Despite sampling biases and the violation of basic assumptions the *DEfrac* method was still able to estimate the elongation direction. This is likely due to the relative magnitude of the mean trace length and the initial CDF slope between the planes.

Further research is needed to enhance the *DEfrac* method to handle any fracture size distribution without the need to assume an underlying distribution. Also further research is needed to look at the affect of assuming different shapes (circular, elliptical, etc.) and what assumption and parameters give the best results for different shaped fractures.

Table 3.13: Varied fracture set parameters for Examples 5, 6, & 7.

Example Number	Length, a (m)	Aspect Ratio	Shape	Size Distribution	Orientation Distribution
5	20	2	Rectangular	Neg. Exponential	Constant
6	20	2	Elliptical	Constant	Constant
7	20	2	Elliptical	Neg. Exponential	Fisher ($\kappa=30$)

Table 3.14: Data obtained from sampling windows used as input into the *DEfrac* software for Example 5.

Trace Data	Units	Window 1	Window 2	Window 3
# Traces	-	54	46	84
Plane Dip	°	90	0	90
Plane Dip Direction	°	0	0	90
$\tilde{\mu}_i$ (point)	m	28.00	11.80	16.90
$\tilde{\mu}_i$ (stereo)	m	24.30	14.08	17.02
$\tilde{\psi}$ (range)	rise/run	0.014 to 0.040	0.018 to 0.037	0.020 to 0.040

Table 3.15: Data obtained from sampling windows used as input into the *DEfrac* software for Example 6.

Trace Data	Units	Window 1	Window 2	Window 3
# Traces	-	41	28	47
Plane Dip	°	90	0	90
Plane Dip Direction	°	0	0	90
$\tilde{\mu}_i$ (point)	m	8.42	8.58	7.26
$\tilde{\mu}_i$ (stereo)	m	12.99	8.75	9.71
$\tilde{\psi}$	rise/run	0.0273	0.0386	0.0364

Table 3.16: Data obtained from sampling windows used as input into the *DEfrac* software for Example 7.

Trace Data	Units	Window 1	Window 2	Window 3
# Traces	-	36	22	50
Plane Dip	°	90	0	90
Plane Dip Direction	°	0	0	90
$\tilde{\mu}_i$ (point)	m	25.7	18.2	18.40
$\tilde{\mu}_i$ (stereo)	m	25.13	14.48	29.26
$\tilde{\psi}$	rise/run	0.0190	0.0211	0.0257

Table 3.17: Results of Examples 5, 6, & 7.

Output	Units	Example 5		Example 6	Example 7
		Mean	Standard Deviation		
<i>a</i>	m	30.6	9.7	34.24	34.44
<i>b</i>	m	17.5	2.1	7.96	28.30
Aspect ratio	-	1.8	0.7	4.30	1.22
Elongation Trend	°	57.4	41.4	56.2	63.2
Elongation Plunge	°	23.7	-	26.7	24.7

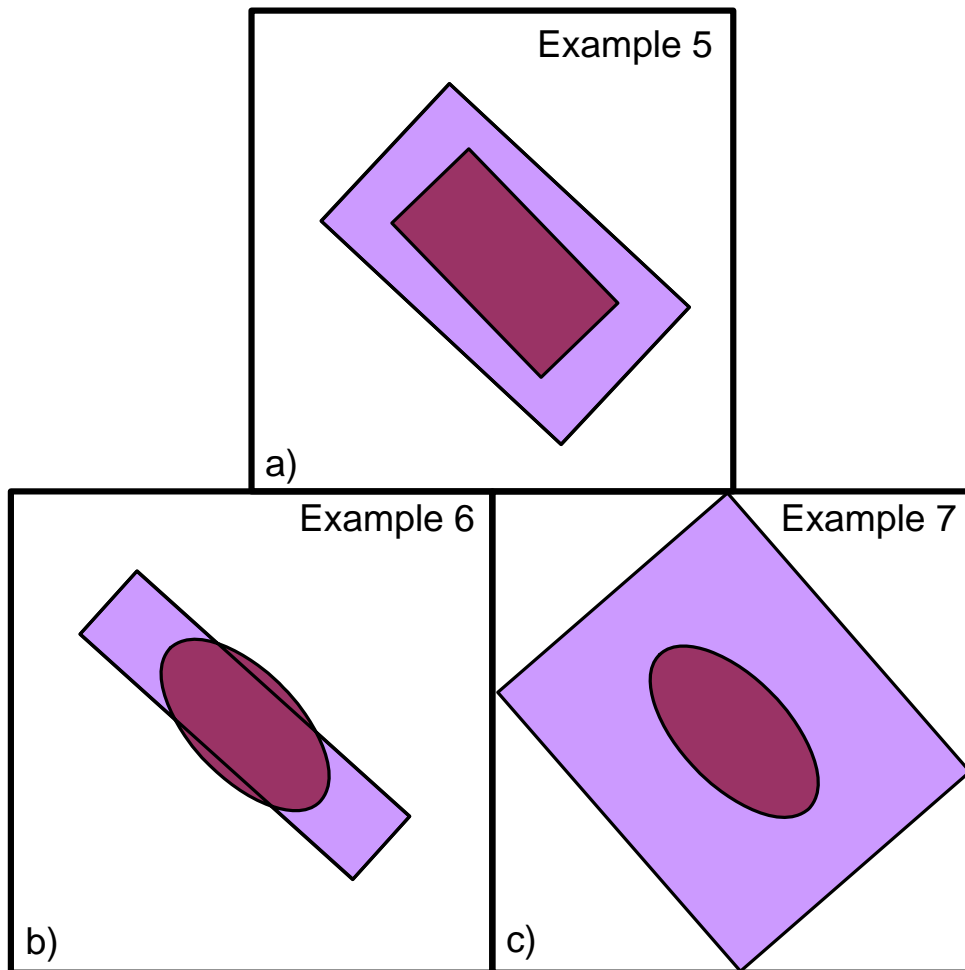


Figure 3.20: Estimates of fracture size and shape for Example 5, 6, & 7. Darker rectangle or ellipse represents the actual mean fracture and lighter rectangle represents estimates based on *DEfrac*, a) Example 5, b) Example 6, and c) Example 7.

3.8 Symbols Used

Symbol	Meaning	Dimension
t	trace length	[L]
t_{max}	maximum trace length that a rectangular fracture can produce	[L]
μ_t	theoretical mean trace length	[L]
$\tilde{\mu}_t$	estimated mean trace length	[L]
μ'_t	apparent mean trace length	[L]
w	width of sampling window	[L]
l	length of sampling window	[L]
θ	angle between side parallel to sampling window width and trace	[deg]
n	total # of intersections between the traces and the sampling window border	[-]
m	total # of trace endpoints within the sampling window	[-]
a	long side of rectangular fracture (along elongation)	[L]
b	short side of rectangular fracture	[L]
β	angle between intersection vector (trace) and side b	[deg]
u_i	i^{th} length interval boundary ($K-M$ -trace)	[L]
r_i	# removals – censored traces ($K-M$ -trace) in i^{th} length interval	[-]
d_i	# terminations – uncensored traces ($K-M$ -trace) in i^{th} length interval	[-]
n_i	# of total traces observed at length u_i ($K-M$ -trace)	[-]
n'_i	# of traces that have not terminated at length u_i ($K-M$ -trace)	[-]
\tilde{P}_i	survival probability at each u_i ($K-M$ -trace)	[-]
\tilde{P}'_i	termination probability at each u_i ($K-M$ -trace)	[-]
ψ	probability of any t less than t_{max} or theoretical slope of trace length CDF for rectangular fractures with constant size and orientation	[-]
$\tilde{\psi}$	empirical slope of CDF obtained from trace data	[-]
p_0	points defining the origin for both the theoretical and empirical CDF	[-]
p_i	points defining theoretical CDF	[-]
p'_i	points defining empirical CDF	[-]

Symbol	Meaning	Dimension
A	weighting factor for mean trace length	[-]
B	weighting factor for slope of CDF	[-]
w_i	Weighting factor for i^{th} sampling plane	[-]
C	Cost (a function of a , b , & β)	[-]
NP	# of individuals in DE algorithm	[-]
X_i	i th individual in <i>Target Vector</i> DE algorithm	[L, L, °]
X_i^m	i th mutated individual DE algorithm	[L, L, °]
X'_i	i th individual in <i>Trial Vector</i> DE algorithm	[L, L, °]
F	scaling factor for mutation in DE Algorithm	[-]
CR	constant controlling crossover rate	[-]
$randnum$	random number generated in DE algorithm controlling crossover operation	[-]
$randint$	random integer generated in DE algorithm controlling crossover operation	[-]
P_{nm}	Parameter m for individual n in DE algorithm	[varies]
P_{32}	3d fracture intensity	[L ⁻¹]

3.9 Acknowledgements

The study presented in this paper is based upon work that is supported by the National Science Foundation under grant number CMS 0324889. Any opinions, findings and conclusions or recommendations expressed in this paper are those of the authors and do not necessarily reflect the views of the National Science Foundation.

Appendix 3.A: DEfrac User Documentation

DEfrac User Documentation

Created by: Jeremy Decker
Virginia Tech
Department of Civil and
Environmental Engineering
jbdecker@vt.edu



Software Use:

DEfrac was developed at Virginia Tech as part of the AMADEUS research project, which is funded by the National Science Foundation, for educational and research purposes. The spreadsheet implements the Differential Evolution optimization algorithm (Price and Storn, 1997; Price et al., 2005; Storn and Price, 1997) to infer fracture size and elongation direction from trace data on three nonparallel sampling planes.

Setup:

The spreadsheet application consists of the folder “DEfrac” which contains two Excel workbooks:

- DEfrac07.xls
- DEfracData.xls

For the application to function properly copy the DEfrac folder directly onto the C drive, so that the file path to the Excel files are as follows: C:\DEfrac\...

Open file DEfrac07.xls to start the application.

Worksheets:

The application contains four main worksheets:

- DEfrac User Documentation
- Input
- DE
- Random Crossover

DEfrac User Documentation

The first sheet contains user documentation

Input

This worksheet is the user interface for the *DEfrac* application. There are two input tables in the user interface. All input variables that can be user defined are in red text. The Algorithm Input table allows the user to change parameters that affect the algorithm behavior, generation number, and run number. The following inputs are in this table:

F	Constant that controls the magnitude of mutation (typical value 0.4 to 1.0)
CR	Cross over rate defined from 0 to 1 with 1 being 100% crossover probability
# Generations	Specifies the number of generations that the algorithm will go through in one <i>DEfrac</i> run.
# Runs	Specifies the number of runs that the algorithm will go through before stopping

The next table is the Trace Data input table. The following inputs are in this table:

For each Plane	
Plane Dip	Constant that control the magnitude of mutation (typical value 0.4 to 1.0)
Plane Dip Direction	Cross over rate defined from 0 to 1 with 1 being 100% crossover probability
$\tilde{\mu}_i$ (point)	Estimated mean trace length using the endpoint estimator (Mauldon, 1998)
$\tilde{\mu}_i$ (stereo)	Estimated mean trace length using the stereological estimator (Decker and Mauldon, 2006)
$\tilde{\mu}_i$ type	Specifies whether the algorithm should use the endpoint estimator (enter 1), the stereological estimator (enter 2), the mean of the two estimators (enter 3), or no data (enter 4)
$\tilde{\psi}$ (single value)	Estimated initial slope of empirical trace length CDF (using <i>K-M-trace</i> (Decker and Mauldon, 2006)) *This input is to be used when only a single value has been computed.
$\tilde{\psi}$ (range) Low	Estimated initial slope of empirical trace length CDF (using <i>K-M-trace</i>) *User should input lower bound value when a range of slopes is being used.
$\tilde{\psi}$ (range) High	Estimated initial slope of empirical trace length CDF (using <i>K-M-trace</i>) *User should input upper bound value when a range of slopes is being used.

$\tilde{\psi}$ type	Specifies whether the algorithm should use a single value (enter 1), a range (enter 2), or no data (enter 3) *Note that if the range option is used the algorithm will randomly choose an initial slope that lies between the upper and lower bound for each run.
Fracture Orientation	
Dip	The mean dip of the fracture set being analyzed
Dip Direction	The mean dip direction of the fracture set being analyzed
Weighting Factors for cost function: $C(Frac) = \sum_{i=1}^k w_i \left[A \frac{ \mu_{ii} - \tilde{\mu}_{ii} }{\tilde{\mu}_{ii}} + B \frac{ \psi_i - \tilde{\psi}_i }{\tilde{\psi}_i} \right]$	
A	Weight factor for mean trace length $\tilde{\mu}_i$, note A + B = 1
B	Weight factor for initial slope of empirical CDF $\tilde{\psi}$, note A + B = 1
w_i	Weight factor for each sampling plane, note $\sum_{i=1}^k w_i = 1$

The worksheet contains three macros that run by clicking on the corresponding macro button. The macros perform the following tasks:

First Generation	Initializes process and loops through first generation
Single Run	Loops through the number of generations defined by user *This macro does not initialize process, therefore, it can be used to accumulate generations (e.g. run “First Generation” to initialize then run “Single Run” for 10 generations, then run “Single Run” again for another 10 generation which would make a total of 20 generation). This option allows users to track the progress of the convergence. **Remember for each new run using “Single Run” the “First Generation” macro should be ran first.
Multiple Runs	Runs first two macros “First Generation” and “Single Run” and then copies output to Workbook DEfracData.xls – this process loops number of runs specified by user. *DEfracData.xls should not be open the macro will open the workbook. If the workbook is already open the macro will not work. DEfracData.xls will contain output data for all runs, it should be saved under a new name. This option allows users to automatically run multiple runs for statistical analyses.

An output table is displayed on the Input worksheet and contains the following output parameters:

Cost Mean	Mean cost (value of cost function) of 30 individuals in Differential Evolution algorithm after specified number of generations
Cost Variation	Coefficient of variation of cost (value of cost function) for 30 individuals in Differential Evolution algorithm after specified number of generations
<i>a</i> (mean)	Mean <i>a</i> (Figure 1) of 30 individuals in Differential Evolution algorithm after specified number of generations*
<i>b</i> (mean)	Mean <i>b</i> (Figure 1) for 30 individuals in Differential Evolution algorithm after specified number of generations*
Equivalent Radius (mean)	Mean equivalent radius, equivalent radius = $\sqrt{\frac{ab}{\pi}}$ *
Aspect Ratio (mean)	Mean aspect ratio, aspect ratio = $\frac{a}{b}$
Elongation Trend (mean)	Mean elongation trend or dip direction, elongation parallel to side <i>a</i> (Figure 1), units in degrees
Elongation Plunge (mean)	Mean elongation plunge or dip, elongation parallel to side <i>a</i> (Figure 1), units in degrees
# Generations	Number of generations since algorithm was initialized
*Unit of length equivalent to unit of mean trace length defined by user	

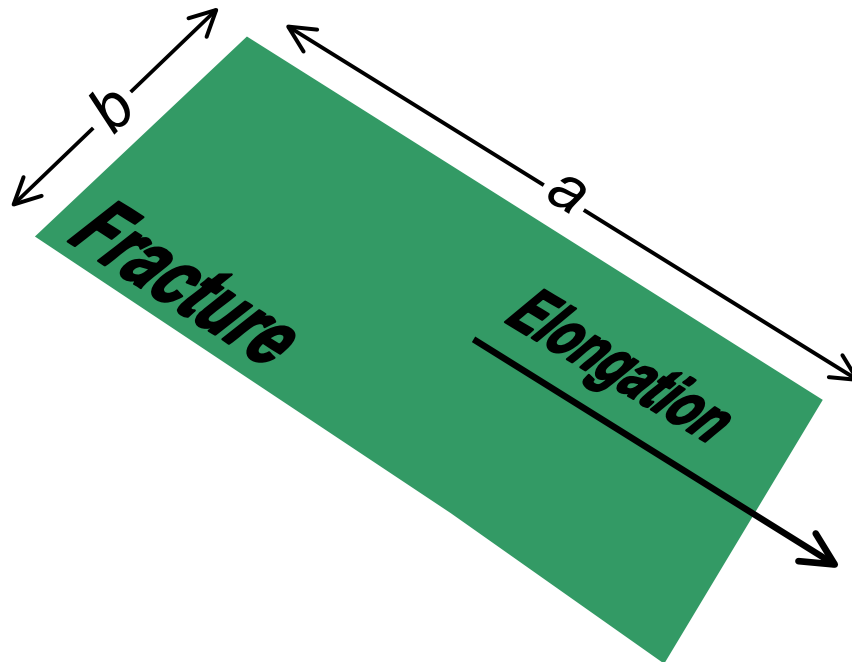


Figure 3.A1: Assumed fracture geometry for *DEfrac* analysis.

DE

The DE worksheet contains the Differential Evolution algorithm. When the macros are run, Excel will switch to this worksheet. Counters of number of generations and number of runs are on this sheet so that the user can track the progress as the application is running. This work sheet is completely protected and does not need to be manipulated in any way by the user. The macros turn protection on and off, therefore, if protection has been turned of by user for any reason it must be turned back on or an error will occur when a macro is run.

Random Mutation

The Random Mutation sheet contains an algorithm that allows three separate individuals to be randomly chosen for the mutation scheme in the Differential Evolution algorithm. This work sheet is completely protected and does not need to be manipulated in any way by the user.

Appendix 3.B: K-M-trace User Documentation

K-M-trace User Documentation

Created by: Jeremy Decker
Virginia Tech
Department of Civil and
Environmental Engineering
jbdecker@vt.edu



Software Use:

K-M-trace was developed at Virginia Tech as part of the AMADEUS research project, which is funded by the National Science Foundation, for educational and research purposes. The spreadsheet implements the Kaplan-Meier (Kaplan and Meier, 1958) procedure modified for trace data (Decker and Mauldon, 2006) to compute unbiased portions of empirical trace length CDF's.

Setup:

The spreadsheet application consists of an Excel workbook:

- K-M-trace.xls

Open excel file to start the application.

Worksheets:

The application contains four main worksheets:

- K-M-Trace User Documentation
- Input
- TraceLengthCDF
- K-M

K-M-Trace User Documentation

The first sheet contains user documentation

Input

This worksheet is the user interface for the *K-M-trace* application. The user interface consists of 7 columns, with only two being input columns (light green shading and red font), and three macro buttons. The columns are as follows:

Trace #	# index for input traces
Length	Length of traces, input by user *any unit of length may be used as long as it is consistent between traces **if data is being copied from other spreadsheet paste values only
Censored	Enter 1 if trace is censored (removals—at least one end of trace not contained in sampling window), enter 0 if trace is uncensored (terminations—both ends of trace in sampling window) **if data is being copied from other spreadsheet paste values only
Terminations	Counts terminations (uncensored) and indexes each uncensored trace *In order to index the terminations, this column only returns integers on the row of a termination. The rows that are not terminations are set at 0.5 plus the last termination number. This operation allows the terminations to be separated from the removals.
Removals	Counts removals (censored) and indexes each censored trace *In order to index the removals, this column only returns integers on the row of a removal. The rows that are not removals are set at 0.5 plus the last termination number. This operation allows the removals to be separated from the removals.
Total Terminations	Total Terminations *does not need to be integer (see Terminations above)
Total Removals	Total Removals *does not need to be integer (see Terminations above)
**in order to index the terminations and removals these columns only return integers on the row of a termination or removal, respectively. The rows that are not terminations or removals	

The three macros run by clicking on the corresponding macro buttons. The macros perform the following tasks:

Plot CDF	Computes CDF, plots the CDF, and then takes user to worksheet “TraceLengthCDF” which show plotted CDF
Clear CDF	Clears CDF *This macro clears only one CDF, so if more than one has been plotted this macro will need to be run more than once.
Clear Input	Clears the two user input columns (light green shading)

TraceLengthCDF

The TraceLengthCDF worksheet is the CDF plot (Figure 1). This work sheet is completely protected. The macros turn protection on and off, therefore, if protection has been turned of by user for any reason it must be turned back on or an error will occur when a macro is run.

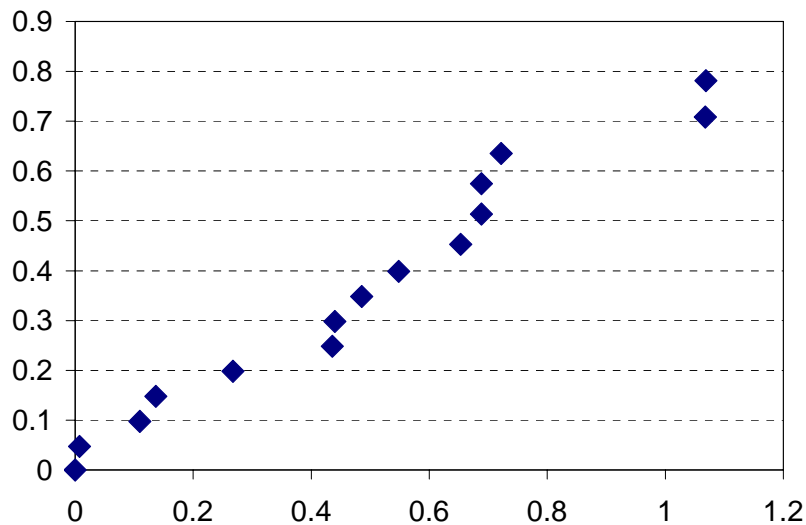


Figure 3.B1: Partial empirical trace length CDF.

K-M

The K-M sheet contains the *K-M-trace* algorithm (decker ref) that computes the empirical CDF. This work sheet is completely protected and does not need to be manipulated in any way by the user. The macros turn protection on and off, therefore, if protection has been turned of by user for any reason it must be turned back on or an error will occur when a macro is run.

References

- Armitage, P., Berry, G. and Matthews, J.N.S., 2002. *Statistical Methods in Medical Research*. Blackwell Science Ltd, Malden, MA.
- Babu, B.V. and Angira, R., 2003. Optimization Of Water Pumping System Using Differential Evolution Strategies, Proceedings of the Second International Conference on Computational Intelligence, Robotics, and Autonomous Systems (CIRAS-2003), Singapore.
- Baecher, G.B., 1980. Progressively Censored Sampling of Rock Joint Traces. *Mathematical Geology*, 12(1): 33-40.
- Baecher, G.B., Lanney, N.A. and Einstein, H.H., 1977. Statistical description of rock properties and sampling. In: F.D. Wang and G.B. Clark (Editors), *Proceedings of the 18th U.S. Symposium on Rock Mechanics*. Colorado School of Mines, Sante Fe, New Mexico, pp. 5C1.1-5C1.8.
- Bai, T. and Pollard, D.D., 2000. Closely spaced fractures in layered rocks: Initiation mechanism and propagation kinematics. *Journal of Structural Geology*, 22(10): 1409-1425.
- Bartholomew, M.J., Schultz, A.P., Lewis, S.E., McDowell, R.C. and Henika, W.S., 2000. Digital Geological Map of the Radford 30 by 60 Minute quadrangle, Virginia and West Virginia, Virginia Department of Mines Minerals and Energy, Division of Mineral Resources Preliminary Draft.
- Cooke, M.L. and Underwood, C.A., 2001. Fracture termination and step-over at bedding interfaces due to frictional slip and interface opening. *Journal of Structural Geology*, 23: 223-238.
- Decker, J.B. and Mauldon, M., 2006. Determining Size and Shape of Fractures from Trace Data using a Differential Evolution Algorithm. In: D.P. Yale, S.C. Holtz, C. Breeds and U. Ozbay (Editors), *Proceedings of the 41st U.S. Symposium on Rock Mechanics*, Golden, Colorado, pp. Paper No. 969.
- Decker, J.B. and Mauldon, M., 2007. Generalized Stereological Estimator for Mean Fracture Trace Length and Density. Not Yet Published.
- Einstein, H.H. and Baecher, G.B., 1983. Probabilistic and statistical methods in engineering geology, specific methods and examples, part 1: exploration. *Rock Mechanics & Rock Engineering*, 16: 39-72.
- Engelder, T. and Gross, M.R., 1993. Curving cross joints and the lithospheric stress field in eastern North America. *Geology*, 21: 817-820.
- Golder and Associates, 2004. *FracWorks XP Discrete Feature Simulator, User Documentation, Version 4.0*, Seattle, Washington.
- Gross, M.R., 1993. The origin and spacing of cross joints; examples from the Monterey formation, Santa Barbara Coastline, California. *Journal of Structural Geology*, 15(6): 737-751.

- Grossmann, N.F., 1995. About the distribution of the trace lengths of a joint set. In: C. Myer, Goodman, & Tsang (Editor), Proceedings of the Conference of Fractured and Jointed Rock Masses. Balkema, Rotterdam, Lake Tahoe, California, USA, pp. 161-169.
- Helgeson, D.E. and Aydin, A., 1991. Characteristics of joint propagation across layer interfaces in sedimentary rocks. *Journal of Structural Geology*, 13(8): 897-911.
- Holland, J.H., 1975. *Adaptation in Natural and Artificial Systems*. University of Michigan Press, Ann Arbor, Michigan.
- Ilonen, J., Kamarainen, J.-K. and Lampinen, J., 2003. Differential Evolution Training Algorithm for Feed-Forward Neural Networks. *Neural Processing Letters*, 17: 93-105.
- Kaplan, E.L. and Meier, P., 1958. Nonparametric Estimation from Incomplete Observations. *American Statistical Association Journal*, June 1958: 457-481.
- Kemeny, J. and Post, R., 2003. Estimating three-dimensional rock discontinuity orientation from digital images of fracture traces. *Computers & Geosciences*, 29: 65-77.
- Kulatilake, P.H.S.W. and Wu, T.H., 1984. Estimation of Mean Trace Length of Discontinuities. *Rock Mechanics & Rock Engineering*, 17: 215-232.
- Kulatilake, P.H.S.W. and Wu, T.H., 1986. Relation between Discontinuity Size and Trace Length, *Rock Mechanics: Key to Energy Production*, Proceedings of the 27th US Symposium on Rock Mechanics. Proceedings - Symposium on Rock Mechanics 27th. Publ by Soc of Mining Engineers of AIME, Littleton, CO, USA., Tuscaloosa, AL, USA, pp. 130-133.
- Laslett, G.M., 1982. Censoring and Edge Effects in Areal and Line Transect Sampling of Rock Joint Traces. *Mathematical Geology*, 14(2): 125-140.
- Lisle, R.J. and Leyshon, P.R., 2004. *Stereographic Projection Techniques for Geologists and Civil Engineers*. Cambridge University Press, New York.
- Mauldon, M., 1998. Estimating mean fracture trace length and density from observations in convex windows. *Rock Mechanics & Rock Engineering*, 31(4): 201-216.
- Mauldon, M., Dunne, W.M. and Rohrbaugh Jr., M.B., 2001. Circular scanlines and circular windows: new tools for characterizing the geometry of fracture traces. *Journal of Structural Geology*, 23: 247-258.
- Michalewicz, Z., 1996. *Genetic algorithms + data structures = evolution programs*. Springer-Verlag, Berlin ; New York, xiv, 250 p. pp.
- Pahl, P.J., 1981. Estimating the Mean Length of Discontinuity Traces. *International Journal of Rock Mechanics & Mining Sciences & Geomechanics Abstracts*, 18(3): 221-228.
- Price, K. and Storn, R., 1997. Differential Evolution. *Dr. Dobb's Journal*, 22(4): 18-24.

- Price, K., Storn, R.M. and Lampinen, J.A., 2005. *Differential Evolution: A Practical Approach to Global Optimization*. Natural. Springer, Berlin.
- Priest, S.D., 1993. *Discontinuity Analysis for Rock Engineering*. Chapman & Hall, New York, 473 pp.
- Priest, S.D., 2004. Determination of discontinuity size distributions from scanline data. *Rock Mechanics & Rock Engineering*, 37(5): 347-368.
- Ravindran, K., Ragsdell, K.M. and Reklaitis, G.V., 2006. *Engineering Optimization: Methods and Applications*. John Wiley & Sons, Hoboken, NJ.
- Reeves, C.R. and Rowe, J.E., 2003. *Genetic algorithms : principles and perspectives : a guide to GA theory*. Operations research/computer science interfaces series ; ORCS 20. Kluwer Academic Publishers, Boston, vii, 332 p. pp.
- Ruf, J.C., Rust, K.A. and Engelder, T., 1998. Investigating the effect of mechanical discontinuities on joint spacing. *Tectonophysics*, 295: 245-257.
- Russell, S.J. and Norvig, P., 2003. *Artificial Intelligence: A Modern Approach: Second Edition*. Prentice Hall, Upper Saddle River, New Jersey.
- Ruzek, B. and Kvasnicka, M., 2001. Differential Evolution Algorithm in the Earthquake Hypocenter Location. *Pure and Applied Geophysics*, 158: 667-693.
- Schultz, A.P., Stanley, C.B., Gathright, I., T.M., Rader, E.K., Bartholomew, M.J., Lewis, S.E. and Evans, N.H., 1986. *Geological Map of Giles County, Virginia*. Publication 69. 1: 50,000-scale colored geologic map., Commonwealth of Virginia Department of Mines, Minerals and Energy-Division of Mineral Resources.
- Schwefel, H.P., 1995. *Evolution and Optimum Seeking*. John Wiley, New York.
- Song, J.J. and Lee, C.I., 2001. Estimation of joint length distribution using window sampling. *International Journal of Rock Mechanics & Mining Sciences*, 38: 519-528.
- Storn, R., 2007. *Differential Evolution (DE)*, <http://www.icsi.berkeley.edu/~storn/code.html#appl> , Berkley, CA, Accessed 03-15-07.
- Storn, R. and Price, K., 1997. Differential Evolution - A Simple and Efficient Heuristic for Global Optimization over Continuous Spaces. *Journal of Global Optimization*, 11(4): 341-359.
- Terzaghi, R.D., 1965. Sources of errors in joint surveys. *Geotechnique*, 15(3): 287-304.
- Tonon, F. and Chen, S., 2005. Closed-form and numerical solutions for the probability distribution of discontinuity diameters. In: G. Chen, S. Huang, W. Zhou and J. Tinucci (Editors), *Proceedings of the 40th U.S. Symposium on Rock Mechanics*. ARMA, Anchorage, Alaska.

- Villaescusa, E. and Brown, E.T., 1992. Maximum likelihood estimation of joint sizes from trace length measurements. *Rock Mechanics & Rock Engineering*, 25: 67-87.
- Wang, X., Mauldon, M., Dunne, W. and Heiny, C., 2004. Using borehole data to estimate size and aspect ratio of subsurface fractures, *Proceedings of the 6h North American Rock Mechanics Symposium (NARMS)*, Houston, Texas.
- Wang, X., Mauldon, M., Dunne, W. and Heiny, C., 2005. Extracting fracture characteristics from the piercing-type intersections on borehole walls. In: G. Chen, S. Huang, W. Zhou and J. Tinucci (Editors), *Proceedings of the 40th U.S. Symposium on Rock Mechanics (USRMS)*, Anchorage, Alaska.
- Warburton, P.M., 1980a. A stereological interpretation of joint trace data. *International Journal of Rock Mechanics & Mining Sciences and Geomechanics Abstracts*, 17: 181-190.
- Warburton, P.M., 1980b. Stereological interpretation of joint trace data: influence of joint shape and implications for geological surveys. *International Journal of Rock Mechanics & Mining Sciences and Geomechanics Abstracts*, 17: 305-316.
- Zhang, L. and Einstein, H.H., 2000. Estimating the intensity of rock discontinuities. *International Journal of Rock Mechanics & Mining Sciences & Geomechanics Abstracts*, 37(5): 819-837.
- Zhang, L., Einstein, H.H. and Dershowitz, W.S., 2002. Stereological relationship between trace length and size distribution of elliptical discontinuities. *Geotechnique*, 52(6): 419-433.

This page intentionally left blank.

4 Rock Fracture Modeling, Imaging and Visualization for a Tunnel in Virginia

Abstract: A field study was performed within an abandoned tunnel in Southwest Virginia. The field study consisted of utilizing state of the art imaging equipment within the tunnel. The image data was used to obtain remote measurements of fracture data including orientation and trace statistics from trace maps created remotely. 3d visualization techniques were used to enhance the remote sampling process. A preliminary fracture model was created using data from outside of the tunnel and general observations around the site and in the tunnel. A 9 meter section of the tunnel was split into three 3 meter intervals analogous to different excavation advancements. Each interval was sampled in the field and remotely. The fracture model was updated and adjusted based on principles of forward modeling using the data obtained from each interval.

* The author acknowledges the contributions of the AMADEUS team to the last paragraph of Section 4.1, Section 4.3.2 and the last paragraph of Section 4.3.3.

4.1 Introduction

One of the greatest challenges for geological engineering is the characterization of rock masses. Geological engineers usually can make only limited observations of the rock mass. Typically, they only have small amounts of data that are obtained from different locations on site, e.g. boreholes, outcrops, excavations, etc. In the case of tunnels, however, the excavation itself provides a great opportunity for engineers and geologists to see and sample the rock mass. The difficulty is being able to obtain the data in a safe and efficient manner and then utilize the data to update and modify the tunnel design and/or the construction procedure, all without impeding the ongoing excavation. The AMADEUS research project being conducted at Virginia Tech is examining many of the above issues for tunneling applications. A field study has been performed to test and validate methods developed as part of the AMADEUS research project. The field study

consisted of using imaging techniques to record data and then using the data to update and verify fracture models for tunnel support design. A brief background on concepts pertaining to the field study will be discussed, such as the observational method, fracture modeling, forward modeling, and 3d visualization.

Observational Method

The idea of modifying the design of a project during construction, based upon new data is referred to as “the observational method.” Introduced by Karl Terzaghi (Peck, 1969; Terzaghi, 1961), “the observational method” is used today in many tunneling applications, e.g. the New Austrian Tunneling Method NATM (e.g., Kolymbas, 2005; Muller-Salzburg and Fecker, 1978), to improve safety and reduce costs (e.g., Einstein, 2004; Field et al., 2005; e.g., Haas and Einstein, 2002; Kovari and Amstad, 1993; Newman et al., 2003; Powderham, 1994; Powderham, 2002).

Fracture Models

In rock engineering, fracture models have been created based on geomechanical processes, stochastic-geometric processes, stochastic-mechanistic, or some other approach (Dershowitz, 1985; Einstein and Stephansson, 2000; La Pointe, 1993). Several such models will be briefly described and discussed. For a more extensive review on all these models and their characteristics, the reader is referred to Einstein and Stephansson (2000).

Geomechanical fracture models incorporate mechanics-based algorithms to create fractures as they would have been initiated and propagated in nature, under various boundary conditions and stress states. The mechanistic approach generally uses numerical techniques to represent boundary conditions, material behavior, and state parameters to produce fractures and fracture systems (e.g., Bai and Pollard, 2000; Cooke and Underwood, 2001; Engelder and Gross, 1993; Pollard and Segall, 1987).

Geomechanical models represent geological features such as fracture set interaction (Renshaw and Pollard, 1992) and clustering phenomena quite well; they are, however, computationally demanding (Einstein and Stephansson, 2000). Also in many cases the lack of sufficient data on forces, material behavior, and initial states prevents geomechanical processes from accurately modeling fracture systems (Hoffmann et al., 2004).

Stochastic-geometric fracture models generate fracture systems based on a probabilistic approach. Such models can adequately model most fracture characteristics; however they must be coupled with experience and verification (e.g., Baecher, 1982; Einstein, 1991). These models require less computation and time, but, may not adequately model fracture set interaction and clustering or account for the origin of the fracture system (e.g., Einstein and Stephansson, 2000; Hoffmann et al., 2004; Renshaw and Pollard, 1992). Despite these potential limitations, the stochastic-geometric approach is widely used (e.g., Baecher et al., 1977; Deng et al., 1995; Dershowitz and Einstein, 1988; Gilmour et al., 1986; Hudson and La Pointe, 1980; Kulatilake et al., 2003; La Pointe and Hudson, 1985; Long et al., 1991; Ouenes, 2000; Priest and Samaniego, 1983; Snow, 1969).

Several approaches combine mechanistic and stochastic elements, blending together the strengths while trying to eliminate the weakness of other models (e.g., Hoffmann et al., 2004). Some of these models deal effectively with fracture set interactions such as cross joints in sedimentary rock by using hierarchical processes (e.g., Dershowitz, 1979; Einstein et al., 1990; Einstein and Lee, 1992; Gervais et al., 1992; Hoffmann et al., 2004; Pascal et al., 1997). Other models use techniques to model fracture clustering (e.g., Ivanova et al., 1995; Meyer and Einstein, 2002).

Forward Modeling

The process of tunneling creates new fracture information on a continual basis. The challenge is being able to use this new data to update, validate, and improve the existing fracture model (Baecher, 1982). The forward modeling approach (e.g. Dershowitz, 1992; La Pointe et al., 1993; Long, 1993; Newman et al., 2003) is an excellent way to meet this challenge. The main idea of forward modeling is to build a model using assumptions based on existing data and then sample the model and compare the sampled data with analogous field samples. The model would be modified to fit the field sample. This process works well in tunneling. First, a fracture model is created based on preliminary studies. Then the first portion of a virtual tunnel is created in the model. Fracture data are recorded along the virtual tunnel and compared to data collected in the actual tunnel. The model is then updated based on the new information. This process continues as the tunnel is advanced.

3d Visualization

3d visualization techniques have been previously utilized in tunneling, mining and other underground applications (e.g., Bowman et al., 2006; Gaich et al., 2005; Kaiser et al., 2002; Opriessnig and Beer, 2001). Recent advances include the use of Virtual Environments (VE). VE software (Ray et al., 2006) has been developed for the AMADEUS project utilizing DIVERSE, a free Virtual Reality (VR) software package developed at Virginia Tech (Kelso et al., 2003). The AMADEUS software is scalable to many different visualization platforms such as desktop computers, GeoWalls (GeoWall Consortium, 2006), head mounted displays (HMD), and CAVEs, the last of which offers a fully immersive stereo VE (Cruz-Neira et al., 1993).

4.2 Field Site



Figure 4.1: North portal of Riverbend Tunnel. Note bedding dipping to the left (southeast) and sub-vertical fractures. There is a major solutionally enlarged fracture just inside this portal, as can be seen from the soil infilling that has spilled onto the tunnel floor.

The tunnel used in this study is an abandoned rail tunnel, referred to here as the *Riverbend Tunnel*, located in Giles County in the Valley and Ridge physiographic province of Southwest Virginia (Figures 4.1 & 4.2). The 229 m long tunnel is unlined and

was originally excavated approximately a hundred years ago as a railroad tunnel. Rectangular in cross section, the tunnel is approximately 5 m wide and 6 m high. The tunnel was never put in to use by the railroad.

4.2.1 Site Geology and Physiography

The tunnel is located in the Alleghany Mountains of Southwest Virginia and is part of the Appalachian foreland fold-thrust belt. The rock in the tunnel consists of Cambrian-age sandy dolomite of the Copper Ridge Formation (Bartholomew et al., 2000; Schultz et al., 1986). The tunnel is located through a ridge forming a bend in the river (Figure 4.2). The site and the surrounding area exhibit karst topography with several sinkholes in the vicinity (Figure 4.2 & 4.3a). Large near-vertical joints (Figure 4.3b) form large columnar structures on outcrops across the New River to the east. These joints also manifest themselves in the tunnel and are typically associated with karst features within the tunnel (Figure 4.4).

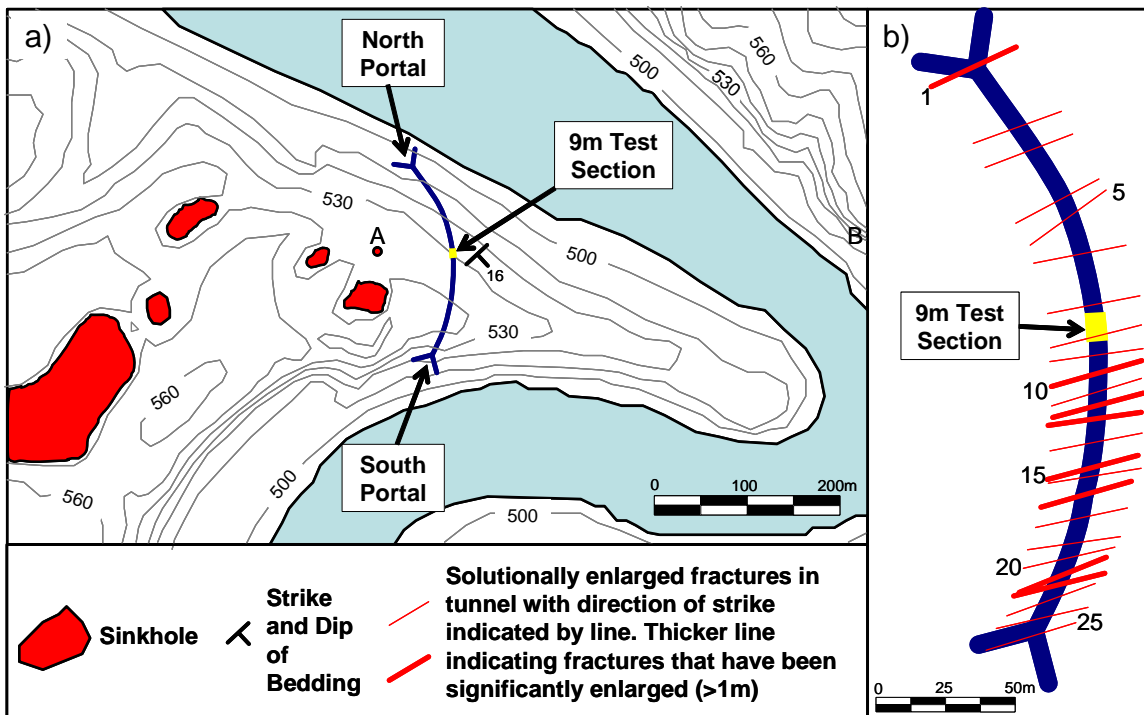


Figure 4.2: (a) Topographic map of site showing tunnel, sink holes and river; (b) view of tunnel showing solutionally enlarged fractures (numbered 1-25) and test section.

a)



b)



Figure 4.3: (a) Small sinkhole located at point A on Fig. 4.2, 80m west of the tunnel test section; (b) Near-vertical joints forming columnar structures along New River east of the tunnel, at point B on Fig. 4.2



Figure 4.4: Solutionally enlarged fracture No. 10, at Station 1+34.5 on right (west) wall of tunnel. Note vertical meter stick bottom center. Bedding dips to the left. Several fractures dip steeply to left-front on left side of picture. Solutionally enlarged fracture is earth filled with boulders or pinnacles. View is horizontal towards the southwest

4.3 Tools and Approach

The field study at the tunnel involved the use of many different tools to develop an approach that was efficient, accurate, and utilized technology. The approach includes using a relational database, imaging techniques, 3d visualization, custom software, and stochastic fracture modeling techniques along with forward modeling techniques. The study involved a general investigation of the tunnel and the surrounding area and a more detailed study of a 9 meter section of the tunnel (see Figure 4.2). The 9 m section for the detailed study was chosen to be in the central part of the tunnel, making it extremely dark, in order to test the imaging equipment for tunneling applications. This test section was divided up into three 3 meter intervals that represented three excavation stages. In each of these 3 meter intervals imaging of the right (west) wall and the roof of the tunnel was performed. Orientation measurements on fractures were taken throughout the 9 meter test section.

4.3.1 Database

This field study required the handling of large amounts of data. The use of an integrated relational database was therefore essential for organization of these data and the analyses of the data. The AMADEUS database, used for this field project, was designed and built to aid in the real-time evaluation and design of underground space (Decker et al., 2006). The database was developed using Microsoft Access and is capable of migrating to other platforms such as Oracle. The database was designed to store information about multiple projects and to also be used as a project specific database. The database was designed as a “Centralized Project Database” (Amor and Faraj, 2001) and consists of a centralized main database containing all processed data and models with five other individual databases containing raw data from the field. The databases are linked together using relational techniques to reduce data redundancy. Figure 4.5 gives a schematic of the AMADEUS Database. For this study the imaging data and geological field data databases were used along with the centralized AMADEUS database.

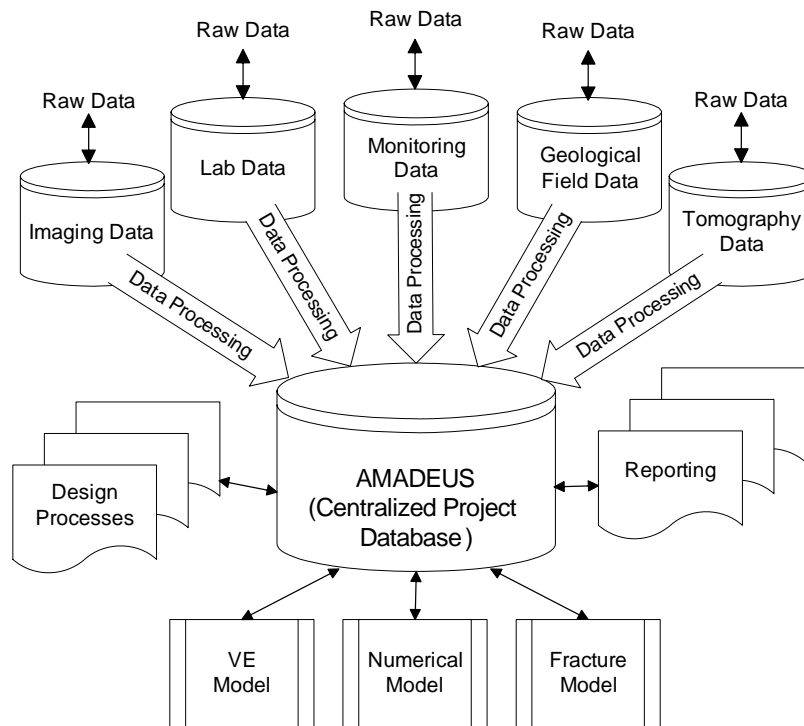


Figure 4.5: Schematic of AMADEUS database showing 5 raw data databases feeding processed data into the centralized project database which is being used for design, reporting and model building processes.

4.3.2 Imaging

Two different imaging techniques were used in the field. The first technique was the use of two Nikon D100 digital cameras to obtain color images and stereo pairs. The cameras were mounted on a custom bar for stereo imaging as shown in Figure 4.6. Four 500 watt halogen working lights were used to illuminate the rock for digital images. Figure 4.7 shows a color stereo pair taken of right (west) wall at station 1+12.5. The second technique was the use of a LiDAR scanner, ILRIS-3D from Optech, to obtain 3d point clouds representing the topography of rock surfaces, as well as the intensity of reflected waves at each point. The LiDAR scanner is shown in Figure 4.8 mounted on custom built cart for ease of movement in tunnel, and tilt table to allow scanning at various angles. In the tunnel, LiDAR reflection intensity values were returned for each raster point and the point cloud was visualized in grayscale. Using this method, data collection could be accomplished in complete darkness without the difficulties of providing a source of illumination. Figure 4.9 is an intensity point cloud made along the tunnel alignment at station 1+05.5. The use of digital photography and LiDAR allows for quick data acquisition during tunnel excavation with minimal loss of time and decreased exposure of personnel to possible hazards from unsupported tunnel sections.



Figure 4.6: Nikon 100D digital cameras mounted for stereo imaging.



Figure 4.7: Stereo pair of right (west) wall at station 1+12.5.



Figure 4.8: ILRIS-3D LiDAR scanner by Optech mounted on custom cart for transportation of scanner along tunnel. Tilt table allows scanning at various angles.



Figure 4.9: LiDAR scan along tunnel alignment with scanner at station 1+05.5. View is towards the south; the image shows intensity values only. The scan was taken without any artificial (visible) light.

4.3.3 Remote Creation of Trace Maps and Data Collection

After images were obtained they were brought back to the lab and processed using 3d visualization techniques and custom software to obtain additional orientation measurements and trace maps. Measuring the data and creating trace maps in the lab allows the excavation process to continue with minimal interruption for gathering geological data, and increases safety by limiting the time engineers and geologists must spend within unlined tunnel sections.

Digital images were used to create trace maps by digitally tracing the fracture traces. A variety of data were collected on the traces, and for some sections, data collection was computer-assisted by means of customized ImageJ software (Rasband, 2007).

Customized software was developed so that the 3d intensity images could be used for discontinuity measurements. The methodology used here with LiDAR data to calculate orientations of surfaces is similar in concept to other developed methods used in conjunction with LiDAR (e.g., Donovan et al., 2005) and terrestrial photogrammetry (e.g., CSIRO, 2007; Gaich et al., 2005).

In this study, 3d visualization techniques were used to enhance the process of creating the trace maps and obtaining orientation measurements. The visualization allowed us to see the rock as we did when we were in the tunnel. The stereo pairs were visualized using a GeoWall built for the AMADEUS project. The GeoWall consists of a passive stereo system using two projectors with polarized images as shown in Figure 4.10. Polarized glasses are used to view the image in stereo. The LiDAR data were visualized with the AMADEUS GeoWall using the AMADEUS 3d visualization software. The fracture models were also viewed in 3d using the AMADEUS 3d visualization software for verification and enhanced visual understanding of the models. In this study, desktops and the AMADEUS GeoWall were used to view most 3d data; however, a few data sets were viewed with the CAVE at Virginia Tech as seen in Figure 4.11.



Figure 4.10: Two projectors for AMADEUS GeoWall shown with polarizing lenses.



Figure 4.11: Fully immersive viewing of LIDAR 3d data within CAVE at Virginia Tech. The researcher is wearing polarized glasses and is holding a wand that controls navigation within the VE.

4.3.4 Analysis of Data

Once trace maps were created and other measurements were taken using the image data, the maps and data were then analyzed using statistical methods to determine statistical fracture set parameters. The orientation data was analyzed by plotting the data on stereonet and determining the mean orientation and the Fisher dispersion parameter with consideration of sampling biases. The mean trace length, trace density P_{20} , and trace intensity P_{21} were determined by using endpoint estimators (Mauldon et al., 2001) and stereological estimators (Decker and Mauldon, 2007b). The trace length CDF was determined by using the Kaplan-Meier method (Kaplan and Meier, 1958) modified for rock fracture traces, *K-M-trace* (Decker and Mauldon, 2006; Decker and Mauldon, 2007a).

4.3.5 Fracture Model and Forward Modeling

Fracture size, shape and intensity were quantified by using a combination of statistical methods along with forward modeling. The fracture size and shape (aspect ratio and elongation direction) were estimated with the custom spreadsheet application, *DEfrac* which uses Differential Evolution for optimization (Decker and Mauldon, 2006). This optimization technique was designed for use with fracture data in tunnels and requires trace data on two or more non-parallel sampling planes. The fracture intensity P_{32} was determined by matching observed trace intensity P_{21} to simulated fracture populations and adjusting the intensity of the simulated fractures so that the simulated trace density and observed trace density were equivalent. The simulated fracture populations were created using FracWorks (Golder and Associates, 2004).

The fracture size and intensity were also evaluated by means of forward modeling techniques. These techniques were used after the initial fracture model was completed and data from the first interval was obtained. The forward modeling technique takes the trace and orientation data obtained in the field and directly compares it with simulated sampling of the fracture model. The input data for the simulated fracture are then adjusted to match the actual sampling. The simulated sampling was carried out using FracWorks. The fracture models built using FracWorks were visualized in 3d using the AMADEUS visualization software. The software contains a novel virtual tunnel excavation tool (Ray et al., 2006). Figure 4.12 shows an excavated 3d fracture model with a circular sampling area defined on the tunnel wall.

The fracture models, as previously stated, were developed in FracWorks and visualized in stereo using the AMADEUS 3d visualization software. The models were developed using the fracture parameters, obtained using the above methods, along with other geological consideration such as regional fractures and fracture hierarchies. The fracture models were for the most part stochastic; however, major structures such as solutionally enlarged fractures associated with the large vertical fractures encountered, were deterministically placed in the model.

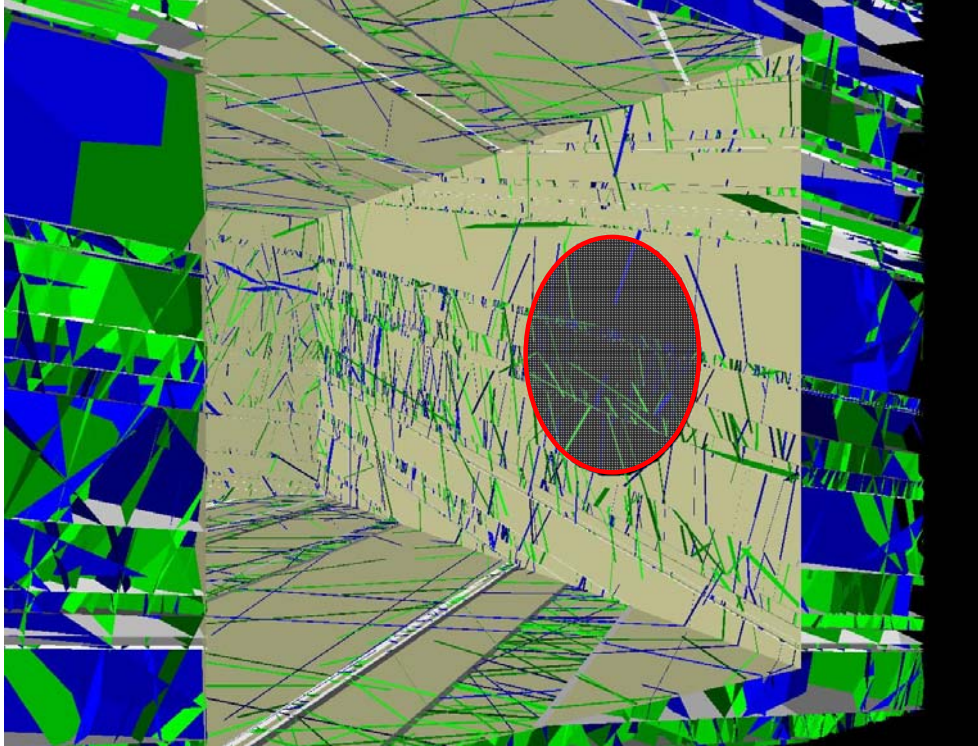


Figure 4.12: Excavated 3d fracture model with circular sampling area on right wall (dark circle).

4.4 Field Study Results

Data obtained in the field were used to analyze and describe the geological setting of the tunnel site. The data were also utilized to build stochastic fracture models. These models were built sequentially, as if the tunnel were being excavated. First a preliminary model was developed and assembled in FracWorks. Then the model was verified and updated as data were obtained within the three intervals of the 9 meter test section of the tunnel.

4.4.1 Preliminary Fracture Model

The preliminary fracture model was based upon limited measured data obtained near the north portal and general observations in the tunnel and vicinity. It was determined that bedrock at the site contained two principal directions of fracturing, which were approximately orthogonal to one another and also orthogonal to bedding. With bedding included, this would make three fracture sets. However, a fourth set, consisting of major solutionally-enlarged fractures was also present, oriented parallel to the first of

the primary fracturing directions. Therefore, the fractures at the site included two near-vertical cross joints (sets 1 & 2), bedding (set 3), and a set of solutionally-enlarged and extensive fractures (set 4) parallel to set 1. The large vertical fractures were encountered approximately every 9 meters along the tunnel. Sets 1 & 2 were observed to be bed-contained in most cases.

Orientations for sets 1, 2 & 3 were measured near the portal while the strikes of all 25 solutionally enlarged fractures in the tunnel were measured assuming a dip of 90° . The poles of these orientation data were plotted on a lower hemisphere equal area stereonet (Lisle and Leyshon, 2004) in Figure 4.13 with the different sets shown using different symbols. The mean orientation of each set was determined, correcting for the sampling biases for sets 1, 2 & 3, which were well within the range of applicability of the Terzaghi correction factor (R. Terzaghi, 1965). For sets 1 & 2 a Fisher distribution was assumed and a dispersion parameter was determined. The orientation distribution for set 3 (bedding) and set 4 was assumed to be constant.

The mean trace length, P_{20} , and P_{21} for set 1 was determined using a trace map created from a digital image, with a circular sampling window superposed (Figure 4.14). Set 2 was nearly parallel with the sampling window and thus no parameters were obtained. For set 3 (bedding) the traces were all persistent and the only parameter calculated was the 1d intensity P_{10} , which was determined using a vertical scanline on the trace map. The P_{10} of bedding was determined to be 3.54 m^{-1} .

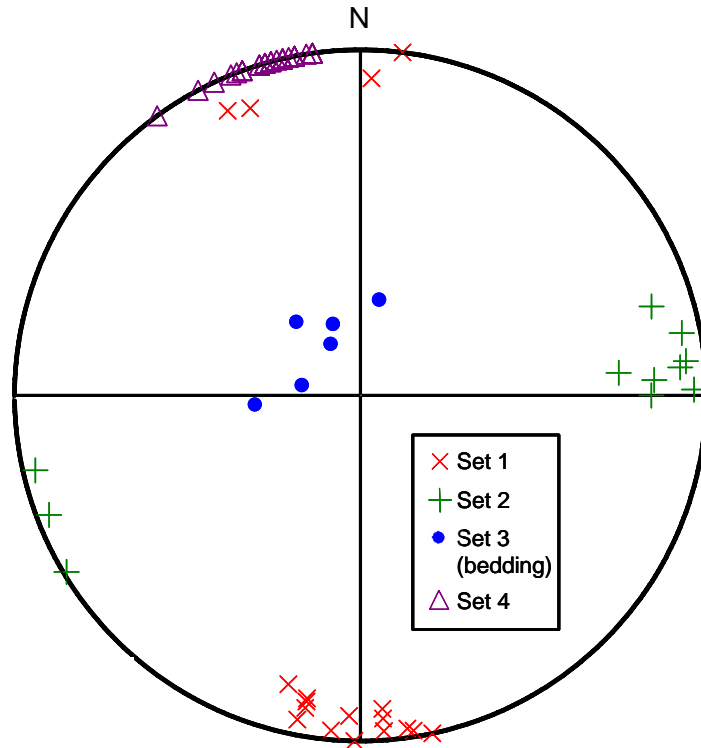


Figure 4.13: Lower hemisphere equal area stereonet plot of poles of orientation measurements taken near north portal. The stereonet was made using XStereo, a spreadsheet program developed primarily for teaching at Virginia Tech.

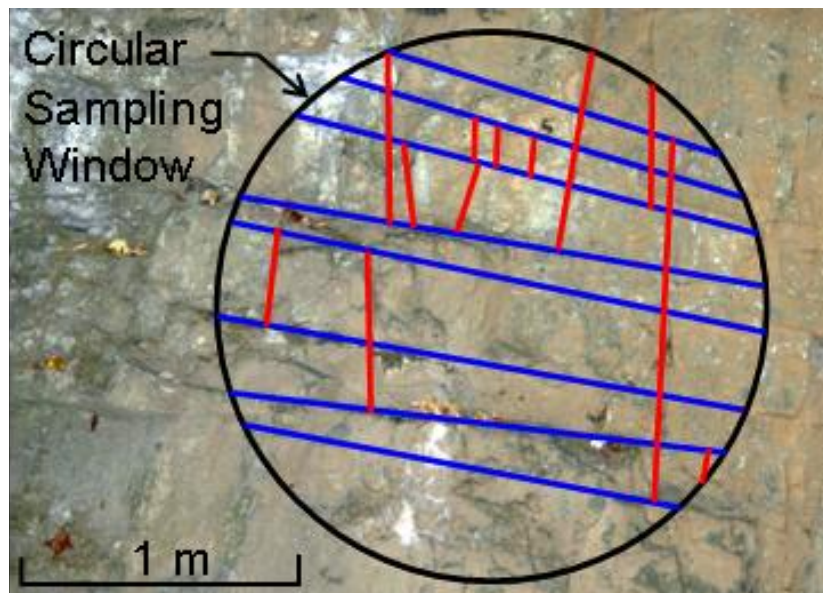


Figure 4.14: Trace map created from digital image of rock wall near north portal with traces from Set 1 (red, sub-vertical) and Set 3/bedding (blue, sub-horizontal).

Table 4.1: Trace data obtained from circular sampling window for set 1.

Measure	Symbol	Units	Estimator Type	Set 1
Density	P_{20}	m^{-2}	Stereological	2.75
			Endpoint	3.18
Intensity	P_{21}	m^{-1}	Stereological	1.68
			Endpoint	0.99
Mean Trace Length	$\tilde{\mu}_l$	m	Stereological	0.61
			Endpoint	0.31
Slope of CDF	$\tilde{\psi}$	rise/run	-	0.60

For the preliminary model, *DEfrac* was not used since only one sampling window was utilized to obtain trace data. The fracture model parameters for fracture size were instead initially determined using observations to formulate some assumptions. The main observation was that sets 1 and 2 were nearly always bed-contained and that the estimated mean trace length was approximately equal to the bed spacing. Therefore for the model, it was assumed that sets 1 and 2 were 100% bed-contained, that the fractures were long slender rectangles, and that their elongation direction was along strike. A preliminary fracture model (Table 4.2) was created for input into the fracture system simulation package, FracWorks. An effort was made to keep the preliminary model as simple as possible. Sets 1 and 2 were modeled as being bed contained. This being the case, FracWorks will truncate fractures on bedding planes, and the size of most fractures will end up being controlled by bed spacing. However, an initial size is required in the preliminary model and this was taken to be constant and larger than mean bed spacing. Since no data was obtained from the trace map for set 2, it was assumed that sets 1 & 2 would have similar parameters for size and density and thus were modeled with the same parameters. Bedding planes (set 3) were assumed to be continuous in the model. The preliminary model had dimensions of a cube with edge length 10 meters to include the entire 9 meter test section and for ease of use with the visualization software, which tends to be sluggish with larger models. For quantitative analysis (involving e.g., groundwater flow, rock block kinematics) the model dimensions would need to be larger in order to

reduce edge effects. In all cases, the generation region needs to be larger than the analysis or visualization region, again in order to avoid edge effects (e.g., Gilmour et al., 1986). It was assumed that at least one large vertical joint (set 4) would be encountered in the region; indeed, 25 such fractures were observed along the length of the 229 m tunnel. Therefore, one fracture of set 4 was randomly placed within the model. Table 4.2 gives the preliminary fracture parameters used in FracWorks. The preliminary fracture model is shown with a virtual excavation of 10 meters, from station 1+11 to 1+21 in Figure 4.15.

Table 4.2: Fracture parameters for preliminary fracture model

	Unit	Set 1	Set 2	Set 3	Set 4
Description	-	Cross joint	Cross joint	Bedding	Major Fractures
Mean Dip Direction,	°	1	260	135	160
Mean Dip	°	86	82	15	90
Orientation distribution	-	Fisher, $\kappa = 40$	Fisher, $\kappa = 40$	constant	constant
Elongation Trend	°	91	170	-	-
Elongation Plunge	°	0	0	-	-
3d intensity, P_{32}	m^{-1}	2.5	2.5	4.20	0.1
Aspect Ratio	m	10	10	1	1
Termination % on bedding	%	100	100	0	0
EFR Mean	m	3.57	3.57	Inf.	Inf.
EFR Standard Deviation	m	0	0	0	0
EFR Distribution	-	Constant	Constant	Constant	Constant

(EFR = Equivalent Fracture Radius)

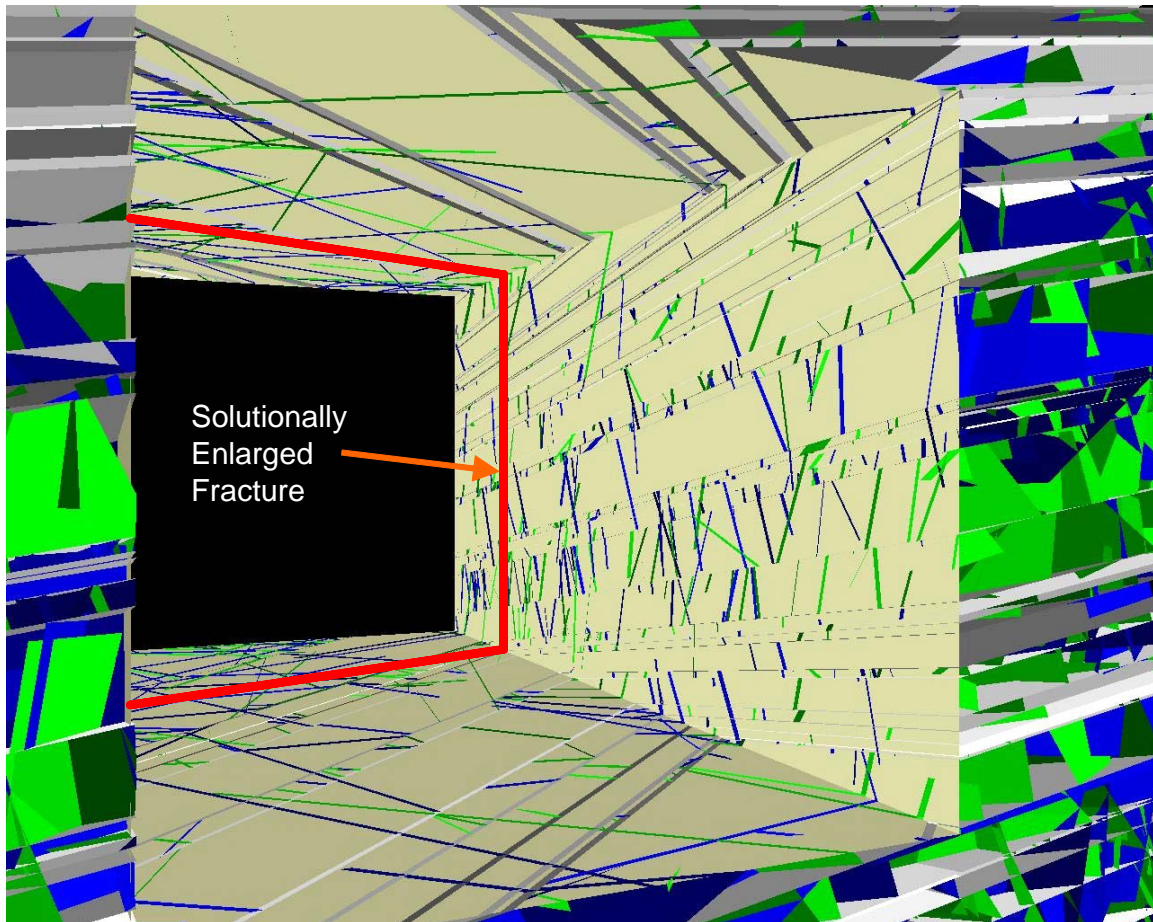


Figure 4.15: Preliminary fracture model with virtual excavation from station 1+11 to 1+21.

4.4.2 Forward Modeling – Updating Fracture Model

The preliminary model was updated and modified as needed, after analysis of new data obtained from each new interval within the test section. The results from the first interval, along with an updated model are presented below. Subsequent to that, the final model will be presented, along with some discussion of the modeling process and how it evolved as more data were obtained.

Interval 1, Test Section: Station 1+11 to 1+14

There were no field orientation measurements taken in the field within interval 1. Additional orientation measurements, however, were obtained using two LiDAR scans of the right (west) wall and one scan of the roof. An additional 13 orientation measurements were obtained from the LiDAR images. It should be noted that 5 orientation measurements on the roof were obtained for set 3 (bedding). The roof consisted of

several beds and was ideal for taking bedding plane orientation measurements. The roof, however, would have been extremely difficult to access for orientation measurements in the field. Figure 4.16 gives a lower hemisphere equal area stereonet plot of poles with the new data points added (circled) and the fracture sets defined. The data plotted in Figure 4.20 were used with a bootstrapping method to generate sets 1 & 2 within FracWorks.

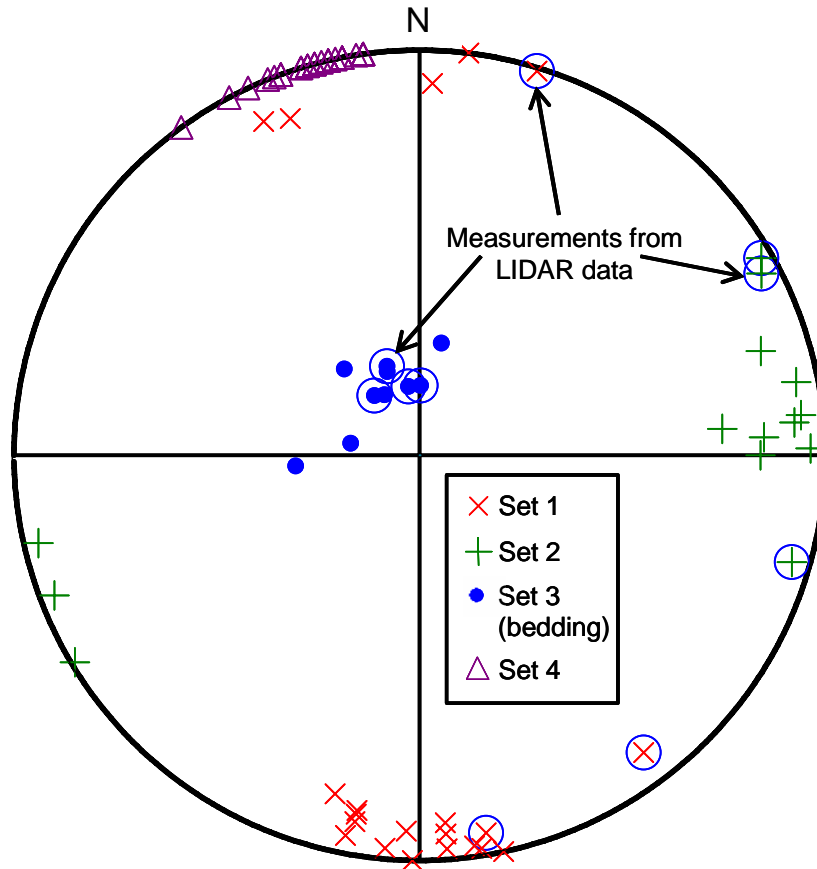


Figure 4.16: Lower hemisphere equal area stereonet plot of poles with added measurements from LiDAR images (LiDAR measurements circled)

Two circular windows were analyzed using digital images of the right (west) wall and roof for interval 1. The trace maps are shown in Figure 4.17. The trace map on the right (west) wall contains traces for sets 1 & 3, with set 2 being nearly parallel with the wall. The trace map on the roof contains traces for sets 1& 2. For the roof trace map, traces for set 3 (bedding) were not fully observed because the roof was not a true planar surface, instead it consisted of bedding planes that abruptly stepped to each other due to cross joints (typically set 1). The transition, therefore, from one bedding plane to the

other was typically characterized by a trace representing set 1 or 2 (Figure 4.18). The trace map on the right (west) wall was used to get another estimate of the linear intensity, P_{10} , along a vertical scanline for set 3. The estimate of P_{10} obtained was 3 fracture traces per linear meter. No fractures from set 4 were encountered within the sampling windows, nor were observed in interval 1. Table 4.3 gives the estimate trace parameters for sets 1 & 2 from the trace maps in Figure 4.17.

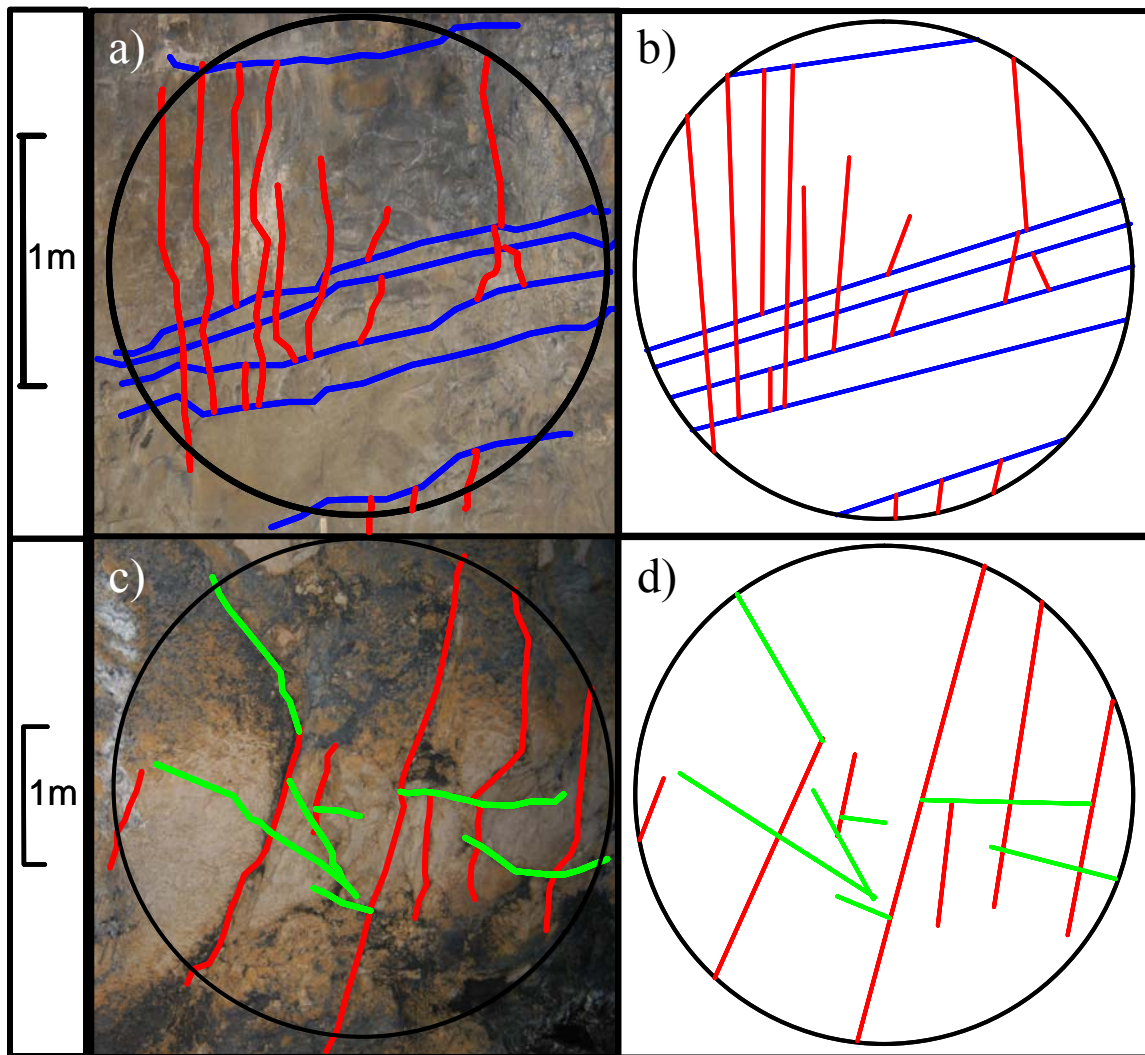


Figure 4.17: Trace maps created from digital images of right (west) wall ((a) digital image with trace fractures, (b) equivalent straight lines for measurement, set 1 (red) sub-vertical and set 3/bedding (blue) sub-horizontal) and roof ((c) digital image with trace fractures, (d) equivalent straight lines for measurement, set 1 (red) sub-vertical and set 2 (green) sub-horizontal) in tunnel.



Figure 4.18: Digital image of the roof showing abrupt steps to bedding planes.

Table 4.3: Trace data obtained from circular sampling windows on right (west) wall and roof of interval 1 for set 1 and set 2.

Measure	Symbol	Units	Estimator Type	Right (west) Wall		Roof	
				Set 1	Set 2	Set 1	Set 2
Density	P_{20}	m^{-2}	Stereological	2.99	-	0.31	0.61
			Endpoint	3.66	-	0.42	0.73
Intensity	P_{21}	m^{-1}	Stereological	2.81	-	1.15	0.60
			Endpoint	1.75	-	0.86	0.29
Mean Trace Length	$\tilde{\mu}_t$	m	Stereological	0.94	-	3.75	0.99
			Endpoint	0.48	-	2.06	0.39
Slope of CDF	$\tilde{\psi}$	rise/run	-	1.00	-	0.35	-

An analysis of set 1 was conducted using the trace data sampled on the right (west) wall and roof at 1+12.5 and the portal with *DEfrac* (See Tables 4.1 & 4.3). *DEfrac* was run 100 times and the average parameters, including their standard deviations are recorded in Table 4.4. The analysis indicates that set 1 is likely elongated along strike and that the aspect ratio is approximately 3.

Table 4.4: Fracture parameters obtained for Set 1 from *DEfrac* analysis after interval 1.

Fracture Parameter	Unit	Set 1	
		Mean	Standard Deviation
Mean Equivalent Fracture Radius	m	0.50	0.02
Elongation Trend	°	280.5	18.6
Elongation Plunge	°	11.4	-
Aspect Ratio	-	3.23	0.55

After analyzing the new data obtained from interval 1, several modifications were made to the preliminary model. The orientation of sets 1, 2 & 3 were modified to reflect the new measurements. Set 1 & 2 were modified to match the new intensity measurements. Set 1 & 2 were also modified by changing the aspect ratio and the size distribution to better match the data obtained using the roof trace map and the *DEfrac* analysis. A negative exponential size distribution with a limit on how small the fracture can be was chosen, so that the bedding planes would still control the size distribution perpendicular to strike. Set 3 (bedding) was modified to reflect the new intensity data gathered. The new P_{10} measurement was averaged with the preliminary P_{10} measurement in the case of Set 3. As with the preliminary model, one solutionally enlarged fracture (set 4) was placed randomly within the model.

After the above modifications were made, the fracture model was sampled and checked to see how well it matched the new data. The model was modified some to obtain the best fit with the final model inputs given in Table 4.5. Figure 4.19 is the new updated model excavated 10 meters from station 1+11 to 1+21.

Table 4.5: Fracture parameters input into FracWorks after considering *DEfrac* analysis and forward modeling analysis for Interval 1.

	Unit	Set 1	Set 2	Set 3	Set 4
Description	-	Cross joint	Cross joint	Bedding	Major Fractures
Mean Dip Direction	°	359	279	148	160
Mean Dip	°	86	83	15	90
Orientation distribution	-	bootstrap	bootstrap	constant	constant
Elongation Trend	°	89	9	-	-
Elongation Plunge	°	0	0	-	-
3d intensity, P_{32}	m^{-1}	1.6	0.5	3.6	0.1
Aspect Ratio	m	1.5	1	1	1
Termination % on bedding	%	95	100	0	0
EFR Mean	m	1.4	0.56	Inf.	Inf.
EFR Standard Deviation	m	1.4	0.56	0	0
EFR Distribution	-	Exp.	Exp.	Constant	Constant
EFR Truncation	m	0.7	0.28	none	none

(EFR = Equivalent Fracture Radius)

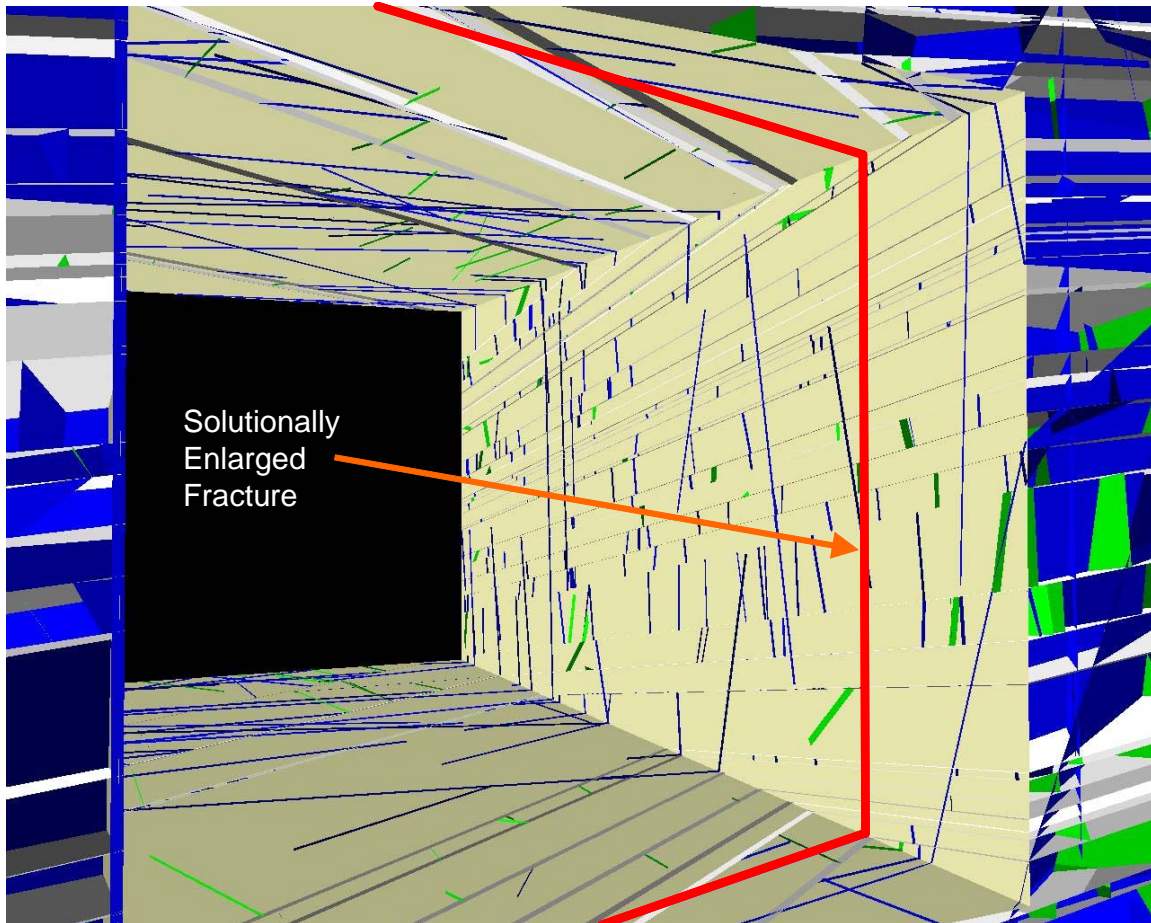


Figure 4.19: Updated fracture model after the analysis of interval 1 with a virtual excavation from station 1+11 to 1+21.

Once the fracture model was completed, virtual sampling was conducted within the updated model and the preliminary model to compare how well the updated model matched the new data obtained in interval 1 as compared with the preliminary model. For each sampling window three virtual samples were taken within the model and the average parameters obtained from those examples are given in Table 4.6 along with the measured data. The new model compares well with the estimated mean trace length from the sampled data for both sets 1 & 2. The estimated density is a good fit also for set 2, but not as good for set 1. The right (west) wall sampling indicated higher fracture intensity than the roof. The intensity used in the model was between the values indicated by the right (west) wall and the roof with a little more weight given to the value on the right (west) wall. It is likely that the roof was less representative due to the stepped nature of the roof as discussed earlier.

Table 4.6: Results of virtual sampling of updated model and preliminary model after analysis of interval 1. Comparison also shown with measured field data.

Sampling Window			Right (west) Wall	Roof	Roof
Set No.			1	1	2
Mean Trace Length $\tilde{\mu}_i$, m	Stereological Estimator	Field Measurement	0.9	3.8	1.0
		Preliminary Model	0.2	1.7	0.8
		Updated Model	0.4	2.6	0.7
	Endpoint Estimator	Field Measurement	0.5	2.1	0.4
		Preliminary Model	0.3	2.0	1.2
		Updated Model	0.5	2.5	0.7
Trace Density P_{20} , m^{-2}	Stereological Estimator	Field Measurement	3.0	0.3	0.6
		Preliminary Model	4.7	1.4	1.8
		Updated Model	3.1	1.1	0.6
	Endpoint Estimator	Field Measurement	3.7	0.4	0.7
		Preliminary Model	4.3	1.4	1.6
		Updated Model	3.1	1.1	0.6
Trace Intensity P_{21} , m^{-1}	Stereological Estimator	Field Measurement	2.8	1.2	0.6
		Preliminary Model	1.0	2.5	1.4
		Updated Model	1.4	2.8	0.4
	Endpoint Estimator	Field Measurement	1.8	0.9	0.3
		Preliminary Model	1.6	2.7	1.9
		Updated Model	1.4	2.7	0.4

Final Model: Station 1+11 to 1+20

After analyzing data from two more intervals, station 1+14 to 1+17 and 1+17 to 1+20, a final fracture model was created. Only slight changes were made to the model from interval 1 to the final model. Figure 4.20 is a lower hemisphere equal area stereonet plot of poles for all the manual measurements and LiDAR measurements. A number of manual measurements were taken within intervals 2 & 3. In Figure 4.20 these additional manual measurements within the tunnel are enclosed by red squares, the LiDAR measurements are enclosed by blue circles, and the preliminary manual measurements are not enclosed. The LiDAR measurements compared well with the manual measurements. The LiDAR measurements were especially useful for the bedding, were LiDAR measurements were taken on the roof which consisted of bedding planes that could not be measured in the field. The orientation data was utilized to create the final model using a bootstrap procedure in FracWorks as used for interval 1.

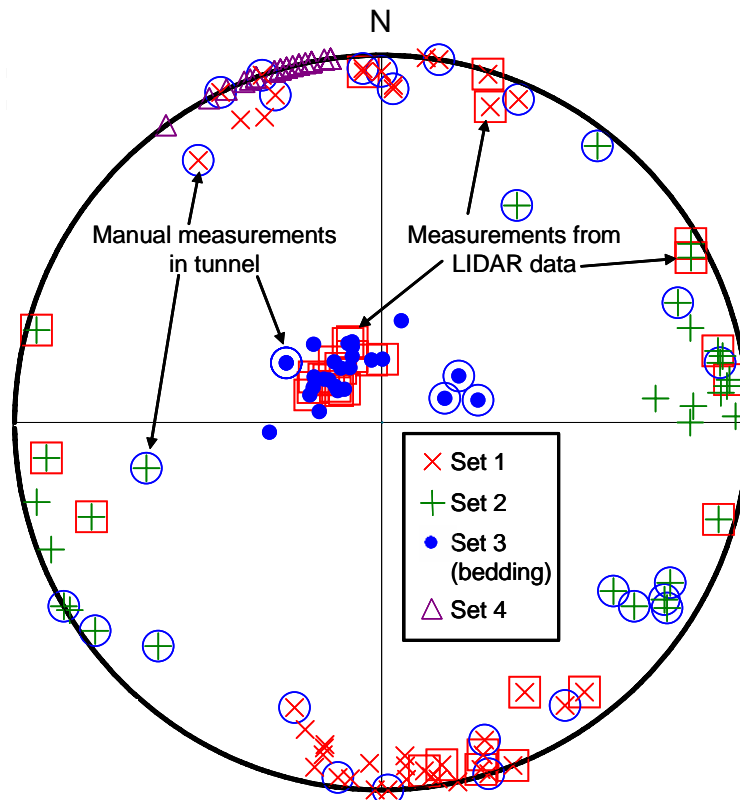


Figure 4.20: Lower hemisphere equal area stereonet plot of poles with added measurements from additional manual measurements in tunnel (enclosed by red squares) and LiDAR images (enclosed by blue circles).

The trace map analyses of the intervals 2 and 3 were similar to interval 1 and confirmed the validity of the model. For set 1, the intensity and mean trace length (increased by decreasing the termination percentage) was slightly increased to better fit the field data. The analysis at interval 3 showed a longer mean trace length and higher intensity for set 1. Observations in the tunnel indicated an increase in non-bed contained fractures for set 1 near solutionally enlarged fractures (set 4). This observation may explain the increase in mean trace length of intensity for interval 3 which contained a solutionally enlarged fracture (set 4). The statistics for set 2 were fairly consistent throughout the tunnel. Set 2 was mostly bed contained with short traces. For the final model set 2 was simulated with a constant size distribution and 100% terminated on set 3 (bedding). The size distribution, therefore, was affected by the spacing of the bedding. Table 4.7 gives the input parameters for the final fracture model. At Station 1+19.7 on the right (west) wall solutionally enlarged fracture No. 8 (set 4) was encountered which exhibited an aperture of approximately 0 to 1 m and a strike of 76° . This set 4 fracture was placed deterministically into the fracture model (see Figure 4.21). Figure 4.21 is the final fracture model shown unexcavated and excavated.

Table 4.7: Final fracture parameters input into FracWorkXP for station 1+11 to 1+21

	Unit	Set 1	Set 2	Set 3	Set 4
Description	-	Cross joint	Cross joint	Bedding	Major Fractures
Mean Dip Direction	°	355	275	137	*166
Mean Dip	°	87	87	16	90
Orientation distribution	-	bootstrap	bootstrap	constant	constant
Elongation Trend	°	85	5	-	-
Elongation Plunge	°	0	0	-	-
3d intensity, P_{32}	m^{-1}	2.0	0.5	3.6	0.1
Aspect Ratio	m	1.5	1	1	1
Termination % on bedding	%	90	100	0	0
EFR Mean	m	1.4	0.56	Inf.	Inf.
EFR Standard Deviation	m	1.4	0	0	0
EFR Distribution	-	Exp.	Constant	Constant	Constant
EFR Truncation	m	1.4	none	none	none

(EFR = Equivalent Fracture Radius)

*Mean dip direction used for Set 4 was determined by field strike measurement of solutionally enlarged fracture No. 8.

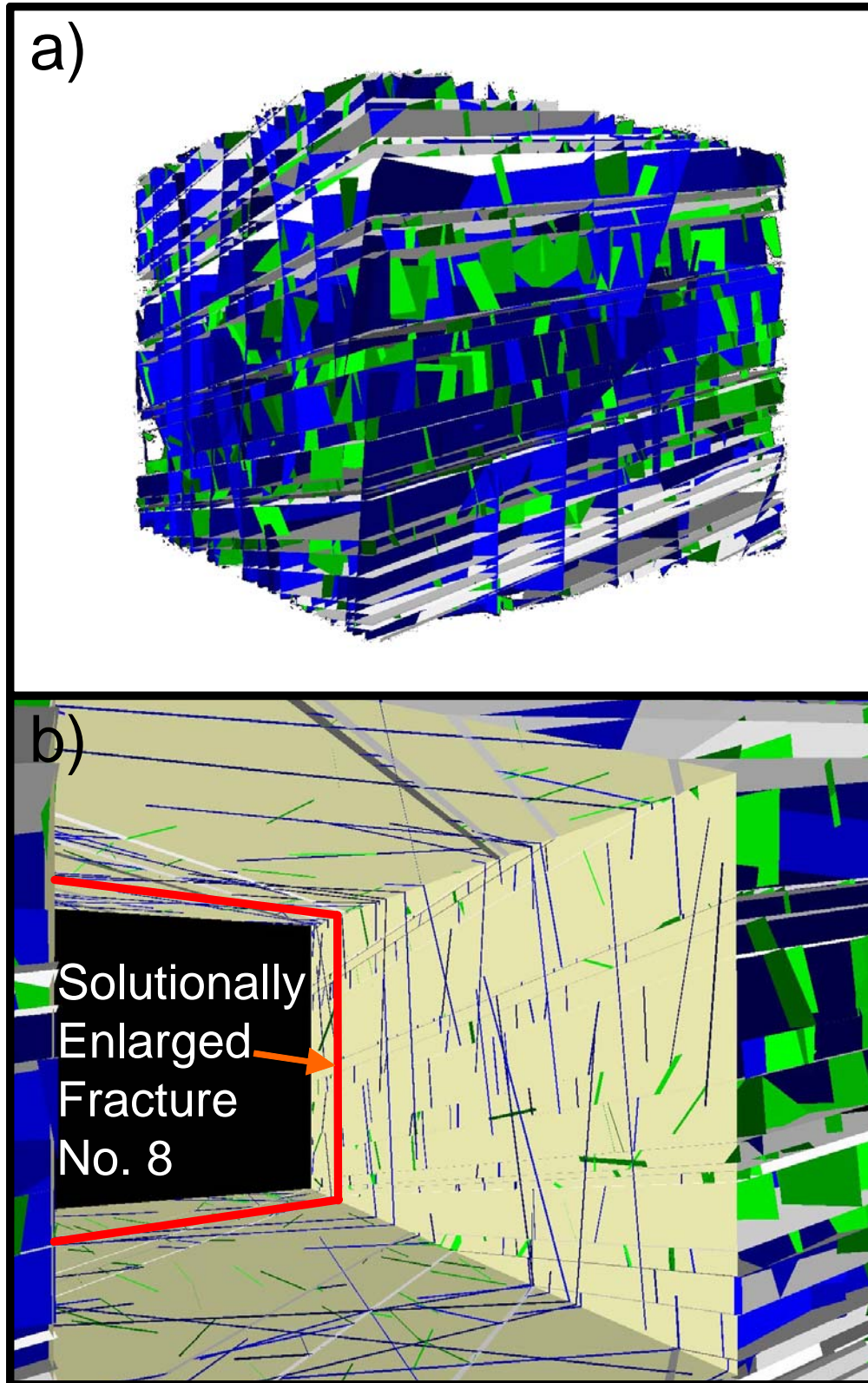


Figure 4.21: Final fracture model: a) not excavated, b) excavated with the location of the existing solutionally enlarged fracture No. 8.

Forward modeling allows engineers to match the fracture model with the actual fracture network by comparing field data with simulated data and by visually comparing the model with what can be seen in the field. Data comparison and visual comparison were used together in this forward modeling process. Figure 4.22 shows the actual trace maps at station 1+18.5 on the right (west) wall and roof compared to typically trace maps in the final fracture model sampled on planes parallel to the right (west) wall and roof. The field trace maps compare well with the simulated trace maps. The orientation distribution had more variance in the simulated data, especially for the roof (see Figure 4.26). This may be due to the variation in measurements which is likely caused by error and the location of the measurement on the fracture, since the fractures are not always flat planes indicated by the traces not being straight (see Figure 4.22a,c).

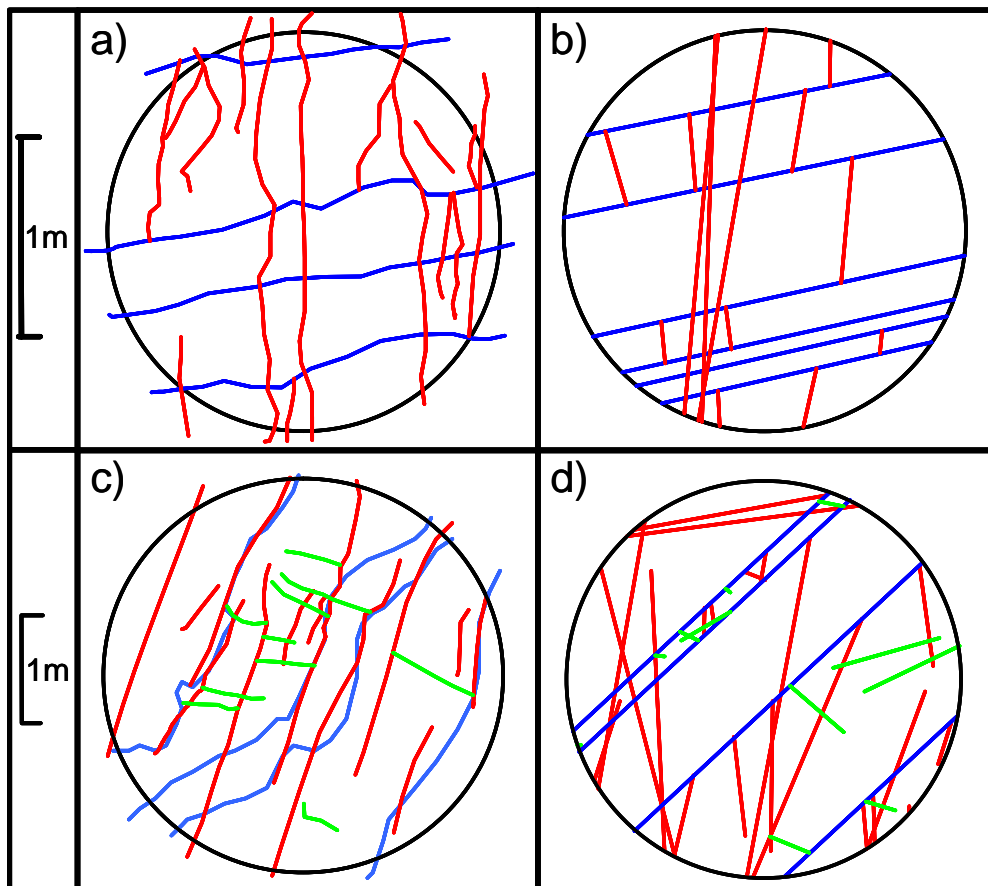


Figure 4.22: Comparison between actual trace maps and simulated trace maps. Trace maps from between station 1+17 and 1+20 on the right (west) wall (a) and the roof (c). Simulated trace maps created on planes parallel to the right (west) wall (b) and the roof (d).

Forward modeling for fracture networks that has been applied in this paper is only a small example of what can be done when data is obtained and used during the tunneling process. This data can also be utilized to update rock quality indexes that are used frequently in tunneling (such as RMR or Q-system) and rock parameters. Also, the imaging data gives engineers and geologists a chance to see the geology and fracture data without being at the tunnel site, and to keep a continuous record of conditions for future reference.

4.5 Conclusions

- The utilization of fracture data obtained during tunneling requires a carefully designed plan to quickly obtain, process, and store the data.
- The use of an integrated relational database is essential to organize and use fracture data obtained during tunneling.
- Fracture data can be obtained during the tunneling process quickly and safely using technologies such as digital stereo photography and laser scanning.
- The use of 3d technologies can enhance the use and understanding of imagery data from within tunnels.
- Remote orientation measurements can be accurately taken using LiDAR data.
- Trace maps can be quickly and accurately created using digital stereo images. Scanlines and other sampling procedures can also be conducted using digital images.
- Remote sampling can reduce the amount of time engineers and geologists need to spend in the unsupported section of the tunnel, thus reducing safety concerns.
- Statistical estimators, along with observation, can be used to update and verify fracture models as more data is obtained during excavation.
- The forward modeling procedure can be used to adjust fracture models to fit field data and observations. The more field data obtained, the better the model becomes.

- Obtaining data in real time during tunnel excavation allows engineers and geologists to increase safety and save money as ground conditions are better understood.
- Data obtained within tunnel can also be used to update rock quality indices used frequently in tunneling processes, be used by engineers and geologists to see the geology and fracture data without being at the tunnel site, and be used to make a continuous record of the tunnel geology before it is lined.

4.6 Acknowledgements

The study presented in this paper is based upon work that is supported by the National Science Foundation under grant number CMS 0324889. Any opinions, findings and conclusions or recommendations expressed in this paper are those of the authors and do not necessarily reflect the views of the National Science Foundation.

The author would also like to recognize all the priceless contributions that have made this paper possible. The individuals and their contributions are as follows: Dr. Matthew Mauldon, guidance, help with revisions, and instrumental in securing access to the tunnel site, Dr. Marte Gutierrez, guidance and support as the principle investigator for AMADEUS; Dr. Joe Dove guidance and support with imaging equipment and custom software and help with revisions; Justin Sommerville, help with field study and maintaining database; Sotiros Vardokas, help with field study and support with 3d visualization equipment; Brian Badillo, support with custom software; Dr. Doug Bowman and Andrew Ray, support with 3d visualization software and equipment.

The author would also like to extend a special thanks to the private land owners who gave us permission to cross their land to access the tunnel.

References

- Amor, R. and Faraj, I., 2001. Misconceptions about Integrated Project Databases. *ITcon*, 6: 57-68.
- Baecher, G.B., 1982. Statistical methods in site characterization Updating subsurface samplings of soils and rocks and their in-situ testing Engineering Foundation, Santa Barbara, California, pp. 463-492.

- Baecher, G.B., Lanney, N.A. and Einstein, H.H., 1977. Statistical description of rock properties and sampling. In: F.D. Wang and G.B. Clark (Editors), Proceedings of the 18th U.S. Symposium on Rock Mechanics. Colorado School of Mines, Sante Fe, New Mexico, pp. 5C1.1-5C1.8.
- Bai, T. and Pollard, D.D., 2000. Closely spaced fractures in layered rocks: Initiation mechanism and propagation kinematics. *Journal of Structural Geology*, 22(10): 1409-1425.
- Bartholomew, M.J., Schultz, A.P., Lewis, S.E., McDowell, R.C. and Henika, W.S., 2000. Digital Geological Map of the Radford 30 by 60 Minute quadrangle, Virginia and West Virginia, Virginia Department of Mines Minerals and Energy, Division of Mineral Resources Preliminary Draft.
- Bowman, D., Ray, A., Gutierrez, M., Mauldon, M., Dove, J., Westman, E. and Setareh, M., 2006. Engineering in Three Dimensions: Immersive Virtual Environments, Interactivity, and 3D User Interfaces for Engineering Applications. In: D.J. DeGroot, J.T. DeJong, J.D. Frost and L.G. Baise (Editors), Proceedings of ASCE GeoCongress, 2006. ASCE, Atlanta, GA.
- Cooke, M.L. and Underwood, C.A., 2001. Fracture termination and step-over at bedding interfaces due to frictional slip and interface opening. *Journal of Structural Geology*, 23: 223-238.
- Cruz-Neira, C., Sandin, D.J. and DeFanti, T.A., 1993. Surround-screen projection-based virtual reality: The design and implementation of the CAVE, Proceedings of the Computer Graphics International Conference, pp. 135-142.
- CSIRO, 2007. Sirovision, <http://www.surpac.com/Sirovision.asp#overview>, Surpac Website, Accessed 03-21-07.
- Decker, J.B., Antony, A., Ray, A., Vardakos, S., Murphy, M.M., Mauldon, M., Dove, J.E., Gutierrez, M., Bowman, D.A. and Westman, E., 2006. An Integrated Relational Database for Tracking Rock Mass Data During Tunnelling, Proceedings of the ITA-AITES 2006 World Tunnel Congress and 32nd ITA General Assembly, Seoul, South Korea, April 22-27, Paper No 312.
- Decker, J.B. and Mauldon, M., 2006. Determining Size and Shape of Fractures from Trace Data using a Differential Evolution Algorithm. In: D.P. Yale, S.C. Holtz, C. Breeds and U. Ozbay (Editors), Proceedings of the 41st U.S. Symposium on Rock Mechanics, Golden, Colorado, pp. Paper No. 969.
- Decker, J.B. and Mauldon, M., 2007a. Determining Size and Shape of Fractures from Trace Data using a Differential Evolution Algorithm. Not Yet Published.
- Decker, J.B. and Mauldon, M., 2007b. Generalized Stereological Estimator for Mean Fracture Trace Length and Density. Not Yet Published.
- Deng, B.-W., Lee, C.-H. and Chang, J.-L., 1995. Characterization and interpretation of variability of fracture pattern in jointed andesites, Lan-Yu, Taiwan. *Chung-Kuo Kung Ch'Eng Hsueh K'An/Journal of the Chinese Institute of Engineers*, 18(6): 787-799.

- Dershowitz, W., 1979. A Probabilistic Model for the Deformability of Jointed Rock Masses. M.S. Thesis, MIT, Cambridge, Massachusetts.
- Dershowitz, W., 1992. Interpretation and synthesis of discrete fracture orientation, size, shape, spatial structure and hydrologic data by forward modelling. In: C. Myer, Goodman, & Tsang (Editor), Proceedings of the Conference of Fractured and Jointed Rock Masses. Balkema, Rotterdam, Lake Tahoe, California, USA, pp. 579-586.
- Dershowitz, W.S., 1985. Rock joint system, MIT, Cambridge, Mass.
- Dershowitz, W.S. and Einstein, H.H., 1988. Characterizing Rock Joint Geometry with Joint System Models. *Rock Mechanics & Rock Engineering*, 21(1): 21-51.
- Donovan, J., Kemeny, J. and Handy, J., 2005. The Application of Three-dimensional Imaging to Rock Discontinuity Characterization. In: G. Chen, S. Huang, W. Zhou and J. Tinucci (Editors), Proceedings of the 40th U.S. Symposium on Rock Mechanics. ARMA, Anchorage, Alaska.
- Einstein, H.H., 1991. Reliability in rock engineering. In: F.G. McLean, D.A. Campbell and D.W. Harris (Editors), Proceedings of the Geotechnical Engineering Congress 1991. ASCE, Boulder, Colorado, pp. 608-633.
- Einstein, H.H., 2004. Decision Aids for Tunneling: Update. *Transportation Research Record*, 1892(2004): 199-207.
- Einstein, H.H., Lee, J.-S. and Veneziano, D., 1990. Hierarchical Fracture Trace Model, Proceedings of the 31st U.S. Symposium on Rock Mechanics. Balkema, Golden, Colorado.
- Einstein, H.H. and Lee, J.S., 1992. Topological slope stability using a stochastic fracture geometry model. In: C. Myer, Goodman, & Tsang (Editor), Proceedings of the Conference of Fractured and Jointed Rock Masses. Balkema, Rotterdam, Lake Tahoe, California, USA.
- Einstein, H.H. and Stephansson, O., 2000. Fracture Systems, Fracture Propagation and Coalescence, Proceeding of GeoEng 2000, Melbourne, Australia.
- Engelder, T. and Gross, M.R., 1993. Curving cross joints and the lithospheric stress field in eastern North America. *Geology*, 21: 817-820.
- Field, D.P., Hawley, J. and Phelps, D., 2005. The North American Tunnel Method-Lessons Learned. In: J.D. Hutton and W.D. Rogstad (Editors), Rapid Excavation and Tunneling Conference, 2005 Proceedings. SME, Seattle, WA.
- Gaich, A., Potsch, M. and Schubert, A., 2005. Improved Rock Mass Documentation in Tunnelling using JointMetriX3D, ITA-AITES 2005, Istanbul, Turkey.
- GeoWall Consortium, 2006. GeoWall.
- Gervais, F., Gentier, S. and Chiles, J.-P., 1992. Geostatistical analysis and hierarchical modelling of a fracture network in a stratified rock mass. In: C. Myer, Goodman, & Tsang (Editor), Proceedings of the Conference of Fractured and Jointed Rock Masses. Balkema, Rotterdam, Lake Tahoe, California, USA, pp. 153-159.

- Gilmour, H.M.P., Billaux, D. and Long, J.C.S., 1986. Models for calculating fluid flow in randomly generated three-dimensional networks of disk-shaped fractures: theory and design FMG3D, DISCEL and DIMES. LBL-19515, Lawrence Berkeley Laboratory, Earth Sciences Division.
- Golder and Associates, 2004. FracWorks XP Discrete Feature Simulator, User Documentation, Version 4.0, Seattle, Washington.
- Haas, C. and Einstein, H.H., 2002. Updating the Decision Aids for Tunneling. *Journal of Construction Engineering & Management-ASCE*, 128(1): 40-48.
- Hoffmann, W., Dunne, W.M. and Mauldon, M., 2004. Probabilistic-mechanistic simulation of bed-normal joints. In: J.E. Cosgrove and T. Engelder (Editors), *The Initiation, Propagation, and Arrest of Joints and Other Fractures*. Geological Society, London, Special Publications, 231, pp. 269-283.
- Hudson, J.A. and La Pointe, P.R., 1980. Printed Circuits for Studying Rock Mass Permeability (Technical Note). *International Journal of Rock Mechanics & Mining Sciences & Geomechanics Abstracts*, 17: 297-301.
- Ivanova, V., Yu, X., Veneziano, D. and Einstein, H., 1995. Development of stochastic model for fracture systems, *Proceedings of the 35th U.S. Symposium on Rock Mechanics*, Reno, Nevada, pp. 725-730.
- Kaiser, P., Henning, J., Cotesta, L. and Dasys, A., 2002. Innovation in mine planning and design utilizing Collaborative Immersive Virtual Reality (CIRV), *Proceeding of the 104th CIM Annual General Meeting*, Vancouver, BC, Canada.
- Kaplan, E.L. and Meier, P., 1958. Nonparametric Estimation from Incomplete Observations. *American Statistical Association Journal*, June 1958: 457-481.
- Kelso, J.T., Satterfield, S.G., Arsenault, L.E., Ketchan, P.M. and Kriz, R.D., 2003. DIVERSE: A Framework for Building Extensible and Reconfigurable Device-Independent Virtual Environments and Distributed Asynchronous Simulations. *Presence*, 12: 19-36.
- Kolymbas, D., 2005. *Tunnelling and Tunnel Mechanics: A Rational Approach to Tunnelling*. Springer, Berlin.
- Kovari, K. and Amstad, C., 1993. Decision Making in Tunneling Based on Field Measurements. In: J.A. Hudson, E.T. Brown, C. Fairhurst and E. Hoek (Editors), *Comprehensive Rock Engineering: Principles, Practice, and Projects, Volume 4, Excavation, Support, and Monitoring*. Pergamon Press, New York, pp. 571-606.
- Kulatilake, P.H.S.W., Um, J.-G., Wang, M., Escandon, R.F. and Narvaiz, J., 2003. Stochastic fracture geometry modeling in 3-D including validations for a part of Arrowhead East Tunnel, California, USA. *Engineering Geology*, 70(1-2): 131-155.
- La Pointe, P.R., 1993. Pattern Analysis and Simulation of Joints for Rock Engineering. In: J.A. Hudson, E.T. Brown, C. Fairhurst and E. Hoek (Editors), *Comprehensive Rock Engineering: Principles, Practice, and Projects, Volume 3, Rock Testing and Site Characterization*. Pergamon Press, New York, pp. 215-239.

- La Pointe, P.R. and Hudson, J.A., 1985. Characterization and Interpretation of Rock Mass Joint Patterns. Special paper 199, The Geological Society of America, Boulder, Colorado.
- La Pointe, P.R., Wallmann, P.C. and Dershowitz, W.S., 1993. Stochastic Estimation of Fracture Size Through Simulated Sampling. *International Journal of Rock Mechanics & Mining Sciences & Geomechanics Abstracts*, 30(7): 1611-1617.
- Lisle, R.J. and Leyshon, P.R., 2004. *Stereographic Projection Techniques for Geologists and Civil Engineers*. Cambridge University Press, New York.
- Long, J.C.S., 1993. Construction of Equivalent Discontinuum Models for Fracture Hydrology. In: J.A. Hudson, E.T. Brown, C. Fairhurst and E. Hoek (Editors), *Comprehensive Rock Engineering: Principles, Practice, and Projects, Volume 3, Rock Testing and Site Characterization*. Pergamon Press, New York, pp. 241-295.
- Long, J.C.S., Karasaki, K., Davey, A., Peterson, J., Landsfeld, M., Kemeny, J. and Martel, S., 1991. Inverse approach to the construction of fracture hydrology models conditioned by geophysical data. An example from the validation exercises at the stripa mine. *International Journal of Rock Mechanics & Mining Sciences & Geomechanics Abstracts*, 28(2-3): 121-142.
- Mauldon, M., Dunne, W.M. and Rohrbaugh Jr., M.B., 2001. Circular scanlines and circular windows: new tools for characterizing the geometry of fracture traces. *Journal of Structural Geology*, 23: 247-258.
- Meyer, T. and Einstein, H.H., 2002. Geologic stochastic modeling and connectivity assessment of fracture systems in the Boston area. *Rock Mechanics & Rock Engineering*, 35(1): 23-24.
- Muller-Salzburg, L. and Fecker, E., 1978. Grundgedanken und Grundsätze der "Neuen Oesterreichischen Tunnelbauweise". Principles of new Austrian tunnel constructions. In: O. Natau, E. Fecker and G. Reik (Editors), *Grundlagen und Anwendung der Felsmechanik; Felsmechanik Kolloquium*, Karlsruhe, Federal Republic of Germany, Feb. 23-24, 1978. *Trans Tech Publ., Clausthal, Federal Republic of Germany (DEU)*, pp. 247-262.
- Newman, T.G., Allen, R.G. and Mortimore, R.N., 2003. Geological Modelling, the observational method and management of ground hazards: Ramsgate Harbour Approach Road Tunnel. *Quarterly Journal of Engineering Geology and Hydrogeology*, 36: 35-50.
- Opriessnig, G. and Beer, G., 2001. Application of virtual reality in rock mechanics. In: P. Sarkka and P. Eloranta (Editors), *Proceedings of the ISRM Regional Symposium EUROCK 2001*. Balkema, Espoo, Finland, pp. 535-540.
- Ouenes, A., 2000. Practical application of fuzzy logic and neural networks to fractured reservoir characterization. *Computers & Geosciences*, 26: 953-962.
- Pascal, C., Angelier, J., Cacas, M.C. and Hancock, P.L., 1997. Distribution of joints: probabilistic modelling and case study near Cardiff (Wales, U.K.). *Journal of Structural Geology*, 19(10): 1273-1284.

- Peck, R.B., 1969. Advantages and Limitations of the Observational Method in Applied Soil Mechanics. *Geotechnique*, 19(2): 171-187.
- Pollard, D.D. and Segall, P., 1987. Theoretical Displacements and Stresses Near Fractures in Rock: with Applications to Faults, Joints, Veins, Dikes, and Solution Surfaces. In: B.K. Atkinson (Editor), *Fracture Mechanics of Rock*. Academic Press, New York, pp. 277-349.
- Powderham, A., 1994. An Overview of the Observational Method: Development in Cut and Cover and Bored Tunnelling Projects. *Geotechnique*, 44(4): 619-636.
- Powderham, A., 2002. The Observational Method - Learning from Projects. *Proceedings of the Institution of Civil Engineers, Geotechnical engineering* 155(1): 59-69.
- Priest, S.D. and Samaniego, A., 1983. A model for the analysis of discontinuity characteristics in two dimensions, *Proceedings of the 5th International Congress on Rock Mechanics*. Balkema, Melbourne, Australia, pp. F199-F207.
- Rasband, W.S., 2007. ImageJ, U.S. National Institutes of Health, Bethesda, Maryland, USA, <http://rsb.info.nih.gov/ij/>, 1997-2007.
- Ray, A., Decker, J.B., Vardakos, S., Antony, A., Murphy, M.M., Bowman, D.A., Mauldon, M., Gutierrez, M., Dove, J.E. and Westman, E., 2006. Visualizing fractures during tunneling with Virtual Environments. In: D.P. Yale, S.C. Holtz, C. Breeds and U. Ozbay (Editors), *Golden Rocks 2006*, Golden Colorado, pp. Accepted.
- Renshaw, C.E. and Pollard, D.D., 1992. Numerical generation of physically based fracture networks. In: C. Myer, Goodman, & Tsang (Editor), *Proceedings of the Conference of Fractured and Jointed Rock Masses*. Balkema, Rotterdam, Lake Tahoe, California, USA.
- Schultz, A.P., Stanley, C.B., Gathright, I., T.M., Rader, E.K., Bartholomew, M.J., Lewis, S.E. and Evans, N.H., 1986. Geological Map of Giles County, Virginia. Publication 69. 1: 50,000-scale colored geologic map., Commonwealth of Virginia Department of Mines, Minerals and Energy-Division of Mineral Resources.
- Snow, D.T., 1969. Anisotropic Permeability of Fractured Media. *Water Resources Research*, 5(6): 1273-1289.
- Terzaghi, K., 1961. Past and Future of Applied Soil Mechanics. *Journal of the Boston Society of Civil Engineers*, 68: 110-139.
- Terzaghi, R.D., 1965. Sources of errors in joint surveys. *Geotechnique*, 15(3): 287-304.

This page intentionally left blank.

5 Conclusions and Recommendations

Each of Chapters 2, 3 and 4 have separate Conclusion sections. However, the major conclusions from the dissertation, along with recommendations, are discussed in this chapter.

Chapter 2

Fracture parameters such as trace density and mean trace length are subject to sampling bias and censoring when measured on surfaces such as tunnel walls. For this reason, practitioners must make use of estimation techniques for characterizing rock masses.

The derived stereological estimators for trace density and mean trace length have been shown, based on Monte Carlo simulations, to be useful tools for obtaining such estimates. It was found that in general both the stereological estimators and the previously published endpoint estimators performed better when intensity was high, trace length was short, and variance was low. The stereological mean trace length estimator was more accurate than the endpoint mean trace length estimator when trace lengths were relatively short (Table 2.5). The endpoint density and mean trace length estimators were more accurate than the stereological density and mean trace length estimators when the mean trace lengths were longer (Tables 2.4 & 2.5). The endpoint density estimator was also slightly more accurate when the intensity was lower than the stereological density estimator (Table 2.4). The stereological and endpoint estimators, therefore, have been shown to complement each other. The utilization of the stereological estimators was demonstrated with field data. The results of the field analysis compared well with estimates from the endpoint estimators using the same field data (Table 2.1).

To determine estimates for trace density and mean trace length, it is recommended that the stereological estimators be utilized along with the endpoint estimators so that engineers and geologists will have more information for making sound engineering decisions. The two estimators can give engineers and geologists greater confidence in estimating trace density and mean trace length, especially when the two estimators give

similar results. If the two estimators do not give similar results, then it should be determined which estimator is likely to be the most accurate based on the mean trace length in relation to the sampling window. A general guideline for circular sampling windows is that the stereological estimators are usually more accurate when the ratio of the mean trace length to the sampling window radius is less than one, and the endpoint estimators are usually more accurate when the ratio is greater than one. In some cases, it may be useful to average the two estimators. It was shown in Chapter 3, where both the stereological and endpoint estimators were used to obtain mean trace length, that averaging the two estimators typically gave better results when performing a *DEfrac* analysis (Tables 3.4, 3.6, & 3.8). The stereological estimators should always be considered as estimates and used in conjunction with good engineering and geological judgment.

Chapter 3

The sizes and shapes of fractures, and their distributions, are very difficult to ascertain directly in an opaque rock mass. The available data, in particular fracture traces on rock surfaces, are typically censored, subject to sampling bias, and of a lower dimension than the fractures themselves. Methods must be utilized, therefore, to reduce bias in the available data and then to use the data to infer fracture size and shape. The problem of inferring fracture size and shape from trace data is an inverse problem, with no unique solution. The solution procedure is, therefore, a process of optimization – finding the fracture characteristics that produce a “best fit” for the observed data. The Differential Evolution algorithm, a Genetic Algorithm variation, has been used effectively for optimization in many different fields. Differential Evolution is utilized in this dissertation to produce a “best fit” fracture based on trace data and is referred to as the *DEfrac* method.

The Kaplan-Meier method applied to censored traces (*K-M-trace*) is very effective in eliminating bias, due to censoring, to produce empirical CDF's (Figure 3.8). If the sampling window is large, in relation to the trace lengths, a full empirical CDF may be obtained. If the sampling window is small, in relation to the trace lengths, only a portion of the empirical CDF will be obtained. It should be noted when using the *K-M-trace*

procedure that it deals only with the bias of censored traces. The *K-M-trace* procedure can be used to determine empirical CDF's for many different applications and analyses of trace data. In applying empirical CDF's, computed using the *K-M-trace* procedure, to the *DEfrac* method, an initial straight-line portion of the CDF should be approximated. When using field data, it is recommended that a range of initial slopes be determined from the empirical CDF to be used in the *DEfrac* analysis.

The *DEfrac* method is an effective optimization procedure, utilizing Differential Evolution, that uses trace data from two or more non-parallel planes to infer the size and shape of rectangular fractures (Figures 3.12, 3.13, 3.14, & 3.15). It works well for fracture populations that follow the basic assumptions used to derive the method. It loses some accuracy, but still works fairly well, when the assumption of constant orientation is violated. The examples given in Chapter 3 indicated that a mutation scaling factor F of 0.5, a crossover rate CR of 1, and 60 to 100 generations were efficient input parameters for the Differential Evolution algorithm. The method can be easily applied using the Excel Spreadsheet *DEfrac*. The *DEfrac* method appeared to give reasonable results for a field example. When using the *DEfrac* method in the field, however, the limitations of the simplifying assumptions should be noted and taken into account. In any case, the result from a *DEfrac* analysis is strictly an estimate and should be used along with geological experience and engineering judgment. It should also be noted that the over all method is only as accurate as the estimated trace data on each plane. The *DEfrac* method can be applied to two non-parallel planes; however, it is recommended that if possible data on at least three non-parallel planes should be used. The *DEfrac* method is suited for many applications of tunneling where non-parallel planes are exposed, e.g. room and pillar mining.

Chapter 4

It is vital that methods and tools, developed for characterizing and simulating rock mass conditions for tunneling, can be applied in the field. Part of this dissertation research was to implement methods and tools that had been developed, by this research or previous research, to gather and analyze data during tunneling and then to build, update, and verify fracture models based on that data. A field study was conducted

within an unlined tunnel in Giles County, Virginia to implement and test these methods and tools.

The field study illustrated the application of state of the art imaging equipment for gathering data during tunneling. Data gathering with the imaging equipment was quick and facilitated remote sampling. The use of digital photography requires artificial light beyond the flash of the camera itself. If no artificial light can be used or if the artificial light is inadequate for digital photography, LiDAR can obtain 3d imaging data without the aide of artificial light. Digital photography was typically faster than LiDAR imaging; however, personnel were not required within the tunnel during the duration of a scan.

The 3d visualization of imaging data allowed for accurate remote sampling. In the case of remote orientation measurements, the 3d visualizations allowed for fracture planes to be confidently identified for measurement. For trace maps, the 3d visualization helped distinguish between actual traces and other features (e.g. water marks, excavation marks, vegetation, etc.) that may appear as traces on a 2d image. It is recommended that 3d visualization be a part of any remote sampling exercise to improve accuracy. Also the engineers and geologists who are performing the remote sampling should be familiar with the sight.

Obtaining, analyzing, and implementing rock mass data into support and excavation design during tunneling requires careful planning. Important considerations include: equipment to be used, training of personnel, safety considerations, logistics of communication, timing of data acquisition in conjunction with excavation, what data are desired, detailed procedures for obtaining data, design of a relational database for storage and easy access of data, analysis procedures to be used, and procedures for updating support design and excavation design.

The use of forward modeling was shown to be an effective way to update and verify fracture models as new data is obtained (Figure 4.21). It is suggested that fracture models should be updated using statistical methods as well as verified visually. Visual checks include the concepts of consistency, plausibility, and completeness. Consistency incorporates verifying the model with previous geological observations in the tunnel and surrounding area. It should be noted that structural, lithologic, or other types of major discontinuities render previous geological observations not applicable in some cases.

Consistency also encompasses the verification of the model with other measurements such as geophysical measurements ahead of the excavation. Plausibility refers to geological compatibility with geologic setting, processes and geomorphology.

Completeness incorporates the inclusion/omission of major features that might need to be inserted deterministically and the appropriate resolution or level of detail for analysis.

The principles of forward modeling can also be applied to updating and verifying rock mass parameters and indices such as those incorporated into the RMR or Q-system.

This page intentionally left blank.

6 Recommended Further Research

- Further testing of the stereological estimators should be performed to define confidence intervals. Additionally further research is needed on inferring 3d rock fracture parameters (including shape, size, spatial distribution, intensity, etc) from fracture trace data.
- The *DEfrac* method needs to be extended to account for any fracture size distribution and to other assumed fracture shapes such as elliptical and circular, and to incorporate other parameters and geologic data. Examples of other data that could be brought to bear on inference of fracture size and shape include fracture trace density and intensity, aperture, lithology, elastic properties of the rock, knowledge of boundary conditions and stress state at the time fractures formed, termination relationships, conductance of fluids, and so forth.
- The *K-M-trace* method developed should be furthered studied. Monte Carlo simulations should be conducted to test method and to better demonstrate its use and application.
- The methods applied in the field study in Chapter 4 need to be applied and implemented more often in the industry. There is no better test than real world applications. Such methods include the use of databases, imaging, 3d visualization, remote sampling, and forward modeling. The use of these tools and methods would not only increase the safety, cost efficiency, and quality of tunneling, but it would facilitate new insights on how to use these tools and technologies for the increased benefit of the tunneling industry. The author has learned through direct communications with tunneling engineers and contractors that the industry has interest in implementing and advancing such techniques.
- Development of rapid field measurement techniques using modern equipment such as LiDAR and photogrammetry to obtain key fracture parameters such as orientation, trace length, trace abundance, aperture, etc.

This page intentionally left blank.

Jeremy Bruyn Decker

EDUCATION

Ph.D., Civil Engineering, Virginia Polytechnic Institute and State University, May 2007
M.S., Civil Engineering, Brigham Young University, 2001
B.S., Civil Engineering, Brigham Young University, 2000

RESEARCH AND WORK EXPERIENCE

Research

Graduate Research Assistant, 1/04-present, Virginia Tech Civil Engineering Department

Part of collaborative research team for a NSF funded project, AMADEUS (Adaptive Mapping, Analysis, and Design of Underground Space).
Perform research in Fracture mapping, statistical analysis of fractures, and visualization of fracture models in Virtual Environments.
Perform field investigations (fracture mapping) to test and validate methods developed in research.

Research Assistant, 1/00-5/01, BYU Civil Engineering Department

AutoCAD drawings for liquefaction research.
ArcView used to create settlement drawings for liquefaction research.
Thesis--Study on the Corrosion of Piles on the Old I-15 Corridor, Salt Lake City, Utah.

Teaching

Course Instructor, 8/05-12/05, Virginia Tech Civil Engineering Department

Instructor for senior/graduate level Engineering Geology course.
Taught under the supervision of a faculty mentor.

Graduate Teaching Assistant, 5/04-7/04, Virginia Tech Civil Engineering Department

Teaching assistant for a short course on Rock Mechanics taught for Corps of Engineers geologists at Virginia Tech.
Graded homework and tests.
Worked directly with participants to help them understand concepts and complete assignments
Helped coordinate with lecturers and organized course material (helped make course CD).
Lectured and authored some course material

Tutor, 6/98-12/99, BYU Civil Engineering Department

Helped students in the tutorial lab with Dynamics class.

Graded tests for Statics, Materials, and Dynamics classes.
Helped students in the tutorial lab with Mechanics of Materials class.

Teacher/Instructor, 01/97-06/98, The Church of Jesus Christ of Latter-day Saints
Teacher at the missionary training center in Provo, Utah.
Taught newly called missionaries communication and teaching skills, scripture study skills, and scriptural knowledge.
Supervised missionaries in call center (received inbound and outbound calls concerning media offerings).
Helped missionaries adjust mentally and spiritually to missionary life.

Work

Staff Engineer, 6/01-7/03, Speedie and Associates, Phoenix, Arizona
Planned, proposed, and conducted field geotechnical investigations using hollow stem augers with standard penetration testing, coring equipment, Becker drill rigs, and seismic testing.
Drafted and reviewed geotechnical reports for commercial and residential building projects, transportation projects, and utilities.
Designed shallow and deep foundations for bearing capacity and settlement.
Designed and gave recommendations for geotechnical hazards such as expansive and collapsible soils.
Recommended slope requirements for excavations.
Designed and recommended road section thicknesses.
Inspected installation of drilled shaft foundations.
Worked part-time with the Geotechnical Group of the Arizona Department of Transportation—contracted through Speedie and Associates for 1 year (4/02-4/03).
Helped coordinate geotechnical investigations for Transportation projects using ADOT resources and outside consultants.
Drafted geotechnical reports for transportation projects.
Reviewed geotechnical reports written by consultants.
Took part in design of road cuts, embankments, subgrade, and foundations for transportation projects and facilities.

Civil Engineering Intern, 5/99-9/99, Utah Department of Transportation
Inspected, evaluated, designed, and implemented erosion control in Provo Canyon.
Managed the installation of a revegetation area protection fence.
Helped survey and was a field inspector for the beginning of an excavation for a wetland.

PUBLICATIONS

Decker, J.B., Rollins, K.M., Ellsworth, J.C., Corrosion Rate Evaluation for Piles Based on Long-Term Field Performance, (submitted to Journal of Geotechnical and Geoenvironmental Engineering, September 2006).

- Ray, A.A., Decker, J.B., Vardakos, S., Murphy, M., Bowman, D., Gutierrez, M., Mauldon, M., Dove, J. and Westman, E., 2006. A Virtual Environment for Visualizing Fractures During Tunneling. In: D.P. Yale, S.C. Holtz, C. Breeds and U. Ozbay (Editors), Proceedings of the 41st U.S. Symposium on Rock Mechanics, Golden, Colorado, June 17-21, 2006, Paper No. 1104.
- Decker, J.B. and Mauldon, M., 2006. Determining Size and Shape of Fractures from Trace Data using a Differential Evolution Algorithm. In: D.P. Yale, S.C. Holtz, C. Breeds and U. Ozbay (Editors), Proceedings of the 41st U.S. Symposium on Rock Mechanics, Golden, Colorado, June 17-21, 2006, Paper No. 969.
- Decker, J.B., Antony, A., Ray, A., Vardakos, S., Murphy, M.M., Mauldon, M., Dove, J.E., Gutierrez, M., Bowman, D. and Westman, E., 2006. An Integrated Relational Database for Tracking Rock Mass Data during Tunneling. Proceedings of the ITA-AITES 2006 World Tunnel Congress and 32nd ITA General Assembly, Seoul, Korea, April 22-27, Paper No. 312—*also in* Tunnelling and Underground Space Technology (abstract only), 21, pp 429.
- Decker, J.B., Mauldon, M. and Wang, X., 2006. Real-time Determination of Fracture Size and Shape using Trace Data on Walls. Proceedings of the ITA-AITES 2006 World Tunnel Congress and 32nd ITA General Assembly, Seoul, Korea, April 22-27, Paper No. 313—*also in* Tunnelling and Underground Space Technology (abstract only), 21, pp 233.
- Decker, J.B. and Rollins, K.M., 2002. Corrosion Rate Evaluation and Prediction for Piles: Salt Lake, Utah Case Histories. Proceedings of the Transportation Research Board 81st Annual Meeting, Washington D.C., January 13-17, 2002, Paper No. 4072.
- Decker, J.B., 2000. Corrosion Rate Evaluation and Prediction for Piles: Salt Lake, Utah Case Histories. Thesis, MS, Civil and Environmental Engineering, Brigham Young University, Provo, Utah.

AWARDS / AFFILIATION

Full tuition University academic scholarship from BYU
Honor's list in the College of Mathematical and Physical Sciences - BYU
Dean's list five semesters in the College of Engineering - BYU
Received an academic scholarship from ADSC for graduate school - BYU
Via Fellowship at Virginia Polytechnical Institute and State University
Student member of ASCE and ARMA